Development of a novel alignment sensing and control technique for the output mode cleaner at GEO 600

Von der Fakultät für Mathematik und Physik
der Gottfried Wilhelm Leibniz Universität
Hannover
zur Erlangung des Grades

Doktor der Naturwissenschaften
Dr. rer. nat

genehmigte Dissertation
von

MSc.-Phys. Aparna Bisht

2020

Referent:	Apl. Prof. Dr. Benno Willke (Leibniz Universität Hannover)
Korreferent:	Prof. Dr. Hartmut Grote (Cardiff University)
Korreferent:	Prof. Dr. Kenneth A. Strain (University of Glasgow)
Tag der Promotion:	18.09.2020

Abstract

We are in the era of multi-messenger astronomy, with gravitational wave detectors playing a pivotal role. All current long-baseline detectors are advanced versions of the basic Michelson interferometer. One of them is GEO 600, located in Hannover, Germany, where this thesis is based.

Once a detector is commissioned, it has to be maintained at a favourable operating state. This is mostly done with automatic control loops. Two of the most important kinds of control are length control and angular control. This thesis is about the development of a high bandwidth autoalignment control scheme for the detector's output beam to the output mode cleaner located just before the main photodiode. The scheme is called modulated differential wavefront sensing (MDWS) and is based on the well-known differential wavefront sensing alignment technique into the regime of beams with strong higher order mode content. The MDWS control surpasses the pendulum resonances without additional auxiliary modulations. Due to these advantages, it is foreseen that it can replace the current autoalignment scheme called the beacon dither scheme that has a low bandwidth of less than 20 mHz.

In chapter 2, the implementation of the MDWS scheme for a stable-low-bandwidth state is shown where a bandwidth of up to 2 Hz could be achieved. This is already 100 times more than the beacon scheme's bandwidth. During the course of this work, challenges were encountered that prevented the full time implementation in a high-bandwidth state. To better understand the observed behaviour, the system was modelled in Simulink (described in chapter 3) along with a combination of modelling tools like Mathematica and Finesse and a noise budget was made with the help of the SimulinkNb tool. To make the model realistic, measurements were performed that gave a deeper understanding of several subsystems and these results have been used as model input. The knowledge gained about the system through the modelling work will form the basis of further development of the MDWS scheme and eventually in its full-time implementation.

keywords: gravitational wave, differential wavefront sensing, autoalignment, higher order modes

Contents

List of Figures

List of Tables

Glossary

AA	automatic alignment.
AC	alternating current.
ADC	analog to digital converter.
AEI	Albert Einstein Institute.
au	arbitrary units.
BDO	beam directing optic.
BS	beam splitter.
CDS	LIGO control and data system.
CMB	cosmic microwave background.
DAC	digital to analog converter.
dB	decibel, relative unit of measurement.
DC	direct current and also 0 Hz frequency.
EOM	electro-optic modulator.
EP	error point/error signal.
ESD	electro-static drive.
FP	feedback point/feedback signal.

GW	gravitational wave.
HOM	higher order mode.
IFO	interferometer.
IR	infrared.
LED	light emitting diode.
LO	local oscillator.
LSC	LIGO Scientific Collaboration.
MCE	close east mirror.
MCN	close north mirror.
MFE	far east mirror.
MFN	far north mirror.
MPR	power recycling mirror.
MSR	signal recycling mirror.
OLTF	open loop transfer function.
PBS	polarising beam splitter.
Pol	polarisation.
PZT	piezoelectric transducer.
SNR	signal to noise ratio.
TEM	transverse electric mode.

TF	transfer function.
TIA	transimpedance amplifier.
UGF	unity gain frequency.

CHAPTER 1

Introduction

The discovery of Gravitational Waves (GWs), momentarily, laid to rest the human curiosity of ever being able to measure them precisely. Albert Einstein, who formulated the General Theory of Relativity, predicted their existence in 1916 but he was almost certain that they cannot be measured. Indeed, it took about a century for an experimental effort to overcome the challenges and make the first-ever direct detection ever of GWs (the event named as GW150914) on 15th September, 2015, almost simultaneously, by the LIGO (Laser Interferometer Gravitational-Wave Observatory) sites in the United States [1]. The origin of the waves was the collision between two black holes (35.4 $M_\odot$, 29.8 $M_\odot$), that happened approximately about 1.4 billion light years ago, making it the first direct observation of such a merger. The detected signal lasted for only about 0.2 seconds but was substantial for the analysis that followed. The Nobel Prize 2017 in Physics was awarded to pioneers - Rainer Weiss, Kip S. Thorne and Barry Barish for building LIGO and for the detection of GWs.

Our knowledge of what exists in the cosmos came mainly through electromagnetic (EM) observations till GWs added the audible frequency range (between 10 Hz to upto 3 kHz) to the possible range of frequencies that we can probe. For this reason, the GW observatories are often referred to as the *ears* to the universe. It was on August 17, 2017 that a GW event named GW170817 [2] was detected by a network of the Advanced LIGO [3] and the Advanced Virgo detector [4] (known as the second generation or Advanced detectors). This event was independently detected as a gamma-ray burst by the Fermi-GBM detector [5]. Due to the well constrained sky localization of the three-detector network, an extensive search was done in the electromagnetic spectrum by several detectors for weeks. The concluding hypothesis was that the event was caused by the merger of two neu-

tron stars in the NGC 4993 galaxy (at a distance of about 40 Mpc) which was followed by a gamma ray burst and a kilonova event [6]. This multi-messenger observation of GW170817 suggest that BNSs are a, if not the most likely, source of heavy elements such as gold and platinum found in the universe.

Till date, three observation runs of different time durations have been done by the GW detector network and multiple confirmed GW events have been reported. Around the time of writing this thesis, an unforeseen GW event named GW190814 was announced [7]. The binary in the merger consists of a black hole that is nine times heavier than its counterpart where the lighter companion could be the lightest black hole or the heaviest neutron star ever observed in a compact binary system. The ambiguity about its nature will push the understanding of the models of the formation of compact-objects. With such breakthrough discoveries, the field of GW astronomy only gets more exciting with time.

1.1 Sources of gravitational waves

Masses of astronomical sizes can distort the rigid fabric of spacetime. The idea of spacetime (three-dimensional Euclidean space and a the fourth dimension of time) entangled together to form the *spacetime fabric*, was first introduced by Hermann Minkowski in 1908 [9]. Einstein further extended this theory to conclude that gravity is a manifestation of the presence of mass due to which straight-line motion of objects around that mass gets curved instead. This effect is caused by any mass, whether big or small. Another important hypothesis made by Einstein was that if masses accelerate then they will distort the spacetime fabric momentarily like a passing wave, these are gravitational waves.

The known sources of GWs can be classified into four broad categories - Continuous Gravitational Waves, Compact Binary Inspiral Gravitational Waves, Stochastic Gravitational Waves, and Burst Gravitational Waves. A detailed description of GW sources can be found in [11]. The most common ones as shown in fig. 1.1 are compact binary systems such as :

- Binary Neutron Star (BNS)
- Binary Black Hole (BBH)

- Neutron Star - Black Hole Binary (NSBH)

So far most of the astronomy has been based on observations made using EM radiation such as radio waves, X-rays, visible light, etc. The advantage with GW radiation is that the universe is nearly transparent to them such that they are neither reflected or absorbed by matter as much as EM radiation. This presents to us a unique possibility of observing the universe with a tool that did not exist till now. Also, if stochastic GWs carry the signature of the Big Bang and can be detected by GW detectors, then that will be most distant event that humans have ever observed. Thus, the potential of GW astronomy is enormous.

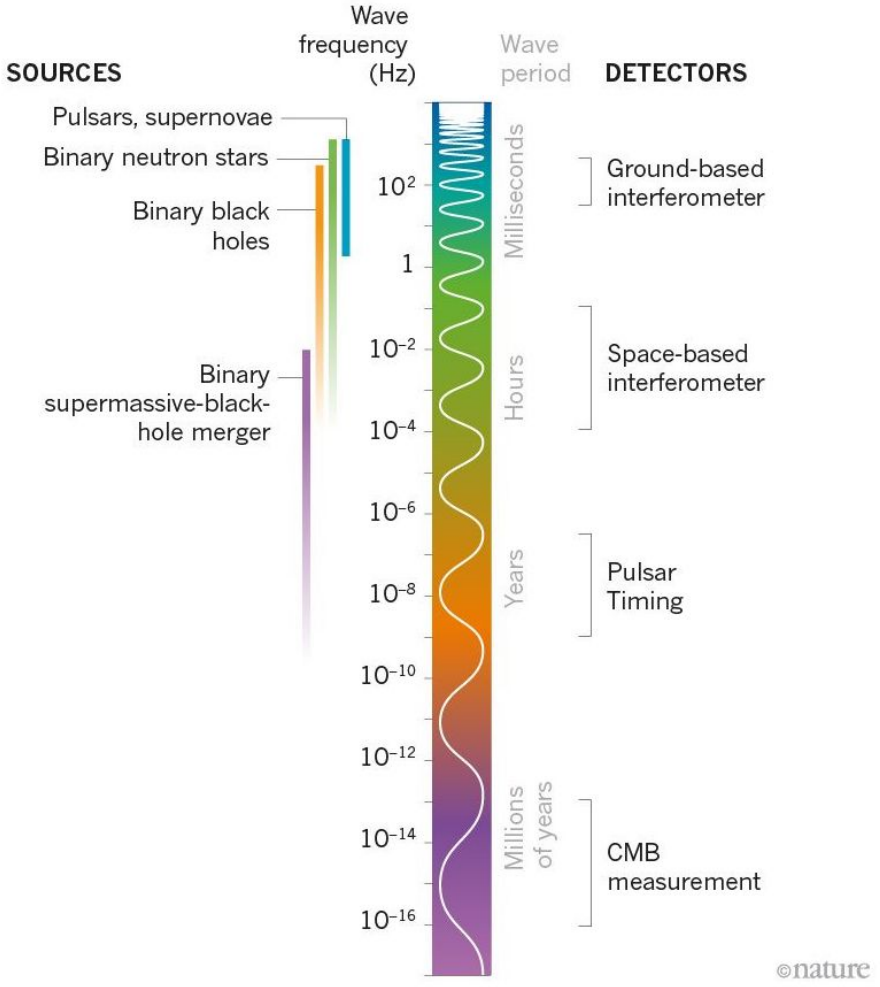

Figure 1.1: The different sources and detectors of GW radiation [8].

1.2 Using a Michelson interferometer for detection of gravitational waves

Building a detector for GWs was pioneered by Joseph Weber in 1960s at the University of Maryland. The detector, called the Weber bar, was an Aluminium cylinder (about 1.52 m long, 0.6 m diameter) decoupled by external vibrations, which was supposed to be excited at its resonance frequency by a passing GW. Although no detection was made with high confidence, this technique was pursued by similar detectors like MiniGrail, EXPLORER, NAUTILUS,etc. An overview of these detectors can be found in [13].

In 1962, it was proposed by Michael Gertsenshtein and Vladislav Pustovoit in Moscow, Russia that laser interferometry could be used. In 1967, Rainer Weiss at Caltech demonstrated the operation of a Michelson Interferometer (MI IFO) and also precisely studied the fundamental noise sources that would affect the detector sensitivity [26]. This was followed by the building of a prototype detector by Rainer Weiss at MIT, USA, Hans Billing's group in Garching, Germany and by Ronald Drever and Jim Hough in Glasgow, Scotland. Also, a theoretical group was set up by Kip Thorne in 1968 at Caltech, USA. Hence, a MI IFO came to be the instrument of choice by GW researchers.[1]

1.3 Effect of gravitational waves

The effect of a passing GW is that it causes spacetime to *stretch* in one-half cycle of the wave and *squeeze* it in the other half-cycle. For a MI IFO having an arms-length L, this would appear as if one arm length has been reduced to L_1 and the other has increased by a small amount to L_2 as shown in fig. 1.2. The relative length change, δl equals $L_1 - L_2$.
The amplitude of a GW, h_{GW}, can then be related to δl by the following formula:

$$h_{GW} = \frac{\delta l}{L} \tag{1.1}$$

where $\frac{\delta l}{L}$ is the detector *strain*.

[1] The MI IFO was initially used by A. Michelson and E. Morley for their well known *aether* experiment [12] in 1887.

A GW may have two polarisation states: Plus (+) and Cross (x). The small length change between the two arms causes the laser beam in each arm to travel unequal distance causing a phase difference that can be detected by a photodetector at the output port of the IFO. This is the basic principle of GW detection [11]. The challenge arises in keeping the IFO as *quiet* as possible such that the phase difference does not appear from a fluctuation in a noise source that can affect the arm length.

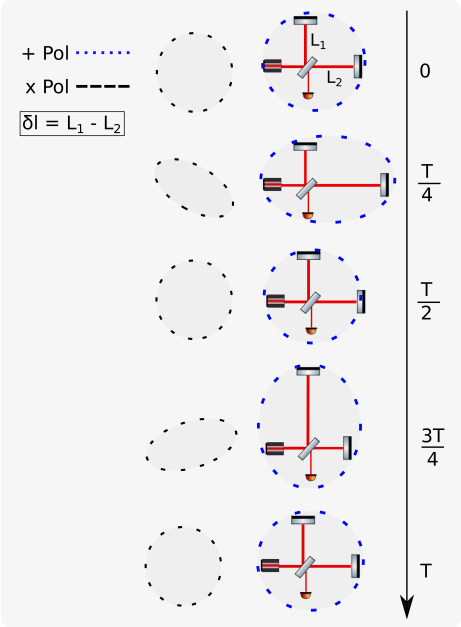

Figure 1.2: The effect of a passing GW wave on the *free test masses* of the MI IFO where the travel direction of the wave is into the plane of the paper.

1.4 Current and future GW observatories

At the moment, there is a network of five long-baseline GW detectors referred to as the Advanced detectors or the 2G detectors. The more detectors there are, the better an event's source can be located or localized [11]. The operational large scale GW detectors are - LIGO Hanford, USA (4 km), LIGO Livingston, USA (4 km) , Virgo, Italy (3 km), KAGRA, Japan (3 km) [14] and GEO 600, Germany (600 m) [15]. A third LIGO facility is planned in India and is being constructed [16]. All of these are based on the MI IFO design with the addition of advanced technologies. The 2G

ground-based detectors have so far taken part in three coincident searches for GWs where at least two detectors were taking data simultaneously. The last run termed as O3 between Virgo, GEO 600 and both LIGO detectors concluded in March 2020 [17]. In April 2020, there was another short run (called O3GK) between GEO 600 and the newly operating KAGRA detector, mainly for getting KAGRA data into the network.

Efforts are being made towards the development of the third generation of GW detectors as well. The list of future 3G detectors includes the Einstein Telescope (ET), the Cosmic Explorer (CE) and the LIGO Voyager [18], [19], [20], [21], [22], [23]. Each of these facilities will be based on Michelson interferometry but while the ET and CE will be built as completely new observatories, the Voyager will be built in the existing LIGO facility. These 3G detectors will make use of new and/or improved technologies that is expected to be at least ten times better than the 2G detectors from approximately 10 Hz to about 10 kHz, and more than 10000 times better at lower frequencies (below 10 Hz).

Another significant addition to the search for GW waves at frequencies between 0.1 mHz and 1 Hz will be made by LISA (Laser Interferometer Space Antenna), [24]. LISA is a space-based observatory and will consist of three freely floating spacecraft million miles apart from each other.

1.5 GEO 600

GEO 600 is a dual recycled Michelson interferometer [34], [35] which is a collaborative project of a British-German group of scientists, located near Hannover, Germany [25], [30], [31], [32]. Several advanced interferometric techniques have been pioneered by the GEO 600 group which played an important role in kick-starting GW astronomy [36]. GEO 600 is also well known for being the first-ever detector to implement long term Squeezing [38], [43], [44], [45]. The GEO 600 observational mode is referred to as *Astrowatch* and has been in this mode since 2011. A supernovae-like event would be an interesting source candidate for GEO 600 due to being more sensitive at high frequencies. A promising candidate would be Betelguese that is about 642.5 light years away in our galaxy. A typical sensitivity curve of the detector is shown in fig. 1.5.

Each arm of the detector has a length of 600 m with an additional folding as shown in fig. 1.3 that makes the effective travel length of the laser in each arm to be 1200 m. The folding design distinguishes GEO 600 from the other GWDs just like the fact that no arm cavities are used. Instead the detector makes use of the dual recycling technique that enhances the laser power as well a potential GW signal.

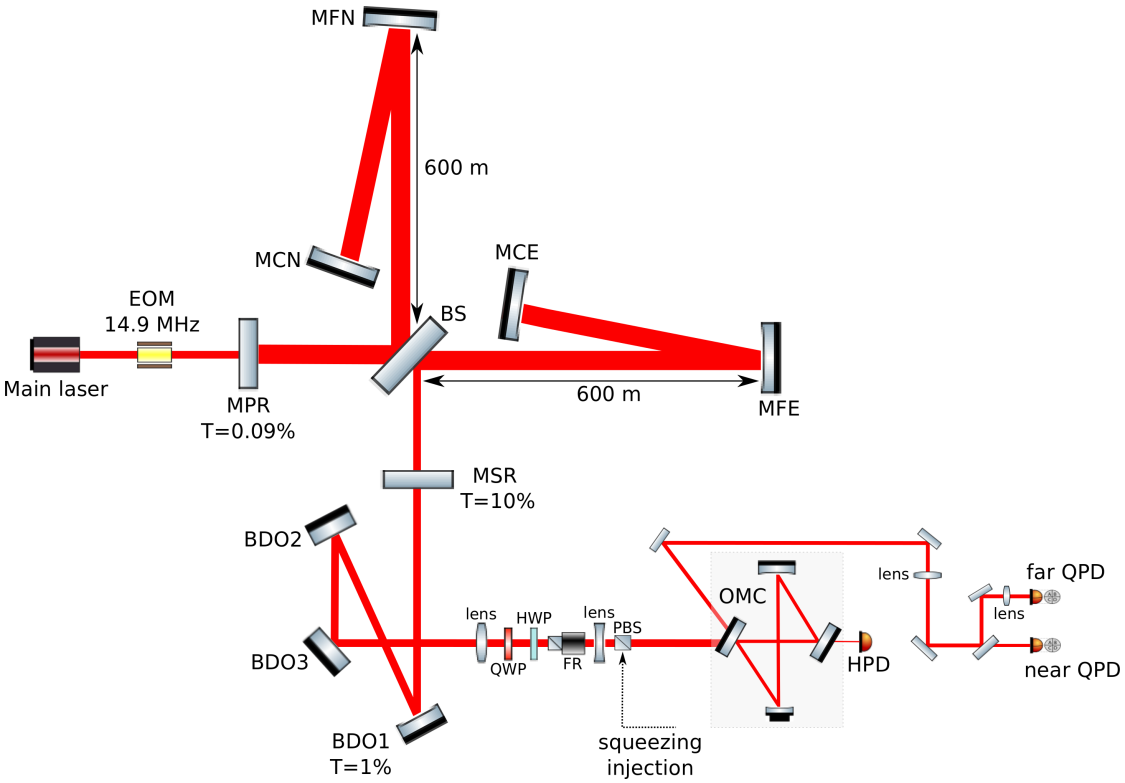

Figure 1.3: A simplified layout of GEO 600. The input optics between the laser and the EOM are not shown due to not being relevant to the topic of this thesis. The output optics consists of the three BDO mirrors, lenses for mode matching to the OMC as well as components for squeezing injection, the OMC and the HPD. The optical components in reflection of the OMC consists of the 'Near QPD' and 'Far QPD' along with related optics that are part of AA techniques for aligning the IFO output beam to the OMC.

The *Dual Recycling* technique - Power Recycling (PR) and Signal Recycling (SR) is used in the normal operation of the detector [28], [29]. For PR, a mirror is placed at the input of the IFO called the power recycling mirror

(MPR, see fig. 1.3) that forms a virtual Fabry-Perot cavity called the Power Recycling Cavity (PRC). The PRC is formed by the MPR and the Michelson interferometer and has a gain factor of about 850 for the input light. It thus resonantly enhances 3 W of the input beam to approximately 2.5 kW. A high power beam resonating in the IFO improves the sensitivity of the detector in the shot noise limited region (above 1 kHz) and thus improve the SNR of a potential GW signal. Yet the high PR gain combined with the fact that the waist of the laser beam (about 1 cm) lies very close to the beam splitter (BS) leads to strong thermal lensing of the BS. This poses various challenges as discussed in [46], [66].

Similar to the PRC, another cavity is formed by the Michelson and the signal recycling mirror (MSR, see fig. 1.3) at the detector output, called the Signal Recycling Cavity (SRC). The SRC is resonant for sidebands created on the carrier due to differential length changes such as caused by a passing GW. The SRC length can be tuned for best sensitivity at DC or detuned for peak sensitivity around a desired frequency [73].

The technique used for reading the *GW channel* is called as DC readout [67], [68]. This requires operating the MI at a slight offset from the dark fringe condition, called as the dark fringe offset (DFO) that allows a small fraction of the carrier field resonating in the IFO to leak out at the detector output port (also called darkport). The leaked out carrier serves as the local oscillator (LO) for the GW signal that appears as sidebands on the carrier. The DC readout scheme has the fundamental advantage of reduced shot noise and compatibility with squeezing, as compared to the traditional heterodyne readout schemes.

The output optics as shown in fig. 1.3 consists of the three beam directing optics (BDO) - BDO1, BDO2 and BDO3 that are used for steering the beam. The curved BDO1 mirror (RoC of 3.5 m) along with a pair of lenses form a mode matching telescope for the IFO output beam on to the filtering cavity called the output mode cleaner (OMC) [47], [48], [49].

1.5.1 The necessity of an Output Mode Cleaner (OMC)

The DFO ensures that only a small fraction of the resonating carrier (about 6 mW) leaks out of the IFO. An additional pair of sidebands at 14.9 MHz,

called as the Michelson Sidebands (MI SBs) also exits with the carrier (each having about 1 mW). These are imprinted on the carrier by an EOM that introduces phase-modulated sidebands before the carrier enters the Michelson as shown in fig. 1.3. The MI SBs are resonant in the interferometer but with a resonant factor much less than the carrier. Hence they can be used as a reference for the IFO axis and is used for locking of the Michelson arms, also called as IFO length lock.

The largest contribution to the IFO output beam is not the carrier and the MI SBs but higher order modes (HOMs) that contribute to about 36 mW of the output beam if operated at 2 kW impinging on the BS. The HOMs and the SB fields cause shot noise at the HPD and thus mask a GW signal. To prevent them from contaminating the GW signal a filtering cavity is installed. It is the output mode cleaner (OMC) that rejects the HOMs and the MI SBs by creating a resonant cavity for the carrier only.

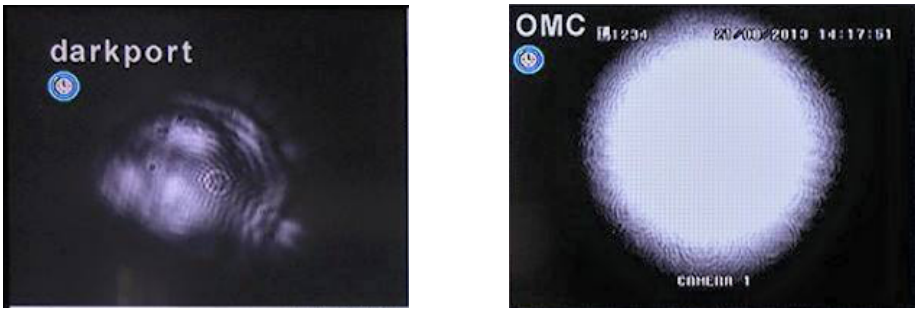

(a) Before the OMC (≈ 40 mW) (b) After the OMC (≈ 6 mW)

Figure 1.4: Fig (a) shows the beam at the darkport consisting of contaminated with HOMs and control SBs . Fig (b) shows the carrier TEM_{00} in transmission of the OMC. This clean light is incident on the HPD.

The OMC is a four mirror bow-tie cavity with a 98% transmission for the TEM_{00} mode of the carrier. It is designed to attenuate unwanted light fields by a factor of 100 or higher [49]. A PZT is attached to one of the mirrors as the actuator for its length control which is done by the dither locking technique (explained in Chapter 2). A dither modulation is applied to the length of the OMC via a PZT at 6 kHz, this frequency at the edge of the GEO detection band. The error signal is derived by demodulating the cavity transmitted signal at the dither frequency.

This thesis deals with angular sensing and control of the OMC. Since length control and angular control are independent degrees of freedom (DoF) so any of these two control can be applied first without any preference. However, due to the aforementioned HOM content at the input of the OMC, the length control is done first. Once the OMC is locked to the carrier, the eigenmode axis is well determined which can be used as a clean reference for angular control.

1.5.2 Causes of higher order modes

The HOMs arise at the IFO output port due to several reasons:

1. Asymmetry in the arms of the IFO caused due to manufacturing defects such as the difference in the radius of curvature (RoC) of the mirrors and imperfect mirror surfaces.

2. Thermal lensing in the beam splitter due to high power beams i.e. due to the aforementioned high PR factor and beam waist close to the BS. The heat absorbed by the beam splitter can cause effects such as refractive index change and cause expansion of the beam splitter material. This will lead to an optical path length difference in two high powered beams that can distort the beam splitter and cause HOMs. At the default operating laser power, the HOM content due to the BS thermal lensing is low but if high laser power is used then significant challenges arise [46],[66].

3. The third reason for HOMs is such as due to suspension resonances. The low frequency motion of the mirrors can introduce small misalignment angle between the two interfering beams at the beam splitter.

There are techniques in place and are being further investigated to reduce the HOMs at the IFO darkport. The first is the use of a ring heater behind MFE that corrects for the RoC mismatch and a pair of side heaters to correct for astigmatism also around the MFE. A combination of these reduces the total power of HOMs by about 37% [66]. Additionally, there is *mode healing* [49] due to the MSR such that it reflects the HOMs back into the IFO where they are cancelled by the HOMs being reflected by the MPR and are converted into the fundamental mode.

There is also a beam splitter thermal compensation system (TCS) which is an active area of research at GEO 600 [66]. It will be used for actively correcting the deformation of the beam splitter due to thermal lensing. This will further reduce the HOM content of the IFO beam when it is operated at higher input laser power.

1.6 Need for alignment sensing and control

A GW detector is made of up of multiple coupled cavities formed by suspended optics. Alignment of a Gaussian beam to an optical cavity is crucial to the operation of an interferometric gravitational wave detector and is needed,

i. To maximise the power build-up in the cavities: high circulating power in the IFO enhances sensitivity where shot noise dominates in the detector readout and improves the SNR of a potential GW signal.
ii. To keep the interferometer stable: the angular motion of the mirrors can modulate optical transfer functions which can cause the calibration of the detector to be less accurate. It can also drive the IFO away from the linear regime and cause instability.

To automatically align an incoming beam to a cavity requires fast control in the form of automatic alignment (AA) techniques. An ideal AA scheme suppresses the angular motion of the mirrors without adding significant noise to the GW measurement channel. Currently, the low frequency sensitivity of all terrestrial GW detectors is limited by the technical control noises [37]. As it can be seen in fig. 1.5, the alignment noise completely dominates over other noise sources for low frequencies at GEO 600. The confirmed GW detections show that the low frequencies are particularly interesting because the strongest part of inspiral is at low frequency. Also, other unforeseen sources of GW might lie in the low frequency regime. This makes the task of designing AA schemes challenging as well as rewarding.

One such technique for the alignment of the IFO output beam to the OMC forms the main content of this thesis. It is based on differential wavefront

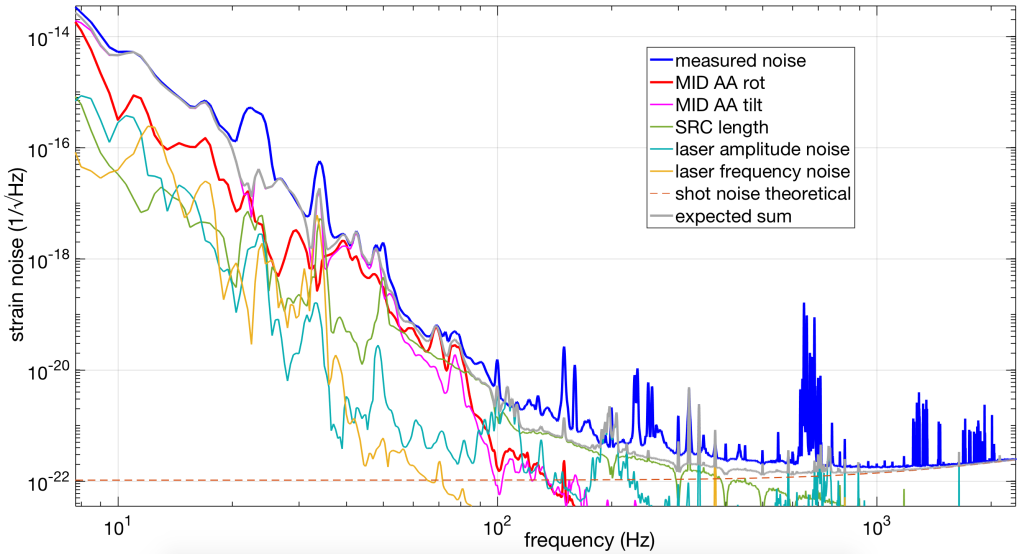

Figure 1.5: A typical GEO "noise budget" plot showing the contribution of noise sources that combine to form the limiting sensitivity (residual noise) of the detector. This is also referred to as the h curve and has a peak value of $1.7\text{x}10^{-22}$ $1/\sqrt{Hz}$ at 1 kHz. Please note that a few other noise sources have been ignored for the purpose of this plot. A detailed description in given in [33].

sensing (DWS) and is called Modulated Differential Wavefront Sensing (MDWS). The output port of the detector is dominated by HOMs and control sidebands called as "junk light". The component at carrier frequency is very small as described in section 1.5.1. MDWS with its high bandwidth is a suitable scheme for preventing the GW signal from being contaminated by these unwanted junk components. The details of the scheme and its implementation are discussed in detail in chapter 2.

1.7 About the thesis

This thesis can be divided mainly into two parts given in chapter 2 and chapter 3, respectively. Chapter 2 begins with a brief revision of the basics of alignment of Gaussian beams. It is followed by a discussion of the traditional AA scheme used for aligning the IFO beam to the OMC called the beacon dither AA technique. It is a robust technique but has certain disadvantages as will be described in the chapter. It is followed by a description of the DWS technique that is itself based on the Pound Drever Hall (PDH)

locking technique. The second half of the chapter will be a detailed discussion of the MDWS AA technique and the related subsystems such as the local control (LC), the spot centring loops etc. The experimental work related to the implementation of MDWS at GEO 600 is also described in detail in this chapter. The concluding section will deal with the challenges faced during the MDWS investigations and motivates the need for studying the noise sources affecting it. I have not included the basics of feedback control which is at the core of any AA system. For a quick and practical understanding of the subject, one can refer to [39] and [40].

Chapter 3 presents a unique approach for building the noise budget of the MDWS system using numerous modelling tools. Firstly, a control model is developed and then noise sources are injected and projected using the SimulinkNb tool. Most of the injected noise sources have been measured on-site or in the lab environment. The measurement results are also presented in the chapter. Finally, the contribution of the noise sources to the MDWS error signals that the model produces have been presented and studied in the last section. The inclusion of measured noise sources makes the study realistic but further measurements are necessary to validate the results of the model.

A brief summary of the entire work will be given in chapter 4 where the outlook is also discussed. The appendices section contains measurements and scripts that were used during the course of this thesis. The work related to the thesis was carried out at the GEO 600 detector facility.

CHAPTER 2

Alignment sensing and control techniques for the OMC at GEO 600

The task of aligning a laser beam to an optical cavity requires two kinds of sensing and control - longitudinal alignment and angular alignment. Simply speaking, longitudinal control means to keep the length of the cavity locked, usually, to the TEM_{00} mode of a laser beam. Angular alignment means to sense and control the angle as well as the position of the optical axis of an incoming beam w.r.t the cavity's eigenmode axis. Thus, the DoF space for longitudinal control is 1-dimensional and for alignment control it is 4-dimensional. In the rest of the discussion, unless otherwise stated, the cavity is assumed to be locked. Therefore, alignment would refer only to angular alignment.

The need of an OMC as well as an AA system for aligning the IFO's output to the OMC has been emphasised in chapter 1. In 2011, the OMC AA system was changed to the beacon dither alignment after having investigated a few schemes with simple dithering of the output optics (BDO mirrors) earlier. The addition of a beacon signal along with the existing dither lines ensured that pure TEM_{00} component of the IFO beam is maximized in the transmission of the OMC vs simple dithering in which the scheme may find an alignment where HOMs can get partially transmitted. Also, the HOMs in the IFO output beam cause coupling of beam jitter to the detector strain channel [36]. Due to this, the dither frequencies were chosen to be quite low as well as have low SNR [49]. This caused the bandwidth of the beacon dither technique to be limited to about 20 mHz which is not sufficient to compensate for alignment fluctuations of the Michelson

suspension resonances. Although, it is enough for keeping the IFO output beam aligned to the OMC to follow slow alignment drifts such as daily temperature changes. In addition, the dithers themselves cause jittering of the beam that affects the application of squeezing as described in section 2.3.1.

To get an improvement on the shortcomings of the beacon dither technique and with an aim of replacing it permanently, the Modulated Differential Wavefront Sensing (MDWS) scheme is being developed at GEO 600. The immediate benefit of MDWS includes getting rid of the dithering process and a higher control bandwidth. The preliminary testing as well as proof of principle demonstration has been done as described in section 2.4. Moreover, a noise budget model has been developed and is a handy tool for studying the system better as described in chapter 3. In this chapter, both the AA techniques are described with a focus on the MDWS scheme.

2.1 Angular alignment of optical resonators

To keep an incoming beam coincident to a cavity at all times needs sensing and control. This has to be done for four DoFs - lateral displacement and the angle between the optical axes for the horizontal and vertical plane. A misalignment between the input beam axis and the cavity axis can be described as a combination of these two cases. Additionally, waist size and waist position mismatch can occur which usually do not require fast active control and are not dealt with in this thesis. However, for completeness they are shown in fig. 2.1 where the possible misalignments are shown which are similar for the x and y plane.

2.2 Gaussian beams

The best description of a monochromatic laser beam is given by the Gaussian function [41], [42]. The equations of misalignment can be developed following the familiar nomenclature for the Hermite-Gaussian (HG) modes. The mth-order of a Gaussian beam propagating in the positive z direction is given by

$$E_m(x,z) = E_m H_m \frac{\omega_0}{\omega(z)} \frac{\sqrt{2}x}{\omega(z)} \; e^{-\frac{x^2}{\omega^2(z)}} \; e^{-j\frac{kx^2}{2R(z)}} \; e^{-j[kz-(1+m)\tan^{-1}(\frac{z}{z_R})]}. \quad (2.1)$$

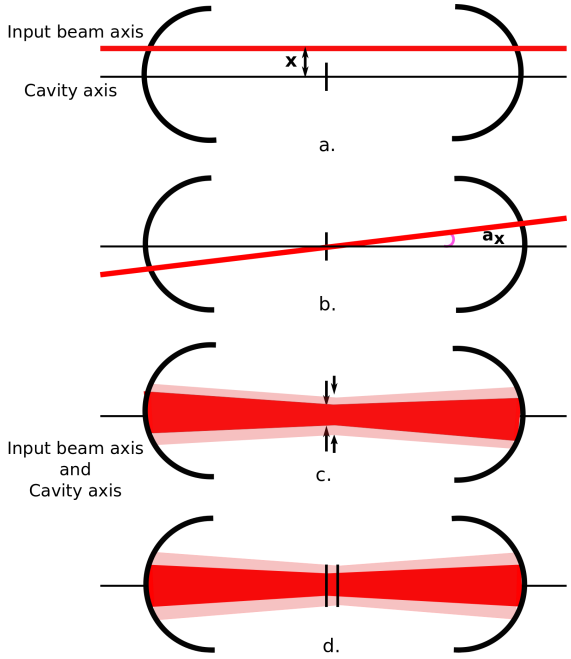

Figure 2.1: Misalignment of Gaussian beams. a). Lateral displacement b). Mismatch in incoming angle c). Mismatch of the waist size d). Mismatch of the waist position.

where, m is an arbitrary integer denoting the spatial mode number and H_m is the Hermite polynomial. A similar expression can be derived for the spatial distribution of the Gaussian field in the y-direction, giving H_n, where n is the mode number.

$\omega_0 = \sqrt{\frac{\lambda_0 z_R}{\pi}}$
where, ω_0 is the beam waist or the minimum spot size
λ is the wavelength of the Gaussian beam

$\omega(z) = \omega_0 \sqrt{1 + (\frac{z}{z_R})^2}$, is the beam spot size

when $z = z_R$, $\omega(z) = \sqrt{2}\omega_0$, z_R is the Rayleigh length

$R(z) = z[1 + (\frac{z}{z_R})^2]$, is the radius of curvature of the wavefront

$\phi(z) = \tan^{-1}(\frac{z}{z_R})$, is a phase shift that a Gaussian beam accumulates due to having non-planar wavefronts. This is called as Gouy phase shift.

The Gouy phase is an important property associated with Gaussian beams and determines the eigenmodes of a resonator as

$$\nu_{q,nm} = \frac{c}{2L}[q + (n + m + 1)\frac{\phi(z)}{2\pi}] \tag{2.2}$$

where, q∈ N
n,m are longitudinal and transverse mode numbers, respectively.

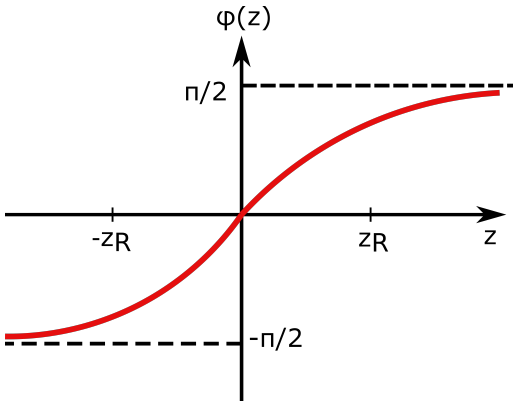

Figure 2.2: A Gaussian beam undergoes a π phase shift when passing through a waist as shown.

The HOMs arise due to the presence of Hermite polynomials, H_{mn}, as in eq. 2.1. Again for simplicity considering only the x direction, the polynomial of order m is given by:

$$H_m(u) = (-1)^m e^{u^2} \frac{d^m e^{-u^2}}{du^m} \tag{2.3}$$

It is instructive to consider a few of the lower order ones:
$H_0(u) = 1$
$H_1(u) = 2u$
$H_2(u) = 2(2u^2 - 1)$

Substituting these in the Gaussian beam equation we get the electric field distribution associated with the first three modes as described in eq. 2.3 to 2.5 and also shown in fig. 2.3.

$$E_0 = A_1\, exp(\frac{-x^2}{\omega_0^2}) \tag{2.4}$$

$$E_1 = A_2\, \frac{x}{\omega_0} exp(\frac{-x^2}{\omega_0^2}) \tag{2.5}$$

$$E_2 = A_3\, (\frac{4x^2}{\omega_0^2} - 1)\, exp(\frac{-x^2}{\omega_0^2}) \tag{2.6}$$

where A1, A2, A3 are amplitude constants.

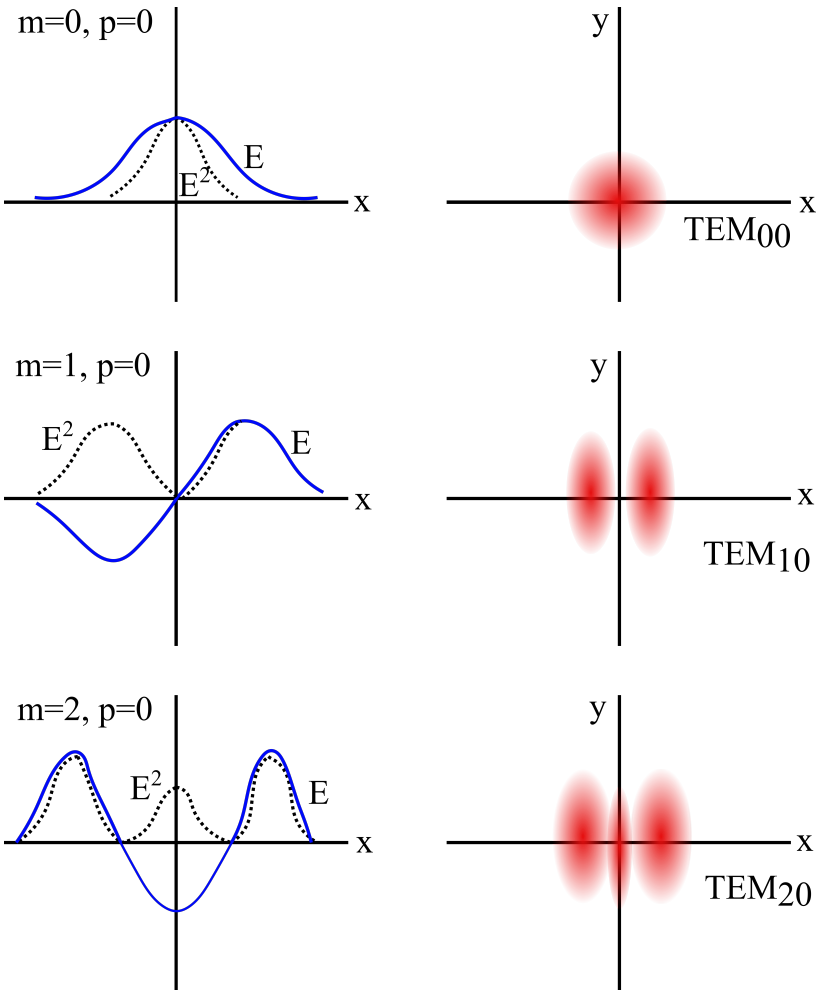

Figure 2.3: The field E, intensity E^2 and the transverse profile of various modes. The number of times that the amplitude of the field goes to zero, other than at ∞ is the mode number m. The same is true for the y direction also. The spot size $\omega(z)$ is the same for all modes plotted above but the radial extent becomes larger for higher order Gaussian beams.

2.2.1 Modal picture in the presence of misalignment

2.2.2 Beams with an angle

If a TEM_{00} beam is at an angle α w.r.t a fixed reference (such as the axis of a cavity) then it can be denoted as:
$E_{angle} = A_t\ exp(\frac{-x^2}{\omega_0^2})\ exp(jk\alpha x)$
for small values of α, $exp(jk\alpha x) = 1 + jk\alpha x - k^2x^2\alpha^2$....

$$E_{angle} \approx E_0 + jk\alpha\omega_0 E_1 \tag{2.7}$$

So the beam having an angle α can now be expressed as a sum of a fundamental and a first higher order mode beam that is 90° out of phase with the fundamental.

2.2.3 Laterally displaced beams

If a beam is displaced w.r.t a TEM_{00} beam in the positive x direction by a small amount β, it can be denoted as:
$E_{displaced} = A_d\ exp(\frac{-(x-\beta)^2}{w_0^2})$
Again for small values of β, this expression can be expanded to give,
$E_{displaced} = A\ [1 - \frac{x^2}{w_0^2} + \frac{x}{w_0}(\frac{2\beta}{w_0})(1 - \frac{x^2}{w_0^2})]$, where A is a constant

$$E_{displaced} \approx E_0 + \frac{2}{\beta w_0 E_1} \tag{2.8}$$

Thus, a laterally displaced beam introduces a first order term in phase with the fundamental.

2.3 Alignment control for the OMC

The OMC as described in section 1.2.1 is a necessary filter at the output of the IFO to prevent higher-order modes and other unwanted light fields from reaching the detection photodiode. Its location can be seen from fig 1.3. Misalignment of the input beam to the OMC causes intensity variations at the HPD. These will be mistaken as intensity variations of the DFO and lead to undesired MID actuation. Therefore, automatic alignment is needed to keep the IFO beam and the OMC eigenmode axis

aligned at all times. In this section, two AA schemes for the OMC are described - the traditionally used beacon dither technique and the new MDWS scheme.

2.3.1 The Beacon Dither alignment technique

The existing method for OMC AA is the beacon dither technique based on dithering the quantity of interest which in our case is the alignment degrees of the beam incident on the OMC [70], [71]. Let the intensity (I) at the HPD be described as a function of input beam angle (θ) as I (θ). A modulation is injected into θ as follows:
$\theta = \theta_0 + msin(\omega t)$
where m«1 is the modulation index and ω is a defined dither frequency. Then the resulting intensity fluctuation will look like:

$$I_\theta = I(\theta_0 + m\ sin(\omega t)) \approx I(\theta_0) + \frac{\partial I}{\partial \theta}(\theta_0)\ m\ sin(\omega t) + ... \tag{2.9}$$

The amplitude of ω is proportional to the partial derivative term and can be extracted by demodulation. Since the cavity transfer function is symmetric around optimal alignment, the derivative will disappear, indicating the desired alignment for that degree. If this is done for all four degrees of alignment then four feedback loops can be employed to keep the incoming beam aligned to the cavity at all times. This is the principle of dither locking.

The beacon dither technique (shown in fig. 2.4) aims to maximize the transmission of the GW mode by an extension of the simple dithering technique called the optimal beacon dither as described in [78]. At GEO 600, it is implemented as follows:

i. A beacon signal is imprinted on the IFO output beam by differentially actuating on the MI end test masses - MCN and MCE, via the electrostatic drive (ESD) actuators at a frequency of 3.17 kHz (f_b). Since the differential arm length change is the effect that a GW would cause, the beacon marks the alignment of the same optical mode that a GW signal would be in.

ii. The alignment dithers are applied at their respective (f_d) frequencies to the steering mirrors, in our case two of the three Beam Directing Optics (BDO), BDO1 and BDO3, as given in table 2.1. These dithers mark the

four degrees of alignment of the mirrors. In this thesis, the rotation of the mirror about the horizontal axis is called tilt and about the vertical axis is called rot. The LIGO nomenclature is pitch and yaw, respectively. The error signals are obtained by demodulating the transmitted field through the OMC at f_b+f_d and filtered and fed back to the BDOs.

The beacon dither scheme is robust against small alignment drifts and is sufficient for the daily operation of the detector but has certain limitations. First, the control bandwidth achieved is less than 20 mHz [49]. Since there is a substantial amount of beam motion caused by the residual misalignment of the MI suspension resonances around 1 Hz, the beacon dither scheme is unable to suppress it.

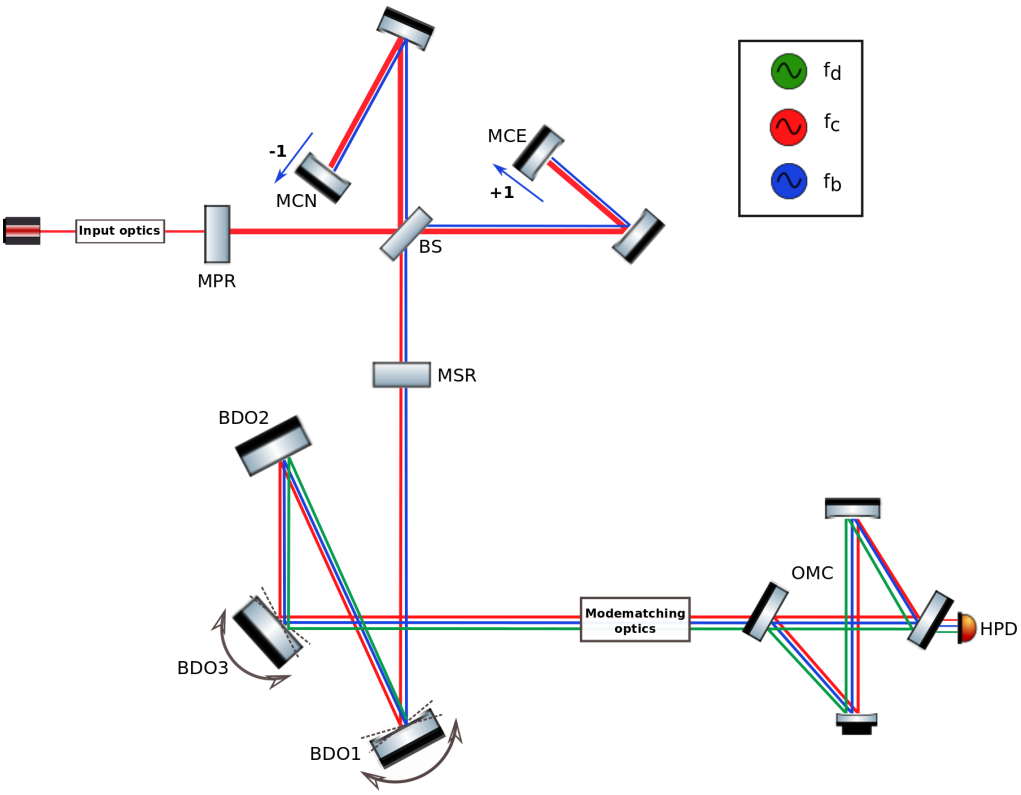

Figure 2.4: Simplified GEO 600 schematic to show the beacon dither control scheme and the respective optical components.

Second, the process of dithering introduces additional motion of the OMC input beam such that the amplitude of the dithers dominates the RMS alignment fluctuations of the beam. This causes optical loss for squeezing

	Rot (Hz)	Tilt (Hz)
BDO1	17	11
BDO3	3.5	14

Table 2.1: Alignment dithers for the BDO mirrors

injection as can be seen from fig. 2.5.

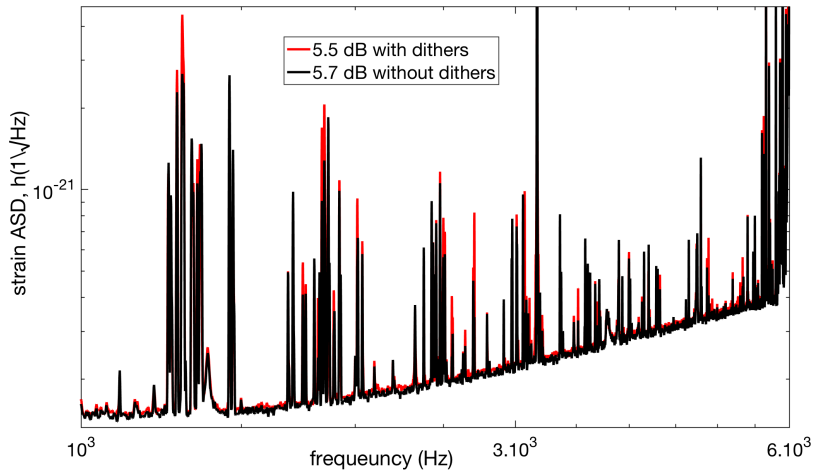

Figure 2.5: The effect on h due to the BDO dithers. The dithers introduce 0.2 dB loss in squeezing at the 5.5 dB level and contribute 1 % loss in the total optical loss budget of squeezing at GEO 600.

To get around the shortcomings of the beacon dither technique the new MDWS scheme was proposed and tested as given in [36]. This scheme eliminates the BDO dithers and also has higher control bandwidth that can reduce beam jitter coupling to the GW readout [33] as described in the next section.

2.3.2 Differential Wavefront Sensing

At the heart of DWS is the Pound-Drever-Hall (PDH) locking technique ([53], [54]) used for stabilizing the frequency of a laser beam by locking it to a reference as provided by a stable cavity or vice versa. The equations for DWS are an extension of this scheme and hence a short review on PDH is given first.

The PDH technique makes use of modulation sidebands on to a carrier

field that is used for locking a cavity to a stable frequency reference or vice versa. It just depends on where the actuation is done. For our case, we actuate on the OMC cavity length to follow the IFO beam.

Let the light field incident on the cavity, E_{inc}, be modulated in phase to introduce modulation sidebands,

$$E_{inc} = E_0 e^{j(\omega t + m \sin \omega_1 t)} \tag{2.10}$$

$$E_{inc} \approx E_0 e^{j\omega t}[1 + jm sin w_1 t] \tag{2.11}$$

where m(t) is a small modulation index and ω_1 is the frequency of modulation.

This creates two additional components in the light field at ω_1 and -ω_1,

$$E_{inc} \approx E_0 e^{j\omega t}[1 + \frac{m}{2} e^{j\omega_1 t} - \frac{m}{2} e^{-j\omega_1 t}]. \tag{2.12}$$

The sidebands are chosen to be outside the bandwidth of the cavity so they are promptly reflected and not affected by the drift in cavity length. They serve as a constant phase reference for the carrier to beat against.

The total reflected field has the form:

$$E_{refl} = e^{j\omega t}[E_0^r + \frac{m}{2} E_+^r e^{j\omega_1 t} + \frac{m}{2} E_-^r e^{-j\omega_1 t}]. \tag{2.13}$$

where E^r is the reflected field at the respective frequencies.
A photo detector in reflection detects the total power, P_r:

$$P_r = E_{refl}.E_{refl}^* \tag{2.14}$$

$$P_r = [|E_0^r|^2 + |E_+^r|^2 + |E_-^r|^2] + [(E_0^{r*} E_+^r + E_0^r E_-^{r*}) e^{j\omega_1 t} + constants] + [E_+^r E_-^{r*} e^{2i\omega_1 t} + constants] \tag{2.15}$$

The signal of interest is the second term of eq. 2.15. It is the beat between the carrier and the sidebands and can be extracted by demodulating the photocurrent proportional to P_r at ω_1 to obtain the in-phase and quadrature components as $\mathrm{Re}[(E_0^* E_0 + E_0 E_-^*)]$ and $\mathrm{Im}[(E_0^* E_0 + E_0 E_-^*)]$, respectively. If the phase of the carrier field drifts due to a change in the cavity length it acquires an additional phase shift. The beat signal between the phase shifted carrier and sideband frequency is the PDH signal as shown

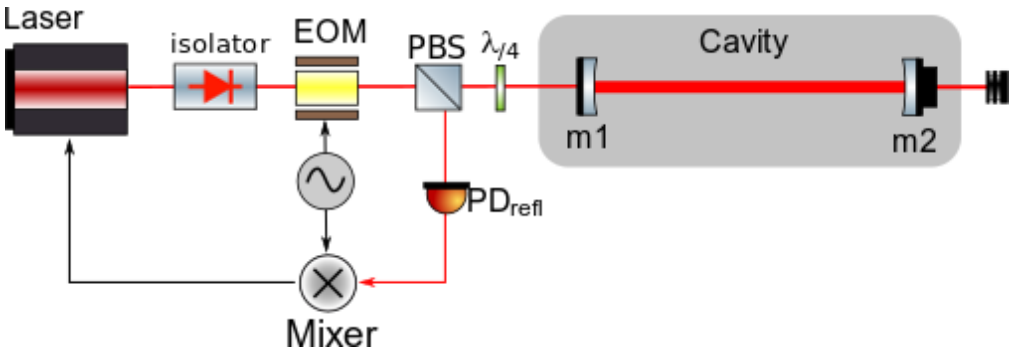

(a) PDH setup for a Fabry Perot cavity. The modulation sidebands are applied via the EOM. The length of the cavity is changed by moving mirror m2 with an actuator.

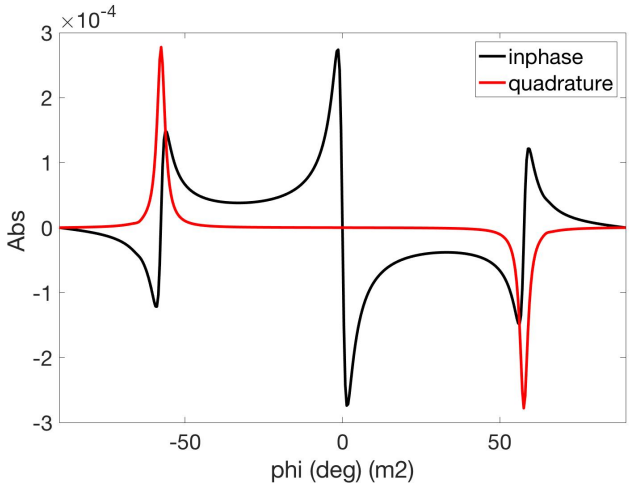

(b) The PDH readout signal. There are three points where the signal crosses zero. The (0,0) corresponds to the carrier being resonant while the symmetric zero points on either side denote the position of the sidebands being resonant. A feedback loop can then keep the cavity locked to a resonating carrier field or the laser cavity can be actuated to follow the cavity length as shown here.

Figure 2.6: The PDH technique

in fig. 2.6b. This signal being antisymmetric around the resonance of the carrier can be used by a feedback loop to keep the cavity locked.

After the longitudinal degree of a cavity has been locked using the PDH technique (or any other), the relative misalignment between the axis of the incoming beam and the cavity eigenmode axis can also be sensed by the same technique of using phase modulated sidebands also called as heterodyne sensing. For optical cavities in an IFO, the sensing of misalignment is done using a split quadrant photodetector (QPD) as shown in fig. 2.7. In the presence of a misalignment (overlap of TEM_{00} and TEM_{01} mode) a spatial gradient will develop across the interference pattern. If this is incident on a QPD then by taking the difference of photocurrents from the four quadrants the position of the combined beam can be obtained for the horizontal and vertical plane. The misalignment between the two axes can be obtained by demodulating the photocurrents at the modulation frequency. For detecting the four DoFs of misalignment two QPDs have to be placed at a Gouy phase difference of $\frac{\pi}{2}$. This concept was first proposed in [50] and first shown experimentally in [51], [52] and later in [55] as well.

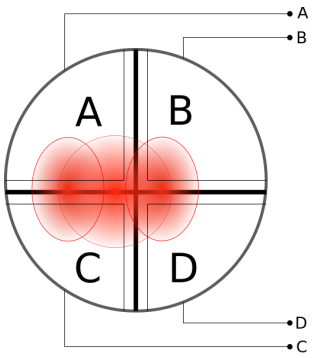

Figure 2.7: A quadrant photodetector with a TEM_{00} and a TEM_{10} beam. The difference of currents on its quadrants is calculated as: $I_x = \frac{I_A+I_C-I_B-I_D}{I_A+I_C+I_B+I_D}$ and $I_y = \frac{I_A+I_B-I_C-I_D}{I_A+I_C+I_B+I_D}$ where the subscript x and y denote the horizontal and vertical plane respectively.

To make the equations generic to longitudinal and angular misalignment, the notations of [51] is being used. The modulated and matched field can be described as

$$E_1 = A_1 U_0 e^{j(\omega t + m(t) + \Phi)}, where \tag{2.16}$$

m(t) is the phase modulation and Φ is a constant phase difference between the fundamental modes of E_1 and a mismatched field, E_2, described as

$$E_2 = A_2 U_0 e^{j\omega t} + A_2 U_1 e^{j(\omega t + \phi(z) + \alpha_n)}, where \tag{2.17}$$

$\phi(z)$ is the Gouy phase shift associated with the first order mode of a Gaussian beam and α_n is the phase shift due to the misalignment. For beam tilt, $\alpha_0 = \frac{\pi}{2}$ and for beam translation, $\alpha_1 = 0$.
Also, U_0, U_1, U_2 are the first three higher order modes of a Gaussian beam.

The total light field incident on a photo detector is given by $E_t = E_1 + E_2$ and the signal is given by

$$E_T = E_t E_t^*. \tag{2.18}$$

The resulting field has terms due to the superposition of the fundamental modes of the two fields, which are proportional to $A_1 A_2 U_0^2 cos(m + \Phi)$. Taking the integral and demodulating at m gives the PDH error signal. However, the terms interesting for angular mismatches are the coefficients of $E_0 E_1$ and when the modulation m is small,

$$E_T \approx U_0 U_1 [m \sin(\phi - \alpha_n)]. \tag{2.19}$$

This approximation is valid only when $\Phi = 0$, i.e., when the length of the cavity is held constant and the second order modes, arising due to mismatches in the waist size and the position of the two interfering beams, have also been corrected. Using a quadrant photodiode, the difference in intensity of its two halves along the x-axis can be expressed as

$$I_x = \int_0^\infty E_T dx - \int_{-\infty}^0 E_T dx. \tag{2.20}$$

$$I_x \approx m \sin\phi \cos\alpha_n - m \cos\phi \sin\alpha_n. \tag{2.21}$$

A QPD placed at the beam waist (z=0) will reduce eq.2.21 to,

$$I_x \approx -m \sin\alpha_n. \tag{2.22}$$

and I_x will be maximized for $\alpha_0 = \frac{\pi}{2}$. In other words, the QPD signal will be maximally sensitive to a misalignment in tilt. In the same way,

a QPD placed in the far field ($z \approx \infty$) will be maximally sensitive to a misalignment in translation (α_1 = 0) where eq.2.21 will have the form,

$$I_x \approx m \cos \alpha_n. \tag{2.23}$$

Hence two QPDs placed at z = 0 *(near sensor)* and z $\approx \infty$ *(far sensor)* can give the four misalignments. For the rest of the thesis the following nomenclatures is used :
The horizontal alignment signal from the near QPD is called *near X* and the vertical alignment signal from the near QPD is called *near Y*. Similarly, the horizontal alignment signal from the far QPD is called *far X* and the vertical alignment signal from the far QPD is called *far Y*.

2.4 Modulated Differential Wavefront Sensing

The equations developed for DWS can be extended now to explain the Modulated DWS (MDWS) scheme. As explained in section 1.2.2, the light fields at the GEO 600 output port consists mostly of HOMs, control sidebands and only a small component at the carrier frequency. This means that the leakage field from the OMC is also contaminated and a small misalignment of the carrier w.r.t. to modulated sidebands, that serve as a reference for alignment, cannot be sensed accurately by a DWS setup. Therefore, an additional modulation frequency is used that marks the mode of the OMC eigenmode. The sensing procedure remains the same.

i. The first is a phase modulation at 14.9 MHz, referred to as the MI SBs (f_{MI}), which is done to the MI input beam (see Figure 2.8). The MI SBs are resonant in the MI along with the carrier, but with a smaller power enhancement factor. Hence, they are predominantly in the TEM_{00} mode and serve as a good approximation of the fundamental GW carrying mode [36]. Also, they are promptly reflected by the OMC and can be found in the OMC reflected field.

ii. The second modulation at 6 kHz (f_{OMC}) is done via the PZT attached to one of the mirrors of the OMC. This frequency f_{OMC}, modulating the carrier inside the OMC, appears as phase modulation sidebands leaking out through the reflection port of the OMC, thus marking its eigenmode. There is also a component due to the prompt reflection of the carrier at the

OMC reflected port, but this does not contain information about the cavity mode. It should be mentioned here that f_{OMC} is an already existing modulation used for the longitudinal control of the OMC by the dither locking technique. Therefore, no additional auxiliary modulation is required for MDWS.

In this case, the error signals can still be obtained using the difference of the modulated currents from the quadrant photodiode but now the signal will be present at the beat frequency of $f_{MI} - f_{OMC}$. Eq.2.21 gets modified as

$$I_x \approx (m_1 - m_2)\sin\phi\, cos\, \alpha_n - (m_1 - m_2)\cos\phi\, \sin\alpha_n \tag{2.24}$$

where $m_1 = f_{MI}$ and $m_2 = f_{OMC}$. The signal of interest is obtained by a two-step demodulation. The first demodulation at f_{MI} is done in the analog domain, giving the DWS signal. This signal is acquired by the digital system [79] and then demodulated at f_{OMC}, giving the MDWS error signal.
The MDWS error signal, in essence, gives the relative misalignment between the MI SBs at f_{MI} (RF) that represents the GW mode and the OMC length dither at f_{dither} (audio) that represents the OMC eigenmode [33].

A crucial component of all the AA schemes at GEO 600 is centring the beam spot on all wavefront sensors or QPDs (also shown in fig. 2.8. At the IFO output port, a scheme based on detecting the power at twice the frequency of MI SBs called the 2f sensing is used as described in the following section. Also in [51], the authors have pointed at the necessity of having the spot of the interfering beams centred on the quadrant photodiodes. Failing which, a considerable amount of signal is lost.

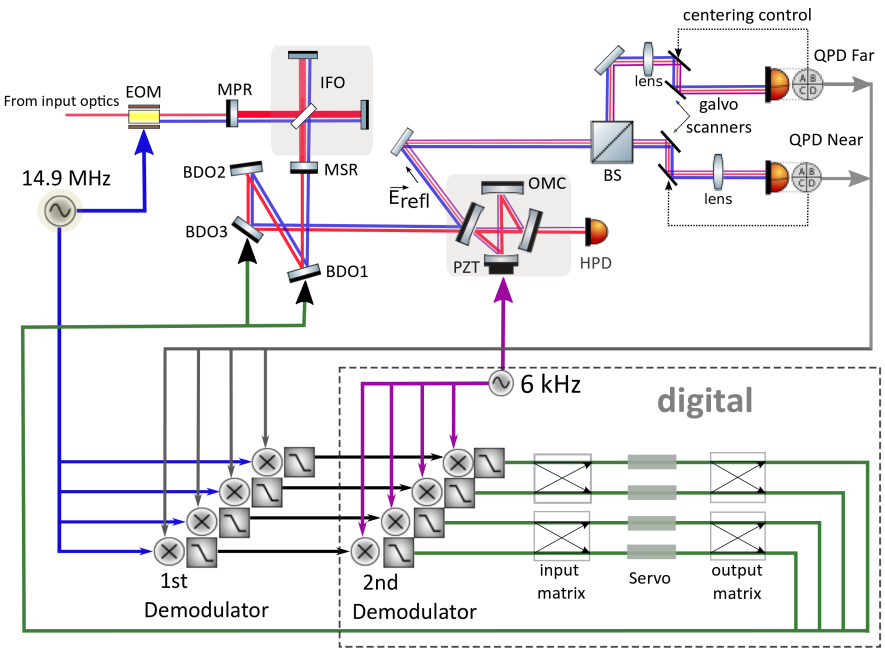

Figure 2.8: The MDWS control schematic. The green signal line shows the MI SBs, f_{MI} being imprinted onto the carrier through the EOM. The yellow line shows the OMC dither, f_{dither} applied via the PZT attached to one of the mirrors of the OMC. The centring control shows the near and far detection paths and the related optical components. Furthermore, the two demodulation steps and the generation of the MDWS error signal is shown. The feedback loops get closed through the actuation path to BDO1 and BDO3.

2.4.1 The 2f beam centring technique

To be able to get reliable MDWS alignment signals the spot of the interfering light fields has to be kept centered on the QPDs based on the 2f sensing technique. The usual method for spot centring is based on ensuring that the DC power is symmetrically distributed on the sensors. In the case of interfering light fields at the detector output, this method does not work because the carrier is dominated with HOMs thus making the DC signal unreliable. Instead, the distribution of the MI sidebands are used at twice the frequency, $2f_{MI}$, giving the light field intensity on the four quadrants at $2f_{MI}$ [44],[73]. Fig. 2.9 shows the generation of the spot centring error signal from the f_{MI} sidebands at the reflected port of the OMC.

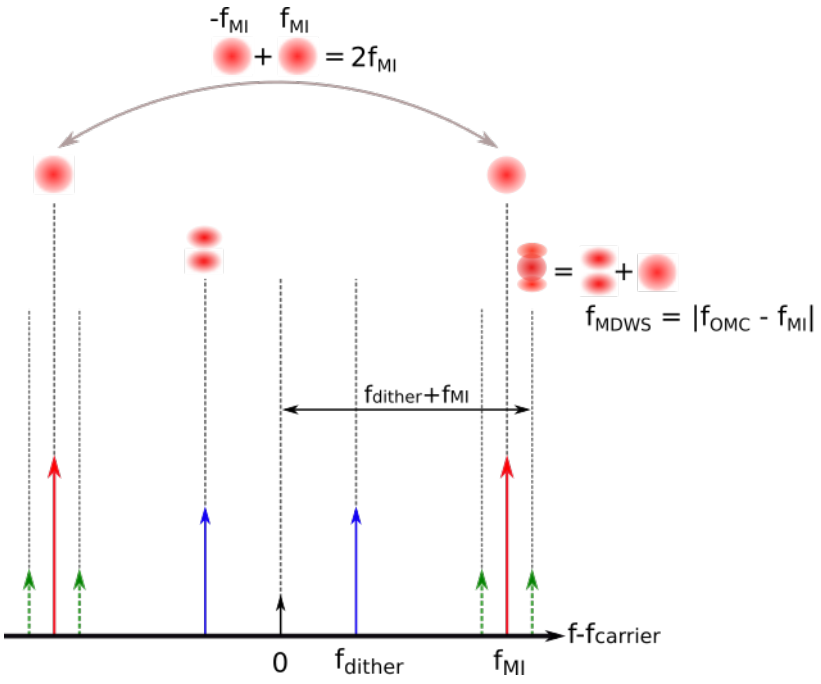

Figure 2.9: A not to scale representation of the electric field distribution at the OMC reflected port where only first order misalignments are taken into account. The f_{dither} field arrows shown in blue has a TEM_{01} mode due to a possible misalignment of the OMC axis as 'seen' by the f_{MI} field shown in green, which has the TEM_{00} distribution. The beat at $f_{MI} - f_{dither}$ shown by the green arrows is the MDWS signal.

The electronic circuit as shown in fig. 2.10 is used to generate a proportional feedback current. It is applied to the coils of two galvanometers (fig. 2.11) that rotate the mirrors attached to it that directs the beam to the QPDs [87].

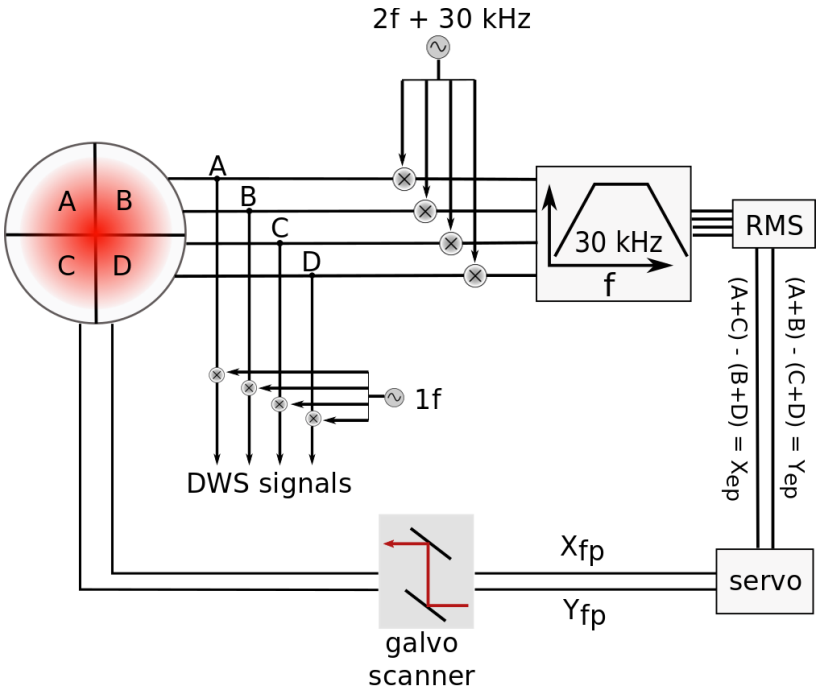

Figure 2.10: Signal flow for 2f sensing. The 1f DWS signals are also shown for completeness. The $(X,Y)_{ep}$ denote error signals and $(X,Y)_{fp}$ are the feedback signals for the x and y plane, respectively.

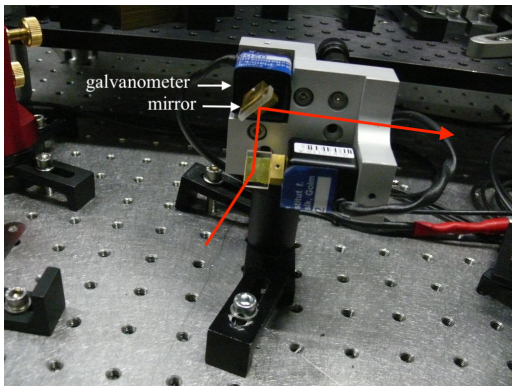

Figure 2.11: A galvo scanner used at GEO 600 for spot centring.

With regard to GEO's history, when the GW readout was changed from heterodyne to DC it was not possible to have a robust lock for more than an hour. It was attributed to spot motion on the wavefront sensors at the IFO output port where the alignment signals for the MI mirrors was generated. It was found that in DC readout there is a first order coupling of the spot position on alignment signals. Hence the 2f spot centering was developed and it proved to be crucial for the detector. A detailed description can be found in [31]. From now on, I would refer to the alignment signals as 1f and the spot centering signals as 2f.

2.4.2 Open loop transfer function measurement

The unity gain frequency (UGF) of the spot centering loops has to be considerably higher than the alignment loops UGF to reduce coupling in the feedback system. If the center of the spot is displaced by one beam radius then 86% of the DWS signal is lost [56]. A simple intuitive reason behind this is that if the spot of f_{MI} is not centered correctly on the QPD then the overlap of the fields described by eq. 2.16 and eq. 2.17 decreases, thereby reducing the overall signal. Fig. 2.12 shows a measurement of the open-loop transfer function (OLTF) of the 2f loops showing the UGF to be about 40 Hz. This is well above the UGF of 1f control which is below 3 Hz.

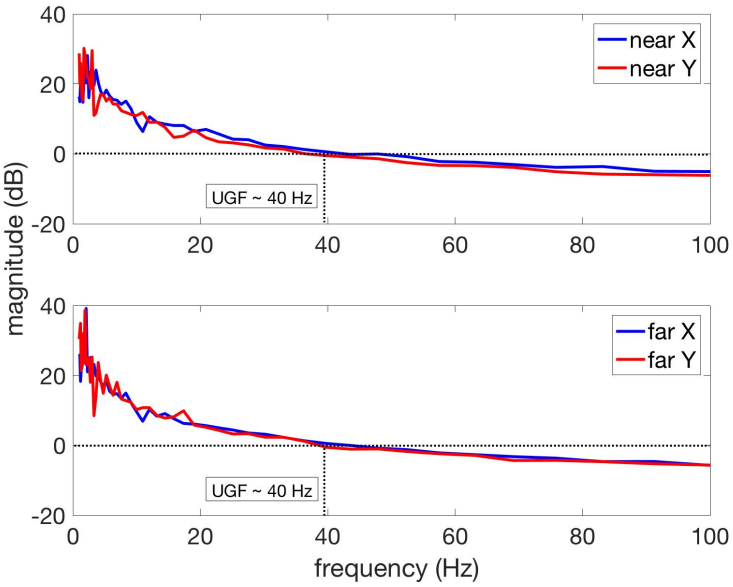

Figure 2.12: Measurement of the OLTF of the 2f loops. Top plot: far scanner. Bottom plot: near scanner

2.4.3 Setting up the sensing path

The requirement of optimal sensing for DWS is a Gouy phase separation of $\frac{\pi}{2}$ between the two QPDs. The software *A la Mode* was used to design the Gouy phase telescope as given in [44]. Given the target of having $\frac{\pi}{2}$ separation between the QPDs and optical components such as lenses and a scanner for each path, the software can calculate the position of each component to fulfil the condition. This is shown in fig. 2.13.

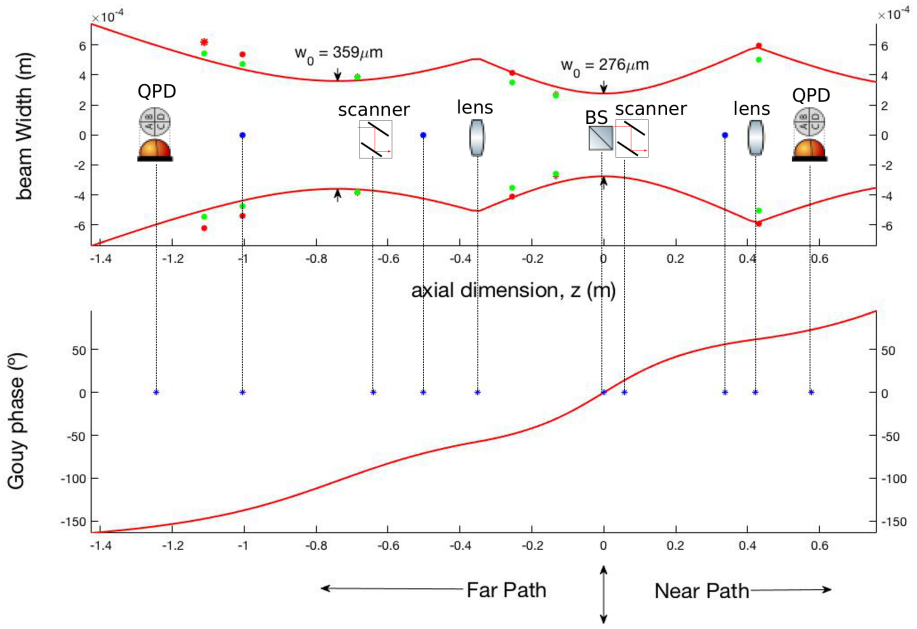

Figure 2.13: The beam profile and the position of optical components for the near and far detection path. The common waist is at z=0 at which the beam gets split in a 50:50 ratio. This entire setup is located in air for easy access. The blue dots without label are reflecting mirrors and 'BS' is a 50:50 beam splitter. The red and green dots show measurements of the beam profile for the horizontal and vertical axis.

2.5 The BDO actuators

The BDOs are three single stage suspensions located at the IFO output as shown in fig. 1.3. BDO1 in combination with a pair of lenses forms the output telescope that serves the purpose of focusing the beam. BDO2 and BDO3 being flat optics direct the beam to the OMC. For OMC AA schemes, BDO1 and BDO3 are used as steering mirrors.

The design of the BDOs remains the same as described in [59]. The properties of the optics are given in table 2.2 and the details of the suspension are given in table 3.1. Due to not being part of a cavity, the seismic isolation requirement for the BDOs is not harsh. It is therefore sufficient to have cantilever springs damped by passive eddy current dampers for vertical isolation. For horizontal sensing and actuation, local control is used that consists of shadow sensors and coil-magnet actuators as described in the following section.

	BDO1	BDO2	BDO3
Thickness	49.8 mm	49.6 mm	49.7 mm
Diameter	99.7 mm	99.99 mm	99.8 mm
Focal length	3.35 m	planar	planar
Material	fused silica	fused silica	fused silica

Table 2.2: The BDO suspension parameters as taken from [58].

2.5.1 The Local control

The Local Control (LC) is a feedback system that damps the eigenmodes of the suspensions and provides low frequency control [59], [65]. The BDO has six DoFs - rotation (rot), tilt, longitudinal, side, roll and bounce. The LC damps the rot, tilt, longitudinal and side degrees while the roll and bounce are damped by eddy current dampers placed at the edge of cantilever springs from which the BDO optic is suspended via steel wires as shown in fig. 3.3.

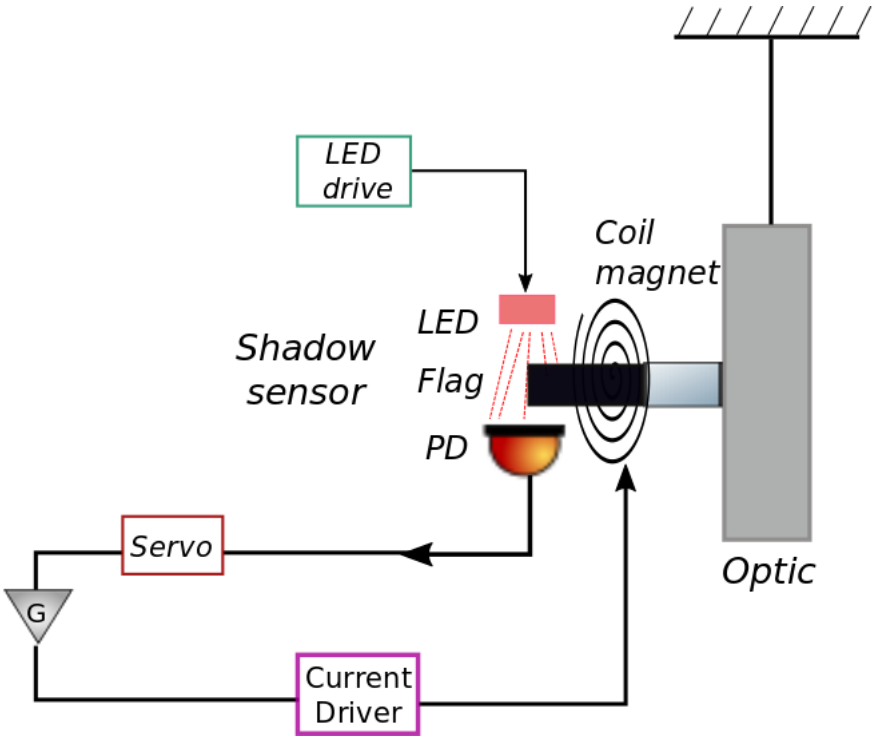

Figure 2.14: Simple schematic of the components of a co-local damping loop.

To detect the motion of the test mass.r.t the suspension point there is a so-called shadow sensor arrangement as shown in fig. 2.14 which is also called a displacement sensor. It consists of an air-core electromagnet (coil) with a LED and a photodiode facing opposite to each other which is encapsulated in vacuum compatible glass, called as OSEM. There is a magnet and a flag attached to the optic such that the flag is inserted in the air-core part and partially prevents the light of the LED from reaching the photodiode. If the flag moves due to the displacement of the optic, the light of the LED reaching the photodiode changes and a proportional current is generated. This current is filtered and sent to the co-located coil as feedback current. This type of damping is also known as *co-local damping*. There is another kind of damping called as *degree-of-freedom damping* in which individual OSEM signals are combined to damp a DoF of the suspended optic. The idea of such a system was first conceived by [62].

The components of the LC are:

- The shadow sensor that is made up of
  - An OSEM : an electromagnet coil with an air core, a LED and a photodiode
  - A magnet and a aluminium flag
- A current driver for the OSEM coil
- A current source for the OSEM LED
- Transimpedance amplifier (TIA)
- Analog filters
- An addition point for low frequency feedback (not shown here)

2.5.2 Optical Sensors and Electro Magnetic actuators (OSEM)

The OSEMs for the GEO 600 suspensions were developed at the Institute of Gravitational Research, Glasgow. They were initially made in a set of two groups (see fig. 2.15). The BDOs use the first kind with a typical coil resistance (R) of $\approx 280\,\Omega$. The LED type is SFH485 and the photodiode is BPW34 on most of them with an active area of about 2.65 mm. The second kind of OSEMs have shorter coil length ($R \approx 40\,\Omega$) which was found to be optimal for the needed control. A description of the OSEMs used by the advanced LIGO suspensions can be found in [63].

(a)

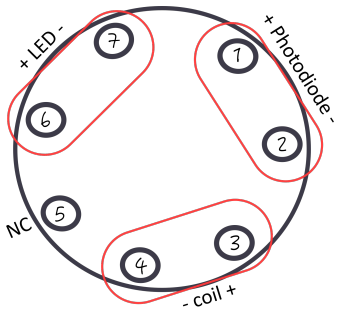

(b)

Figure 2.15: a). The two kinds of OSEMs used at GEO 600. Left: Large coil OSEM. Right: Small coil OSEM. b). Pin configuration used for electrical connections of an OSEM.

2.5.3 Coil-magnet force measurements

There is a unique *sweet spot* for placing the magnet w.r.t. coil where the force exerted by the coil due to a given input current is maximum [64]. The coil-magnet force measurement was done for the two kinds of OSEMs with small cylindrical magnets of varying sizes: 10 mm diameter, 3 mm thickness (used by the BDOs) and 10 mm diameter, 10 mm thickness. The magnet sizes were chosen based on information in [58], [59]. For this measurement, a few spare OSEMs were collected and the measurement was performed at the AEI electronic workshop. The result is shown fig. 2.16 and summarised in table 2.3.

At the maxima of the curve, the derivative of force vs the position of the magnet is zero. This implies that if the distance between the coil and the magnet changes due to a displacement of the OSEM mount (due to ground seismic noise) then it will have no effect on the applied force. In other words, the actuation will be decoupled from seismic noise coupling. This is the sweet spot for the magnet.

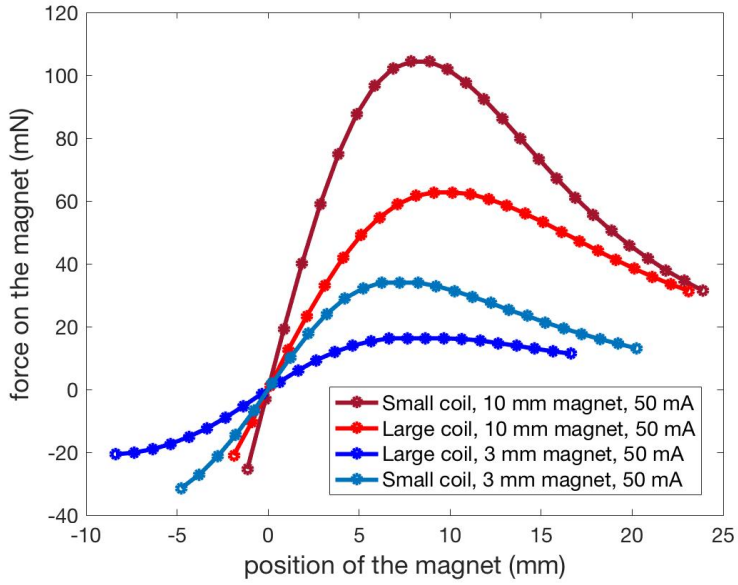

(a) Using an input current of 50 mA

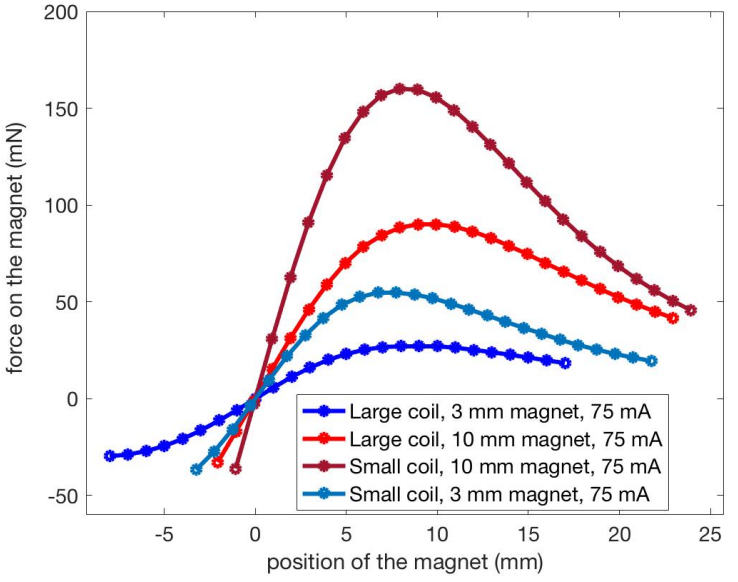

(b) Using an input current of 75 mA

Figure 2.16: The force exerted by the coil vs the position of the magnet using two different input coil currents.

	Peak force (mN) at 50 mA	Peak force (mN) at 75 mA
Large coil, small magnet	16.27	27.05
Large coil, large magnet	62.72	90.06
Small coil, small magnet	34.00	54.70
Small coil, large magnet	104.3	160.1

Table 2.3: Results of the measurement shown in fig. 2.16 for the various combinations of coil-magnet and input current.

Another measurement was made for the force on the magnet due to varying coil current as shown in fig. 2.17 which is a straight line with a slope of 0.72 N/A.

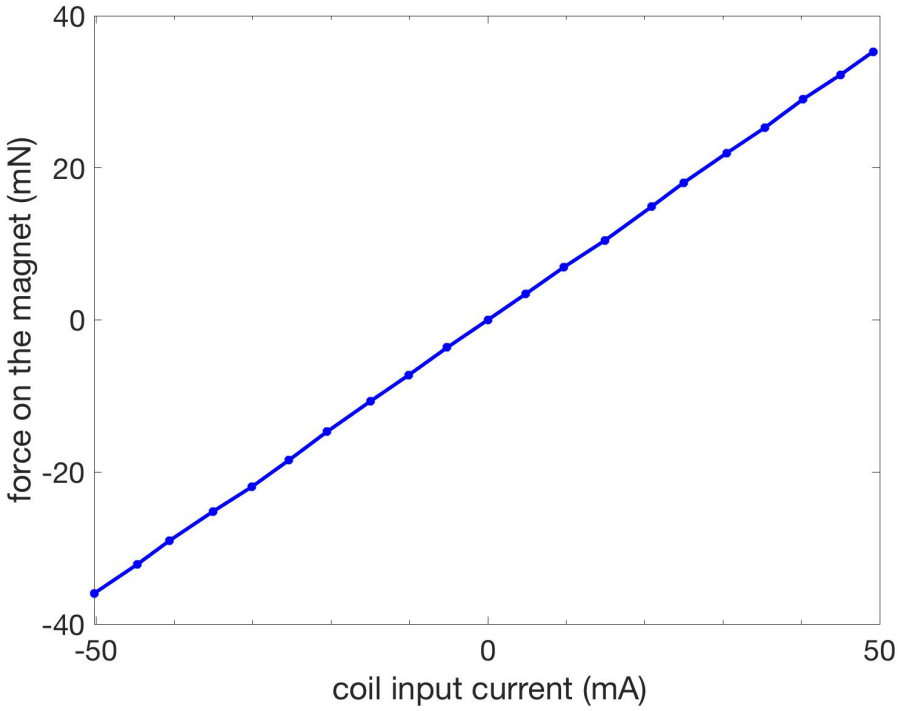

Figure 2.17: Measurement of force on the magnet due to varying input coil current.

2.5.4 Measurement of the linear range of the OSEM

The photodiode that senses the position of the flag and converts it into a proportional current has to be well-calibrated. This requires measurement of the photodiode output vs the position of the flag as shown in fig. 2.18. The table 2.4 summarizes the results of the measurements.

From fig. 2.18, the desirable position at which the flag should be placed is within the region where the derivative of the photodiode output signal w.r.t the flag position, in other words, its displacement sensitivity is maximum. This corresponds to about 5 mm of linear range between the flat portions of the curves. The lower flat portion where the output signal is close to zero corresponds to the photodiode being completely covered with the flag so that no light reaches it. Gradually, as the flag is moved to uncover the photodiode, the signal rises through the linear region to the upper flat portion where the flag is completely removed. Here the photodiode signal gets saturated and the position of the flag can no longer be determined correctly.

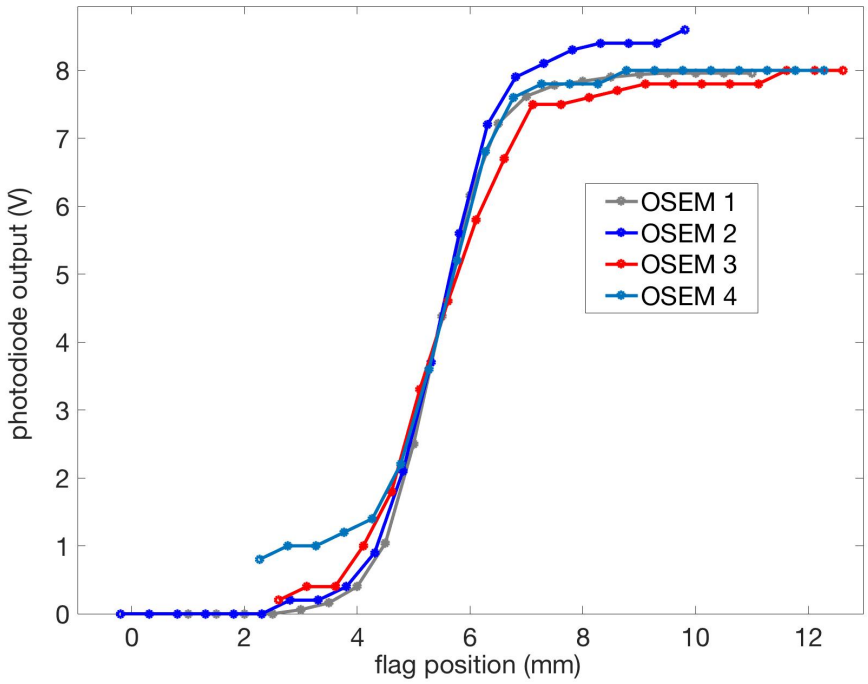

Figure 2.18: Measurement of the OSEM linear range. The OSEM 3 has a small coil while the other three have larger coils as shown in fig. 2.15.

	Outer diameter	Inner diameter	Height	Linear sensitivity	Total range
OSEM 1	5.40 cm	1.73 cm	3.90 cm	-2.40 V/mm	5.00 mm
OSEM 2	5.40 cm	1.81 cm	3.80 cm	-2.47 V/mm	4.50 mm
OSEM 3	5.60 cm	1.83 cm	3.50 cm	-2.20 V/mm	5.00 mm
OSEM 4	5.38 cm	1.58 cm	3.77 cm	-2.48 V/mm	5.50 mm

Table 2.4: Measurements of OSEM dimensions and the sensitivity.

2.5.5 Transfer function measurements of the BDO suspensions

Each BDO suspension has four LC feedback loops where the OSEMs are fixed to a support structure that is clamped to the bottom of the vacuum tank as shown in fig. 2.19a. The BDO DoFs can be addressed by actuating through the OSEMs in the following combination:

long = OSEM 1 + OSEM 2
tilt = OSEM 1 - OSEM 2
rot = OSEM 3 - OSEM 4

The separation (d) between the top-bottom and right-left OSEMs is not equal. This leads to unequal torques (τ) being generated for the rot and tilt DoF as represented in fig. 2.19b and can be calculated as:

$\tau_{\text{tilt}} = \text{F} \times \text{d}$; d= 6.45 cm
$\tau_{\text{rot}} = \text{F} \times \text{d}$; d= 2 cm
Assuming equal force (F) on both degrees,
$\tau_{\text{tilt}} \approx 3.2 \times \tau_{\text{rot}}$

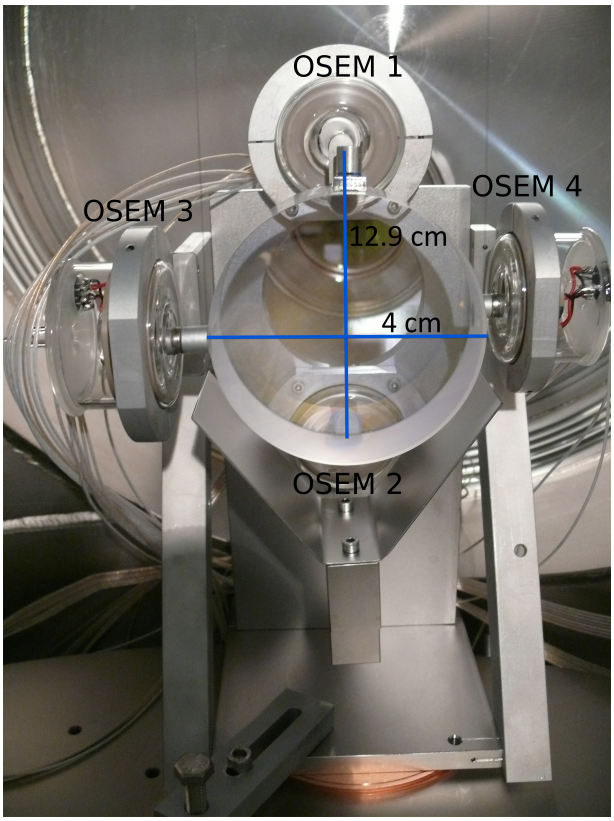

(a)

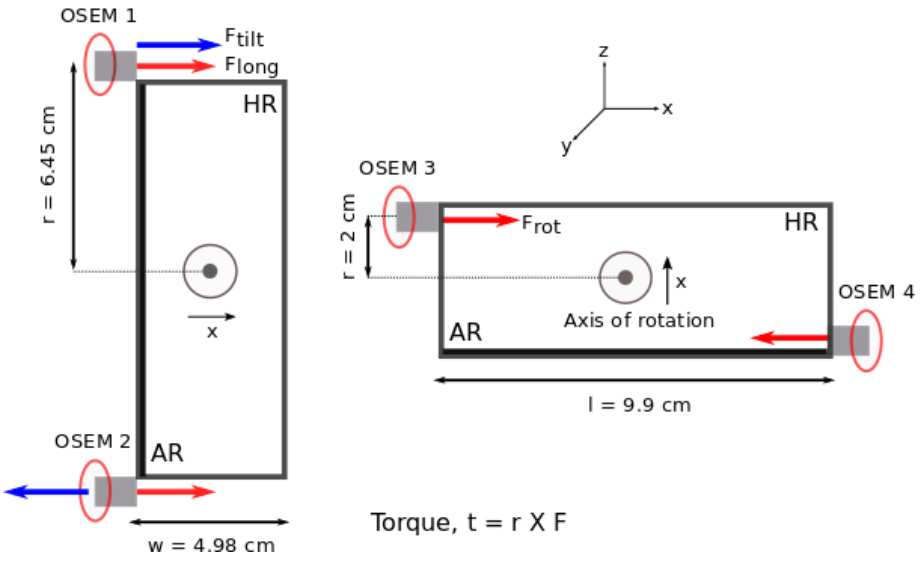

(b)

Figure 2.19: a). Front view of the BDO2 suspension and the four OSEMs. b). The BDO optic viewed from the side and from top. The x direction is the one in which the IFO beam is reflected from the BDO and z is the direction in which the optic is suspended at the suspension point. The arrows show the direction of actuating force (F).

For alignment actuation the relevant DoFs of BDO1 and BDO3 is rotation and tilt. To determine the resonance frequency a swept sine transfer function is done with injection being applied through the OSEM loops with a photodiode placed in reflection of the OMC. Also, the OMC cavity length is kept off resonance w.r.t the carrier such that the carrier is reflected. The bode plots of the measurement are shown in fig. 2.20 where it is fitted with a model of a resonant low pass filter. The script for the fitting is given in Appendix A. The results are summarized in table 2.5.

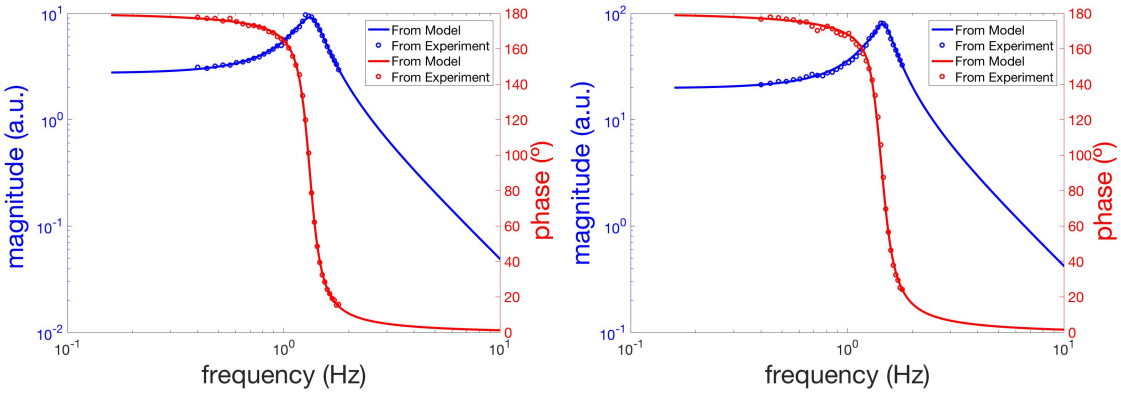

(a) BDO1 Rot

(b) BDO1 Tilt

(c) BDO3 Rot

(d) BDO3 Tilt

Figure 2.20: Results of the transfer function measurements for BDO1 and BDO3 suspension for rot and tilt DoFs.

The measurements show that BDO3 tilt has a different resonance frequency which was not expected before the measurements were made. It is just a technical issue that has been explained in chapter 3.

	Rot (Hz)	Q	Tilt (Hz)	Q
BDO1	1.34	2.79	1.43	4.34
BDO3	1.30	2.02	0.75	5.20

Table 2.5: The measured BDO resonance frequencies and Q values

2.6 General design requirements for an optimal control system

The DoFs of a system can be expressed as orthogonal axes in a coordinate system forming a DoF space [75],[76]. The actuators and sensors can be expressed as vectors in this space as shown in fig. 2.21. For a sensor or actuator pair to be orthogonal, the accumulated Gouy phase between them must be $\frac{\pi}{2}$ radians. In an experimental setup, the initial position of actuators and sensors can be obtained by modelling of the beam parameters using tools like *just another mode matching tool* (JamMT) or *A la Mode* [74].

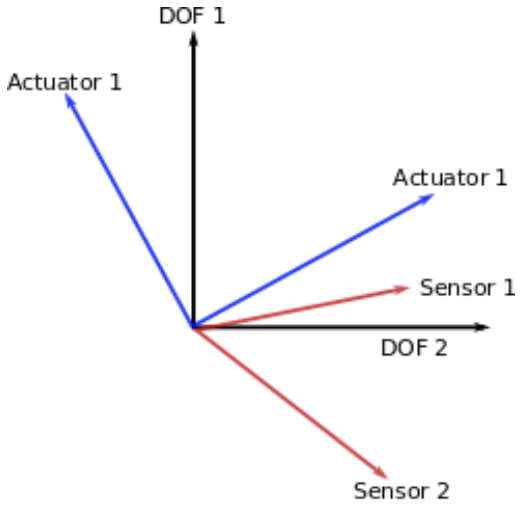

Figure 2.21: A general representation of an ideal set of actuators and sensors shown as vectors in the DoF space. Well separated sensors and actuators will span the DOF space sufficiently.

In a linear system, the sensor ($\vec{S}$) to actuator ($\vec{A}$) will have the following relation

$$\vec{S} = M\vec{A} \tag{2.25}$$

where, the matrix M is called the sensing matrix and is of the form $\mathrm{M} = \begin{bmatrix} a & b \\ c & d \end{bmatrix}$, $\vec{A} = \begin{bmatrix} A_1 \\ A_2 \end{bmatrix}$ and $\vec{S} = \begin{bmatrix} S_1 \\ S_2 \end{bmatrix}$.

To create a common basis between the sensors and actuators, the sensor signals have to be transformed back into the actuator basis. This can be done by computing the inverse of M which is called the input matrix (or decoupling matrix), such that

$$M^{-1}\vec{S} = M^{-1}M\vec{A} \tag{2.26}$$

$$\vec{A} = M^{-1}\vec{S} \tag{2.27}$$

To determine the sensing matrix, an actuator can be excited at a known modulation frequency which in general will create signals in both the sensors. This has to be repeated for the second actuator as well that provides the 4 x 4 sensing matrix which is then inverted to get the input matrix. Similarly, there is an output matrix that determines the combination in which control signals are applied to the actuators. Usually, one of the two matrices (input or output) is chosen to be a diagonal matrix. This means that the servo filter has to be shaped differently in each case forming the servo basis (diagonal input matrix) or the actuator basis (diagonal output matrix) shown in fig. 2.22. For implementing MDWS at GEO 600, both kinds of basis were used and the results are discussed in the next section.

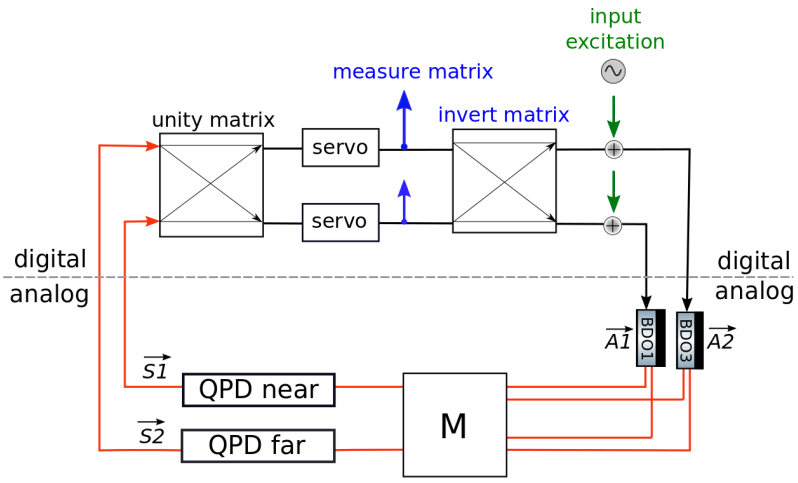

(a) Sensor basis

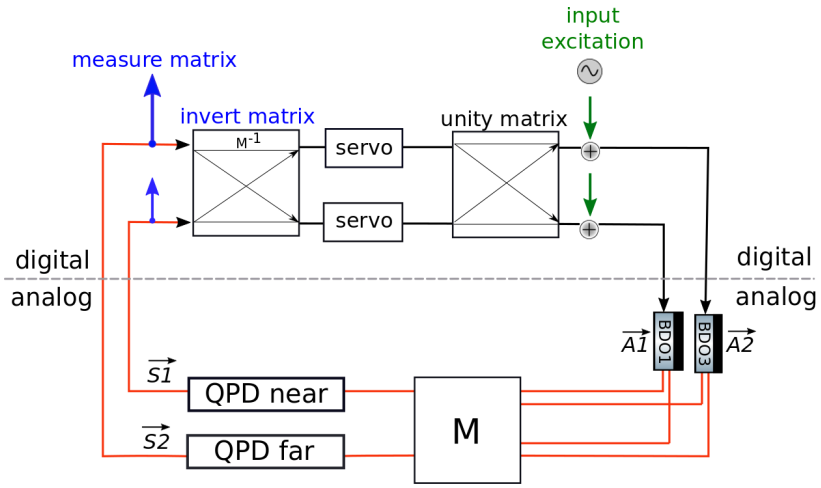

(b) Actuator basis

Figure 2.22: Simple schematic for the choice of the basis in a feedback loop. In fig. a, b, the matrix on the right of the servo is the input matrix and on the left is the output matrix. The point of injection of the modulation is indicated by the green arrow whereas the blue arrow shows the point where the sensing matrix can be measured.

2.7 Implementing MDWS

2.7.1 Preliminary demonstration and motivation for MDWS

The first demonstration of MDWS was done by closing an AC coupled loop with a bandwidth from 0.1 Hz to 3 Hz as described in [36]. The alignment onto the OMC was dithered at 0.3 Hz, 0.6 Hz, 1.1 Hz and 2.1 Hz using injections into the LC of BDO2 (see fig 2.8) and suppressed using a combination of actuation on BDO1 and BDO3. To check the validity of the loop, an out of loop measurement was set up by dithering BDO3 at a frequency of 542 Hz. This produced a spectral line at the dither frequency as well as sidebands due to the injected lines in the GW strain channel as shown in fig. 2.23b, which the loop was able to suppress. This successful preliminary result for one DoF led us to further investigation of the MDWS technique as given in the following sections.

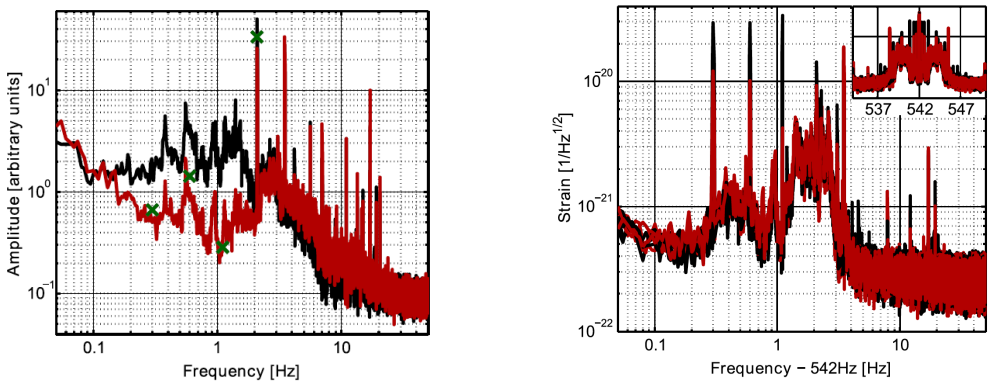

(a) (b)

Figure 2.23: a). Open (black) and closed (red) loop error point spectra of the loop showing the suppression at the injected frequencies marked by green crosses. b). The out of loop measurement showing line height reduction at the injected frequencies. In the inset, the 542 Hz is shown along with the sideband structures. The main figure shows only one side of the sideband structure. Both of these figures have been taken as it is from [36].

2.7.2 Sensor basis

The MDWS servo was initially set up in the sensor basis. It was observed that the loops would become unstable over the period of a few minutes. We investigated and observed coupling between the loops. Fig. 2.24 shows an example of coupling where a sine wave was injected in the near Y loop and in the absence of coupling it should not appear in the far Y loop.

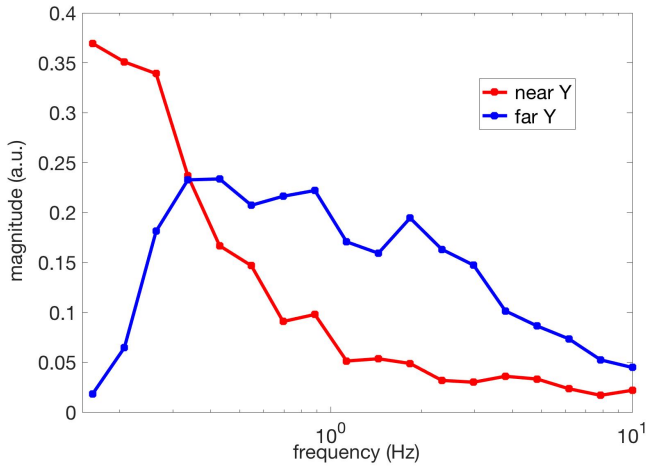

Figure 2.24: Coupling between the MDWS tilt loops in the sensor basis

To reduce the effect of coupling two steps were taken. First, a DC offset is added in the loop and the response of all the other loops is measured that gives the initial decoupling matrix as shown in fig. 2.25b. Second, with the initial decoupling matrix in place, the noise injection is repeated and the matrix is re-measured to give a second matrix as shown in fig. 2.25a. The result is shown in fig. 2.25a where the response in other loops is minimized.

This improved the stability of the loops such that they were stable up to a few hours instead of minutes. Due to the sub-optimal Gouy phase separation of about 8° between BDO1 and BDO3 the actuators have to move a lot to span the full DoF space that causes coupling in actuation. Therefore the servo was changed to the actuator basis in which a combination of sensor drives each actuator separately instead of the sensor basis in which the actuators are driven in a combination of sensor signals.

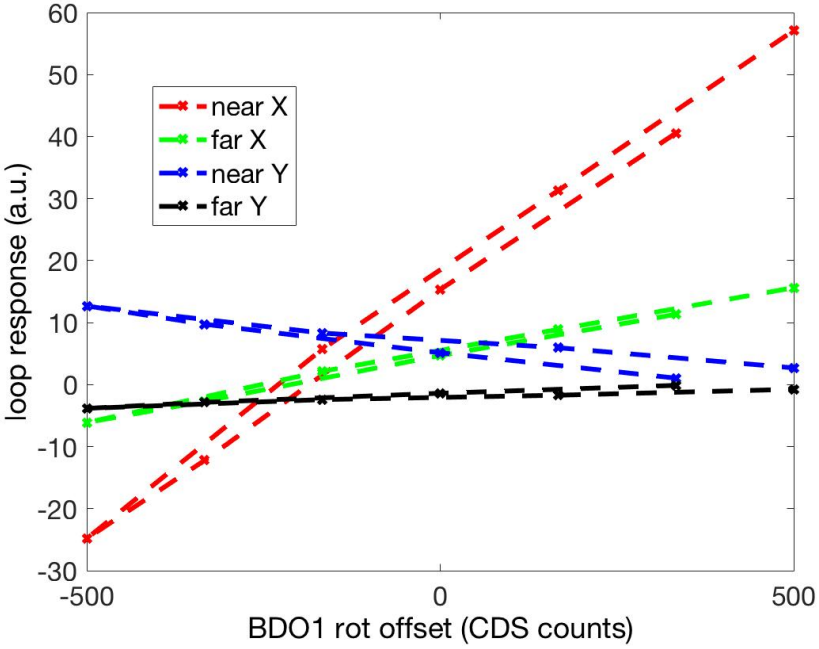

(a)

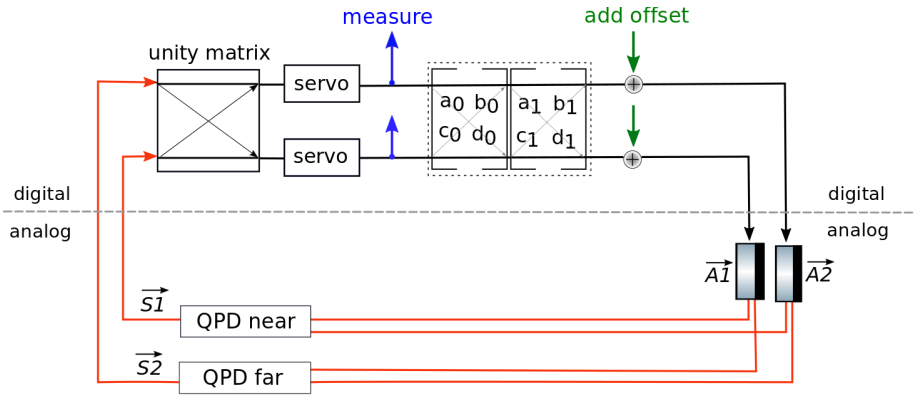

(b)

Figure 2.25: a). The four QPD signals vs offset introduced in the BDO1 rot loop after two steps of decoupling. The final output matrix is given by the product of the initial matrix (subscript 0) and the first decoupling matrix (subscript 1). The slopes of the three traces being small indicates that the loops are fairly decoupled. b). The schematic of the loop for the measurement.

2.7.3 Actuator basis

In the actuator basis, the decoupling matrices were re-measured. Also to reduce the actuation noise, a gain hierarchy was used such that BDO1 rot and tilt loops are at a higher gain than the BDO3 rot and tilt loops. Due to the difference in gains the *stronger* loops compensate much more for the misalignment than the *weaker* loops. Eventually, all the four loops were made stable with UGF between DC to 2 Hz for the weaker and the stronger loops, respectively, as shown in fig. 2.23a. To make sure that no additional noise is added in the GW channel noise projection was done as shown in the next section.

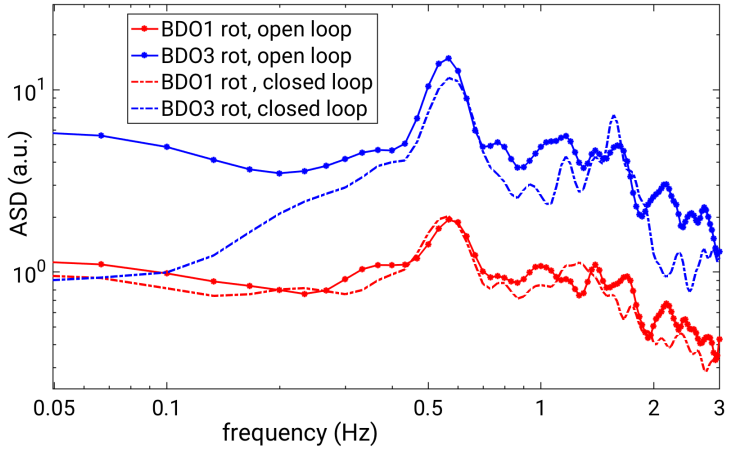

(a) Error spectrum for the rot loops

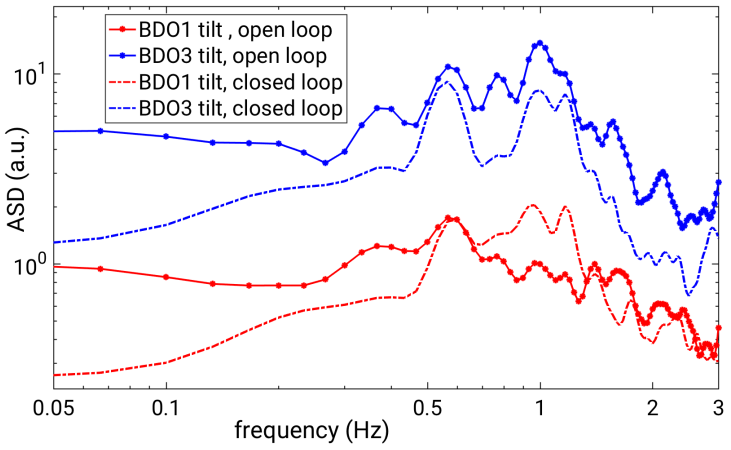

(b) Error spectrum for the tilt loops

Figure 2.26: The open and closed loop error spectra of the MDWS signals.

2.7.4 Noise projection onto h

An important quantity to estimate is the noise coupling of a subsystem to the GW channel, h. This can be represented by a noise projection. The procedure is to inject noise in the channel (N_j) of interest such that it is the dominating noise source in the channel itself as well as the h channel for a given time. This gives a complex transfer function (α). The next step is to compute the discrete Fourier transform (DFT) of both channels simultaneously for a default operating state of the detector. The noise projection is given by the product of α and the DFT of the noise channel. This procedure is described in detail in [77].

The noise of the MDWS feedback channels was projected onto h and the result is shown in fig. 2.27. It was sufficient to do the measurement up to 100 Hz as the coupling reduces gradually at high frequencies due to a roll off in the feedback signal to the BDO actuators.

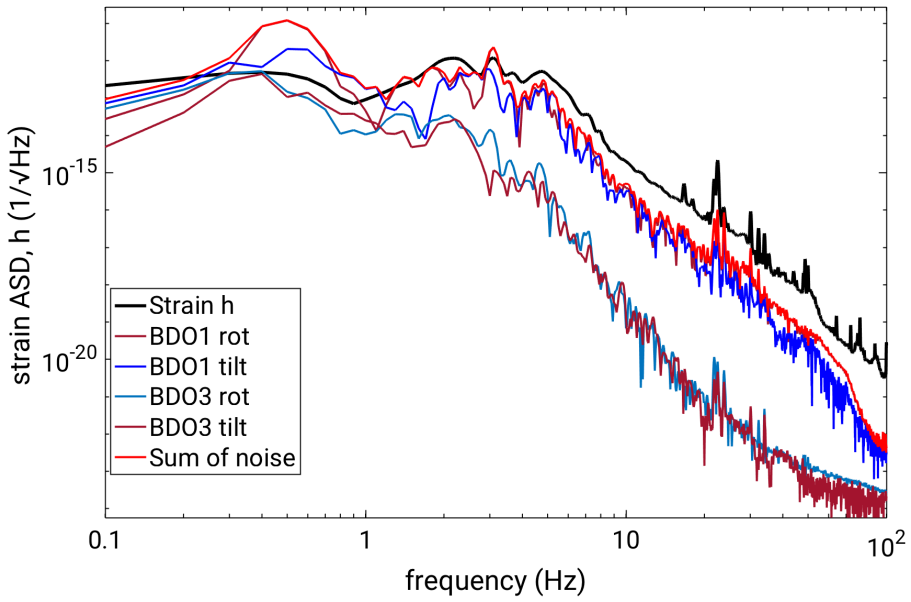

Figure 2.27: The noise projection of the MDWS feedback signals to h. Below 1 Hz, h is dominated by the feedback noise but reduces gradually for higher frequencies.

2.8 Challenges

On day scale, the MDWS loops showed a DC drift that would misalign the IFO beam w.r.t. the OMC. Since the DFO of the MI IFO is adjusted according to the OMC transmitted power, this compromised the stability of the detector. Another challenge arose when it was observed that the 2f loops generated an error signal in the absence of any light on the QPDs which was suspected to be a leakage of the 1f LO to the 2f path as they were connected through a common soldered joint as seen in fig. 2.10. This design was corrected by constructing new electronic modules for the 1f and 2f path such that the two signals were split through a high frequency splitter module as given in Appendix B.

The new electronic rack was installed in the cleanroom at GEO 600. It was found that the Michelson would drift out of lock as soon as the MDWS electronics would be turned on. To better investigate this behaviour, the path of all the relevant cables were tracked to the RF bench where the LO is generated. The grounding of some signal lines was made checked and made consistent at the time of writing the thesis. Additionally, as a long term improvement, the spot centring servo is being migrated to CDS [79]. This will ensure minimal cross-talk between the demodulation electronics.

To be able to understand the effect of various noise sources that can affect MDWS without disturbing the operation of the detector a separate study was done i.e. building a noise budget for the system using modelling tools. The procedure and the results are described in detail in chapter 3.

CHAPTER 3

MDWS noise budget using modelling tools

Noise can have several forms. It can be explained as any unwanted disturbance in a measurement. For a system like MDWS, noise can show up in several forms such as seismic noise, sensor noise, LED intensity noise, etc. A plot of all known sources of noise calibrated to show their contribution to a channel of interest is called a noise budget. It helps in tracking the dominant noise sources and in reducing them eventually.

In practice, creating a noise budget is a process with the following steps:

- Determine all the possible sources of noise that can contribute to a measurement channel.
- Measure (or model based on the knowledge of the system) ASD of the noise source.
- Measure (or model based on the knowledge of the system) the transfer functions from each source of noise to the measurement channel.
- Propagate the noise spectrum of the source to the measurement channel.

The first step in building a noise budget is to have a stable control model with a tool like Simulink which is a Matlab based simulation environment [60]. The noise sources and probes can then be added at several places in the model to look at the quantity of interest. This approach is followed to get a noise budget for the MDWS AA scheme as described in this chapter. A unique feature of this work is in using a combination of several modelling tools. The study of noise present in a system is crucial for troubleshooting

the dominating noise sources that can pose a problem in the long term operation of the system.

Fig. 3.1 shows the top layer of the MDWS control model built in Simulink. It consists of the BDO actuators, the local control and the 1f and 2f feedback loops. As can be seen, BDO2 is also modelled to include the noise sources associated with it but is not part of the MDWS feedback loops. Three triple stage suspensions have been modelled as a replacement of the input optics and IFO (see fig. 1.3) such that the optical simulation model is simplified. It should be mentioned that the BDO suspension modelling has been done using a tool-kit in Mathematica [61] but the triple suspensions are simple second-order resonant low pass filters with a $\frac{1}{f^6}$ frequency response.

The optical plant is modelled using Finesse [80], [81] which is a widely used optical simulation tool and SimulinkNb (a Simulink based toolkit) is used for noise input as well as for plotting the noise budget. A description of the usage of SimulinkNb is given in Appendix D. The details of the modelling of each component (also called block) is given in the following sections.

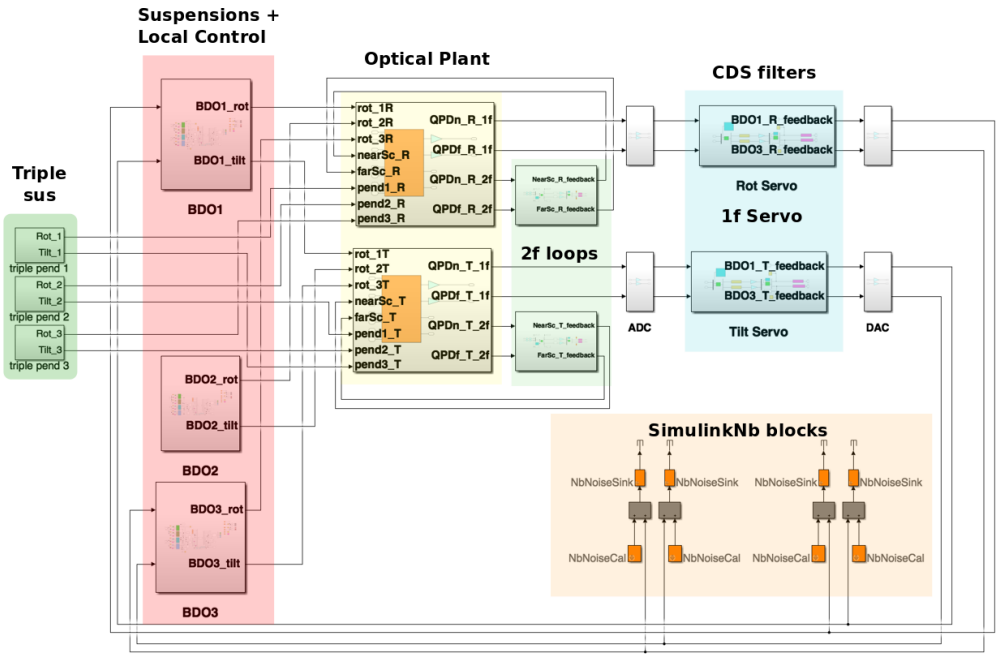

Figure 3.1: The top layer of the MDWS control model showing the various components. The layer beneath the top layer is faintly visible.

3.1 The noise inputs in the model

As illustrated in fig. 3.2 the overall control model is built with Simulink in combination with different tools as labelled inside the respective blocks. The orange coloured tags are for noise input to the model through the SimulinkNb tool which is a toolkit used for noise budget plots. The noise inputs are in units of ASD where most were measured at the GEO 600 site or at the AEI.

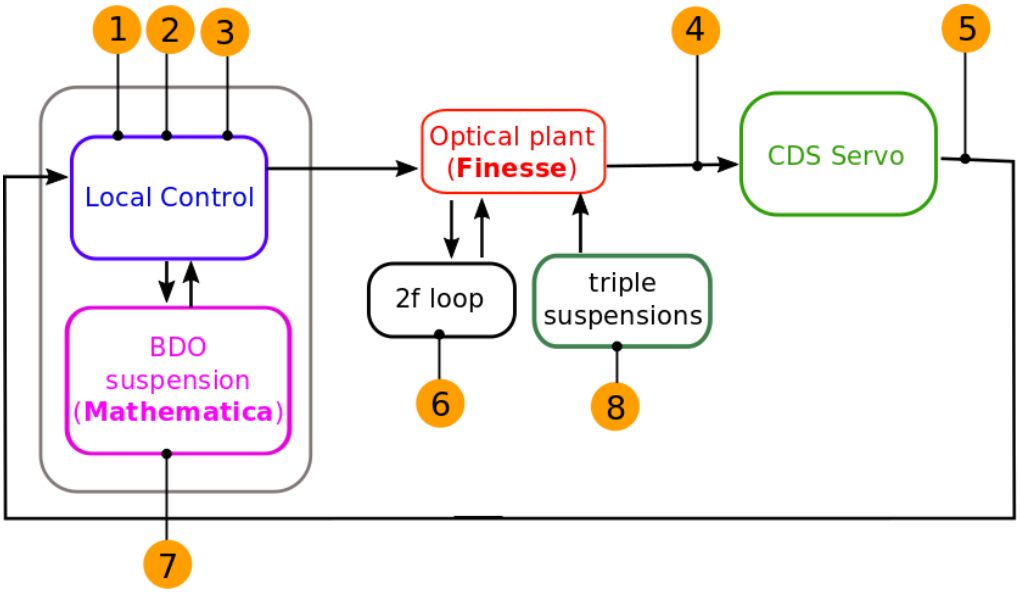

Figure 3.2: Simplified schematic of the MDWS model showing the points of noise injection.

The noise sources added in the model are as follows:

- 1 : intensity noise of the OSEM LED
- 2 : noise of the current driven through the OSEM coil
- 3 : seismic noise injection through the OSEM mounts
- 4 : ADC noise estimated to be 3.5e-6 $V/\sqrt{Hz}$
- 5 : DAC noise estimated to be 1e-6 $V/\sqrt{Hz}$
- 6 : seismic noise injection through the scanners
- 7 : seismic noise injection through the suspension point of the BDOs

- 8 : seismic noise injection through the three triple suspensions

3.2 Modelling the BDO suspension

It can be recalled from section 2.4, the BDO1 and BDO3 suspensions are used as alignment actuators for the MDWS technique. As already mentioned, the BDO2 suspension is also included in the model although feedback is not applied on it through the MDWS loops. Its modelling is identical to the BDO1 suspension.

The BDO suspensions have been briefly described in section 2.5 and further details are given in table 3.1 that have been compiled from [58],[59]. Based on these parameters a Mathematica model developed by Dr. Mark Barton [83] is used to extract the dynamic response of the suspension called the state-space representation. While the model for a single stage suspension was already existing, it was improved to include the twist of the cantilever blades for the BDO suspenion modelling. The model is based on a Lagrangian formulation of the system that outputs the state-space matrices of the suspension and can be accessed with LIGO credentials at [84]. The procedure to create user defined cases of the model is given in brief in Appendix F.

As was stated in section 2.20, the BDO3 tilt resonance frequency was found to be different from that of the BDO1 tilt resonance. The reason for this difference was unclear at the time of measurement. However, the modelling of the suspension indicated that if the parameter d (table 3.1, also see fig. 3.3) was chosen to be different from that of BDO1 then the difference could be explained. Using a value of d = -0.006 m, there is close agreement between the model and the measurement for the value for the BDO3 tilt resonance frequency. This implies that the point of attachment to the optic is below the center of mass of the optic or the optic is attached upside down (180° off in roll). In table 3.2, the measurement of the resonance frequencies of the six DoFs of the suspensions is compared with the results of the model. The close agreement between them therefore confirms the implications that has been drawn from the model.

Parameter	Value
Blade length	0.185 m
Blade width minor	0.01 m
Blade width major	0.018 m
Optic diameter	0.0997 m
Optic thickness	0.0498 m
Suspension point to standoff length	0.46 m
Distance from optic com to wire standoff BDO1 (d)	0.00 m
Distance from optic com to wire standoff BDO3 (d)	-0.006 m
Wire separation BDO1 (dx)	0.002 m
Wire separation BDO3 (dx)	0.003 m
Material	Fused silica
Mass of optic	860 g
Wire separation BDO3	0.003 m
Young's modulus of steel wire	200 GPa
Radius of steel wire	63.5 µ m

Table 3.1: BDO suspension parameters used as input for the Mathematica script.

DoF	Experimental	Model (BDO1, BDO2)	Model (BDO3)
x (long)	0.734 (0.56 for BDO3)	0.734	0.60
y (side)	0.73	0.736	0.736
z (vert)	X	3.828	3.828
tilt	1.426 (0.756 for BDO3)	1.48	0.789
rot	1.30	1.32	1.32
roll	X	5.605	5.44

Table 3.2: BDO suspension resonances (in Hz): Measured vs model output. The X indicates that they could not be experimentally determined since those degrees are damped by the passive eddy current dampers.

Fig. 3.3 shows a BDO suspension where the input parameters used for the Mathematica script are shown. The naming convention of the DOFs of the suspension as used in the model is shown by the figure in the inset on the left.

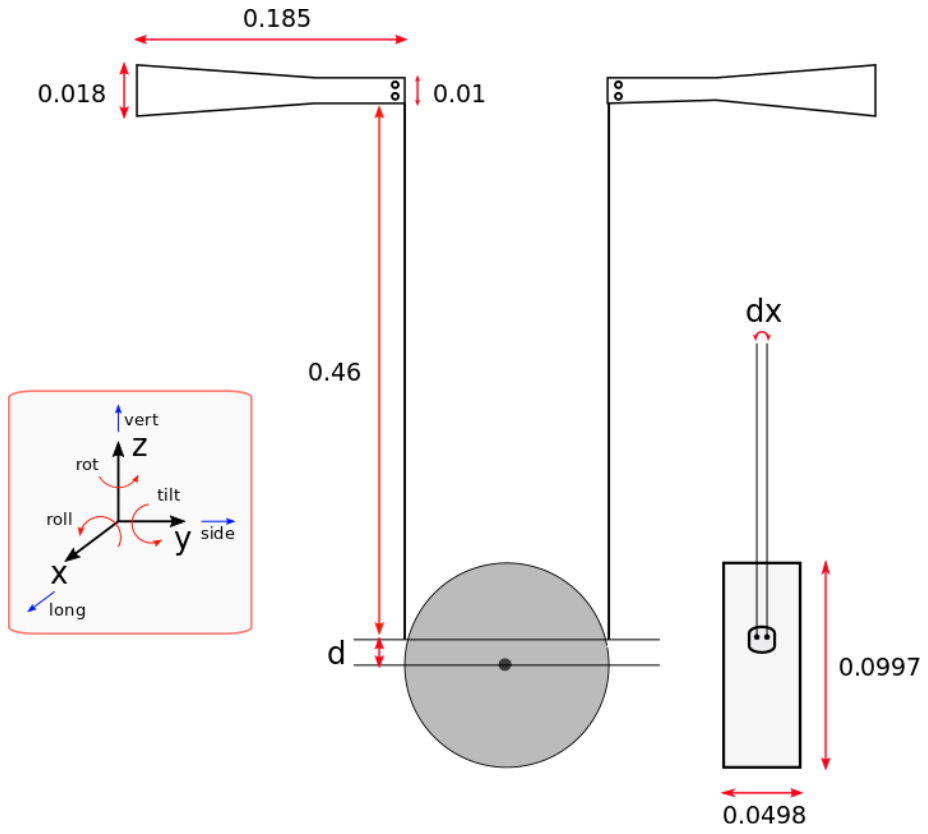

Figure 3.3: Schematic of a BDO suspension with the dimensions marked in metres. The +x direction is the HR side of the optic.

3.2.1 State Space representation

The dynamic response of a linear system can be expressed through a set of Ist order differential equations:

$$\dot{x} = Ax + Bu \tag{3.1}$$

$$y = Cx + Du \tag{3.2}$$

where, x(t) is the state vector, u(t) is the input vector, y(t) is the output vector and A (t), B (t), C (t), D (t) are matrices that connect the vectors.

The eq. 3.1, and eq. 3.2 are a mathematical representation of the physical system called the state space representation. The state variable evolves through time and is dependent on its value at a given time and input. The output in turn depends on the state vector. A similar description can be found in [85], [86]. The ABCD matrices are obtained as output of the Mathematica model of the suspension and converted into a state-space model by a single line of code to give the 'sus' block in fig. 3.4. For the BDOs, the matrices obtained is given in Appendix F.

3.3 The local control

The BDO suspension local control (LC) has been described in section 2.5.1. Fig. 3.4 shows the sketch of the LC loops where the suspension (sus) block along with the inputs and output channels form a 12x12 matrix. On the left-hand side the first six inputs correspond to the displacement of the suspension point for the six DoFs while the last six are for force inputs at the test mass. The first six outputs on the right-hand side correspond to the displacement of the test mass and the last six is the velocity of the test mass where two DoFs are damped by passive eddy current dampers on the cantilever blades.

The displacement of the test mass or sus for the six DoFs is converted into the displacement of the flags through the *Euler to OSEM matrix* which is described in the next section. The flag displacement signals go through the LC servo, which is not shown here explicitly and results in corresponding force outputs from each OSEM. *The OSEM to Euler matrix* transforms the force outputs into the test mass basis, thus closing the loops.

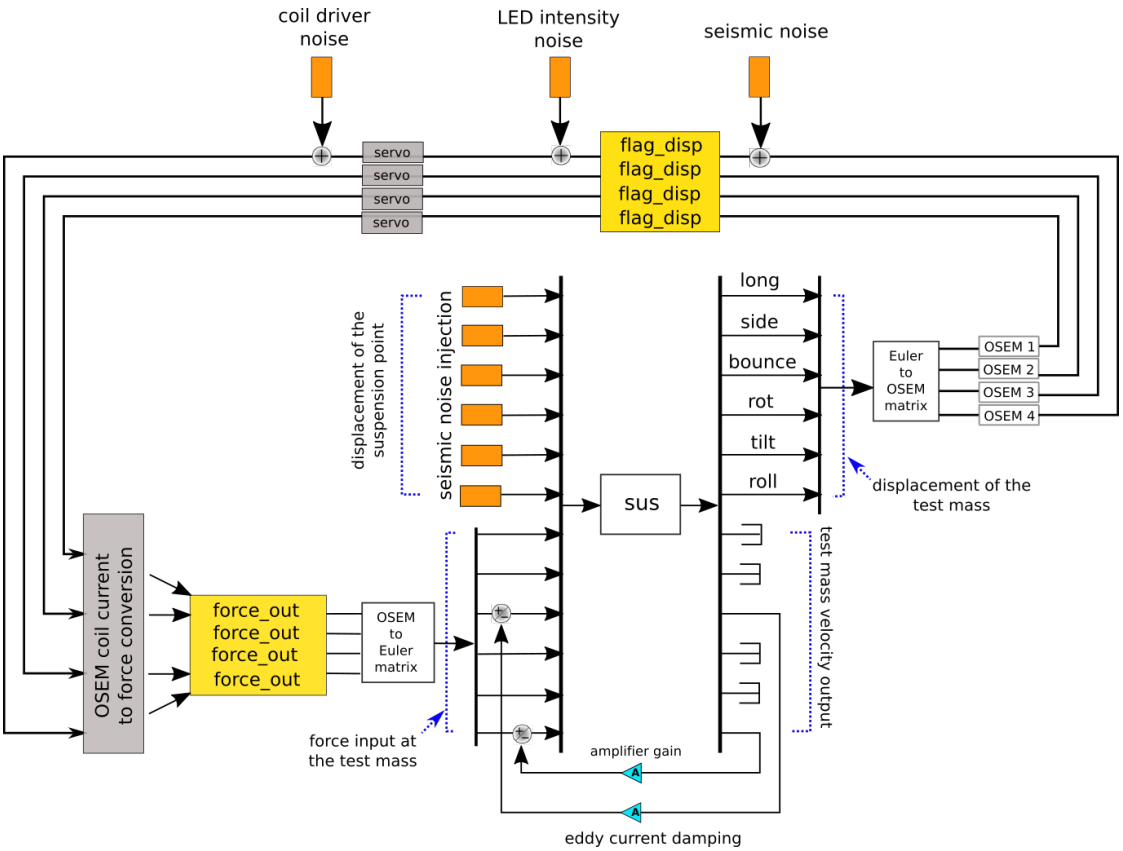

Figure 3.4: The model of the local control and the BDO suspension showing the location of noise injections. The eddy current damping of the roll and bounce degrees of the suspension is also shown.

The Simulink model of the LC servo closely follows the analog circuitry in place in order to reproduce the observed suspension response. The LC servo consists of the following units in series:

- High pass filter at 0.7 Hz
- Zero-pole pair at 0.35 Hz and 0.8 Hz, respectively
- Loop gain chosen to have Q ≈ 3 to 5
- Zero-pole pair at 2 Hz and 14 Hz, respectively
- Low pass filter at 4 kHz
- Peak-notch filter pair at (18 Hz, 25 Hz), (28 Hz, 50 Hz), (24 Hz, 45 Hz)

Fig. 3.5 shows the OLTF of the LC loop. As can be seen here, the loop acts at frequencies that are close to the 0 dB line. Here the 0.7 Hz and 1.3 Hz peaks are for the longitudinal and rotation resonance frequencies of the suspension. The step response of the LC flag signals is shown in fig. 3.6.

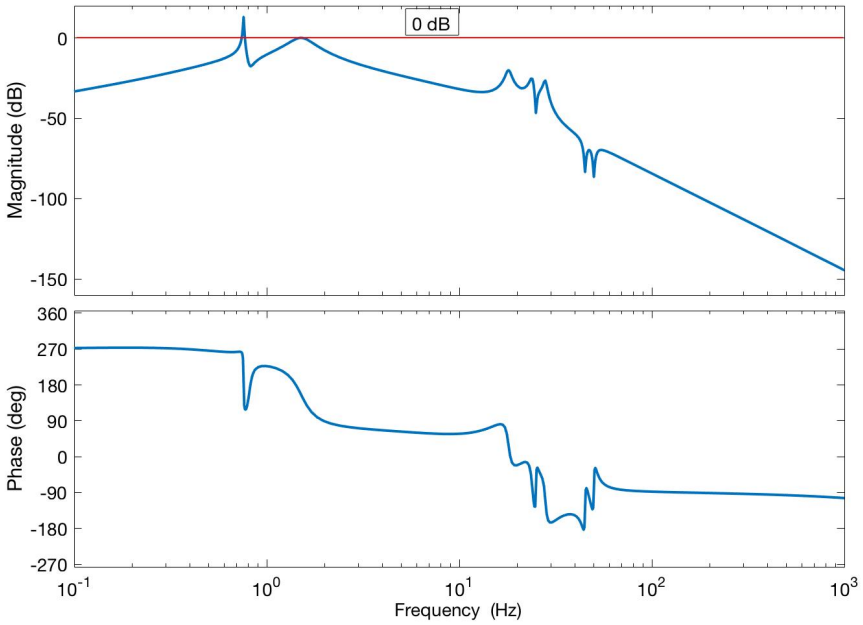

Figure 3.5: The simulated OLTF of a LC loop.

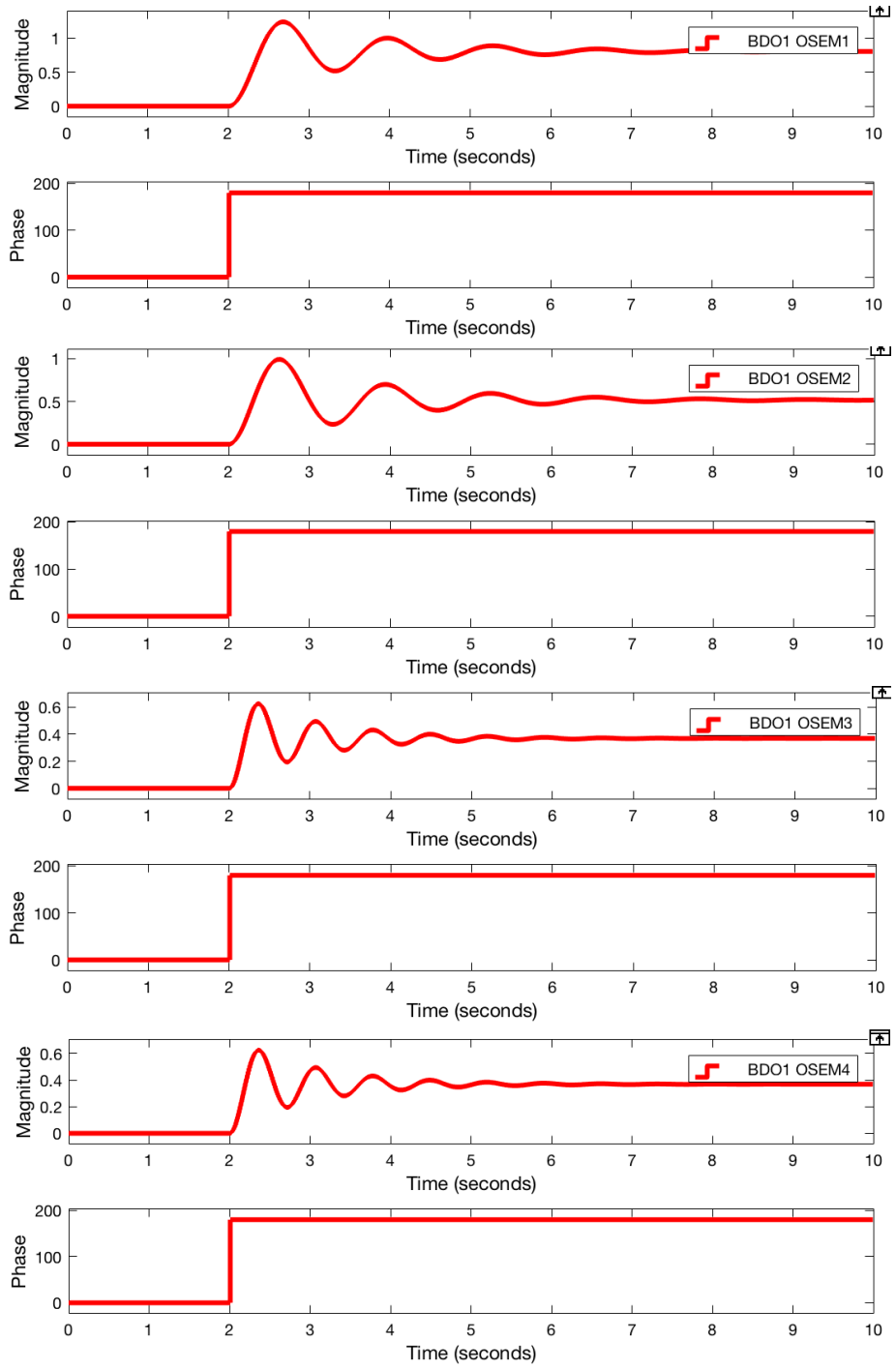

Figure 3.6: The response of the BDO1 OSEM flag signals to a step input at 2 seconds. The phase behaviour (not shown) is as expected. The gain of the loops can be adjusted to achieve the level of damping seen in the measurements made at GEO 600 of the damped suspension response.

3.3.1 Changing the basis between the OSEMs and the test mass

As shown in fig. 3.4, matrices have been used for changing the basis between the OSEM and the test mass that can be obtained from simple geometrical calculations based on fig. 3.7. Let the forces applied by the OSEMs to the optic be denoted as, F_1, F_2, F_3, F_4 and the corresponding displacement of the test mass be given as:

longitudinal, F_L
sideways, F_S
bounce, F_B
rot, τ_r
tilt, τ_t
roll, τ_{rl}

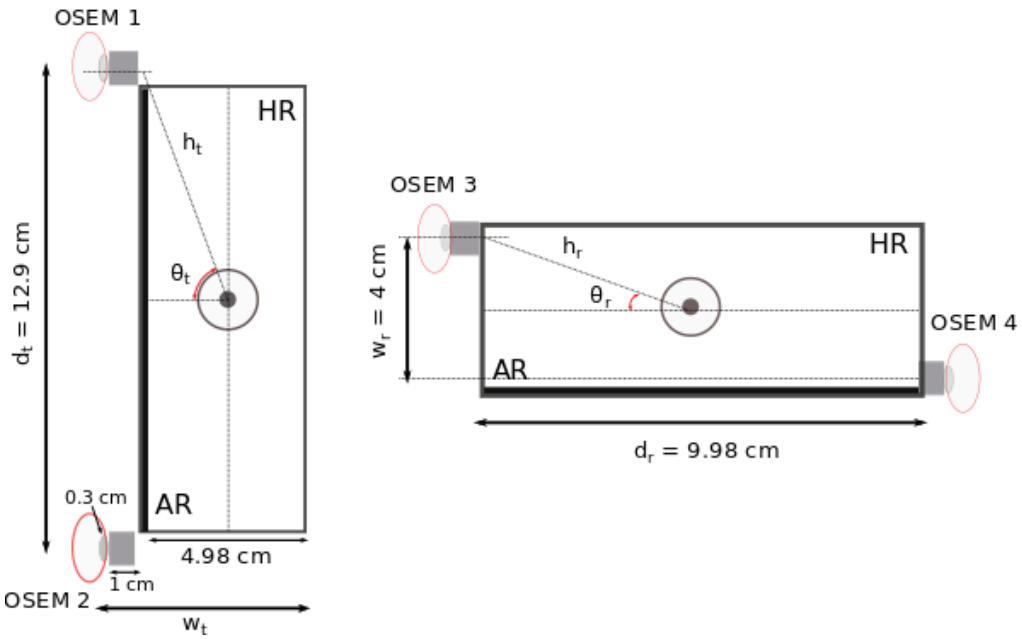

Figure 3.7: The matrices for basis change have been derived by using known dimensions of the BDO suspensions. The approximate length of the spacer between the optic and the magnet (0.3 cm) was measured to be 1 cm.

Based on fig. 3.7, the following estimations are obtained:

$$\theta_t = \tan^{-1}\left(\frac{2w_t}{d_t}\right) \tag{3.3}$$

$$\theta_r = \tan^{-1}(\frac{w_r}{d_r}) \tag{3.4}$$

$$h_t = \sqrt{(\frac{d_t}{2})^2 + (\frac{w_t}{2})^2} \tag{3.5}$$

$$h_r = \sqrt{(\frac{d_r}{2})^2 + (\frac{w_r}{2})^2} \tag{3.6}$$

The OSEM to Euler matrix transforms the forces through the OSEMs to displacement of the optic given by the following relation:

$$\begin{bmatrix} F_L \\ F_S \\ F_B \\ \tau_p \\ \tau_y \\ \tau_r \end{bmatrix} = [OSEMtoEuler] * \begin{bmatrix} F_1 \\ F_2 \\ F_3 \\ F_4 \end{bmatrix} \tag{3.7}$$

The OSEM to Euler matrix is of the form 4x6 and is given as:

$$\begin{pmatrix} 1 & 1 & 0 & 0 \\ 0 & 0 & -cos(\theta_r) & cos(\theta_r) \\ cos(\theta_t)sin(\theta_t) & -cos(\theta_t)sin(\theta_t) & 0 & 0 \\ 0 & 0 & h_r sin(\theta_r) & h_r sin(\theta_r) \\ h_t cos(\theta_t) & -h_t cos(\theta_t) & 0 & 0 \\ 0 & 0 & 0 & 0 \end{pmatrix}$$

In a similar way, the relation between the optic displacement and corresponding signals (Flag1,2,3,4) from the OSEM is:

$$\begin{bmatrix} Flag1 \\ Flag2 \\ Flag3 \\ Flag4 \end{bmatrix} = [EulertoOSEM] * \begin{bmatrix} F_L \\ F_S \\ F_B \\ \tau_p \\ \tau_y \\ \tau_r \end{bmatrix} \tag{3.8}$$

The Euler to OSEM matrix is a 6x4 matrix given as follows:

$$\begin{pmatrix} 1 & 0 & 0 & 0 & h_t cos(\theta_t) & 0 \\ 1 & 0 & 0 & 0 & -h_t cos(\theta_t) & 0 \\ 0 & -1 & 0 & h_r cos(\theta_r) & 0 & 0 \\ 0 & 1 & 0 & h_r cos(\theta_r) & 0 & 0 \end{pmatrix}$$

3.4 Modelling the optical plant with Finesse

For the modelling of the optical plant, all the components before the MSR (as shown in fig. 1.3) has been replaced with three triple suspensions. The rest remains the same. The optical plant consists of the actuator-to-sensor response which has been derived using Finesse and the script used for the modelling is given in Appendix F. Fig. 3.8 shows the architecture of the plant where the actuators and sensors (near and far field QPDs) are shown. The 1f sensor refers to the sensing of the MDWS alignment signals that is obtained by a double demodulation at f_{MI} and f_{OMC} whereas the 2f sensor is for spot position sensing at $2f_{MI}$ as described in chapter 2.

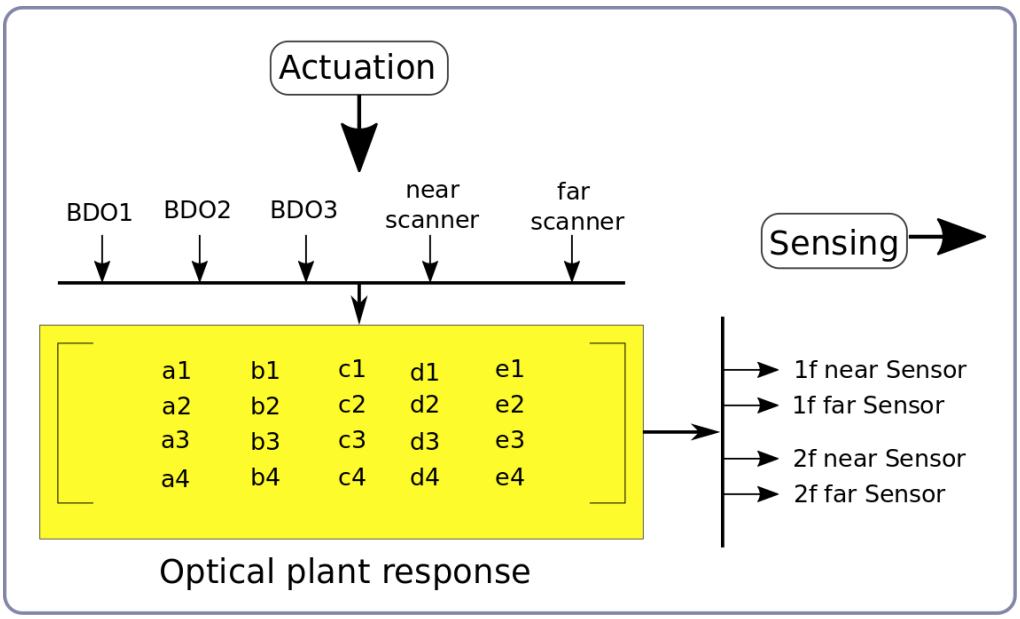

Figure 3.8: Schematic of the optical plant in which the elements of the matrix are derived using Finesse simulations.

3.4.1 The 1f optical response

The optical response of the 1f sensor is modelled by a DC optic rotation through a range of angles. The resulting QPD signal is double demodulated at f_{dither} and f_{MI} to give the resulting plots as shown in fig. 3.9. The slope of the traces gives the elements of the matrix for the 1f sensor as shown in fig. 3.8.

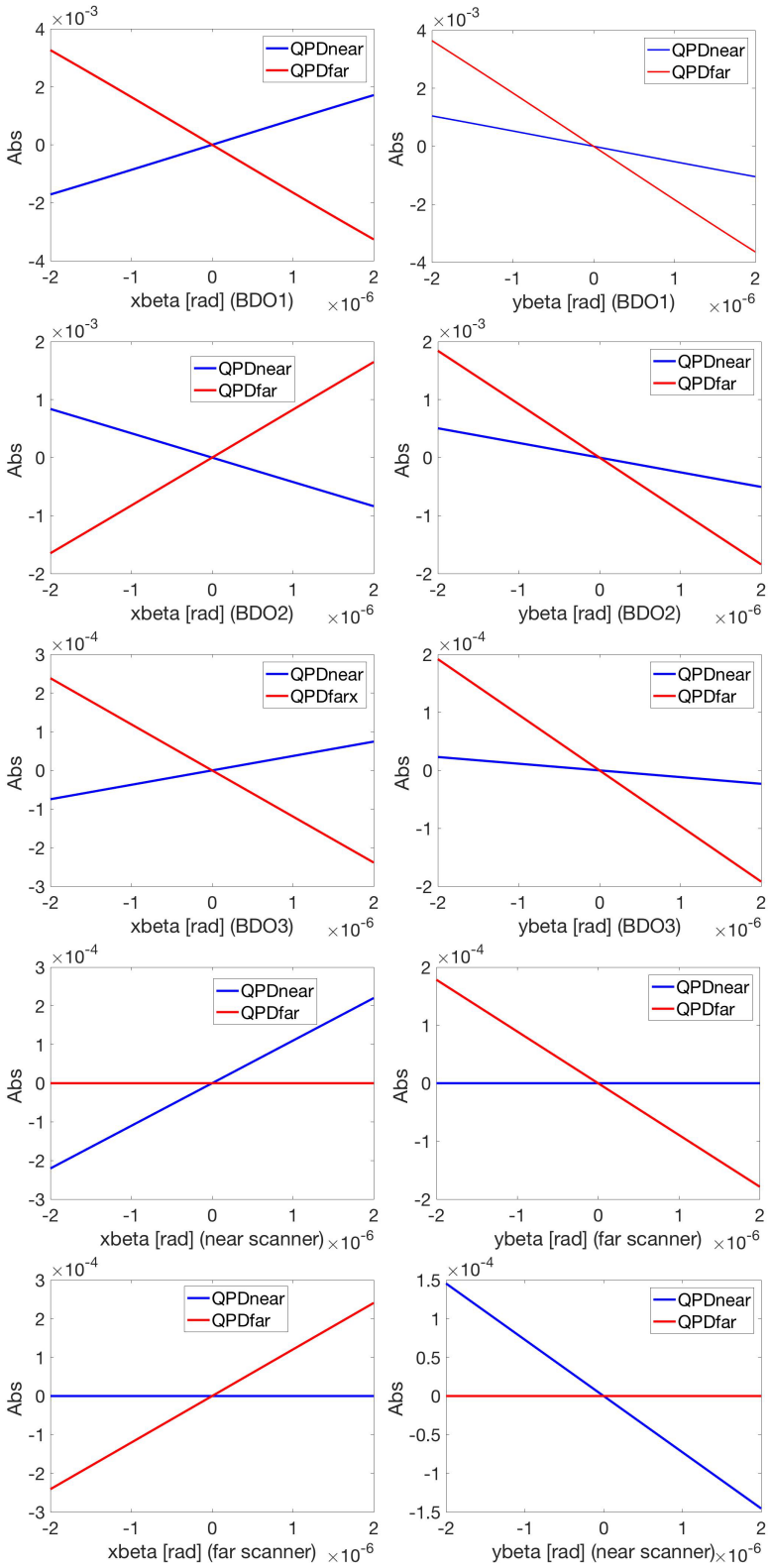

Figure 3.9: Finesse simulation for the optical plant transfer function measured at the near and far QPD. The actuators, from top to bottom: BDO1, BDO2, BDO3, the near scanner and the far scanner. The left hand figures are for rotation and the right hand figures are for tilt of the respective optic.

3.4.2 Modelling the 1f servo

The 1f servo is modelled to be in the sensor basis and consists of:

- An integrator at DC for providing high loop gain at lower frequencies
- A low pass filter with a cut off at 50 Hz
- Inverse of the suspension transfer function (suspension compensation filter)

The resultant shape of the servo is a product of the above three. The UGF of the loop can be adjusted with a separate loop gain factor. The integrator and the cut off frequency for the low pass filter have been designed to have a required UGF without adding noise at high frequencies.

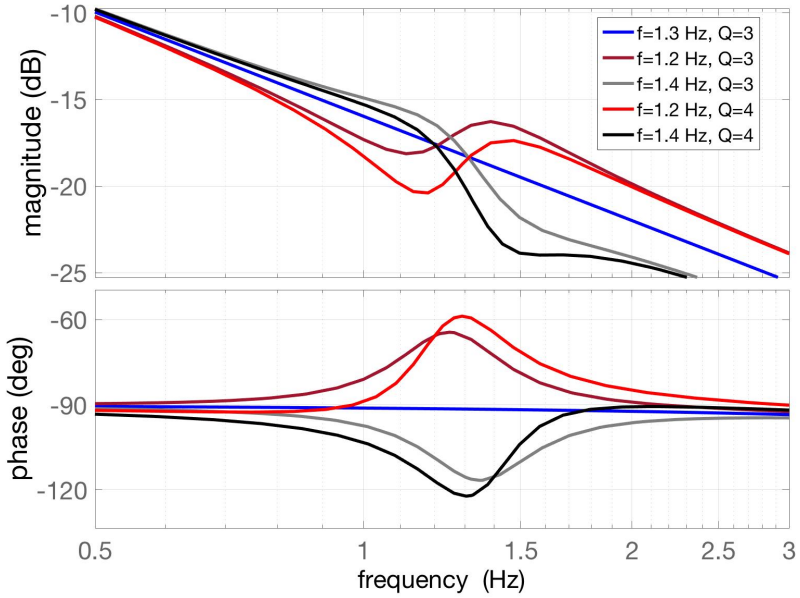

Figure 3.10: The resultant shape of the servo with different compensation filters as given by the legend.

It was found that that a small error in the frequency and Q of the suspension compensation filter can give rise to significant phase jumps. In fig. 3.10, the shape of the resultant servo is shown with different compensation filters for a suspension that is modelled as a second-order resonant low pass filter with a Q of 3 and a resonance frequency of 1.3 Hz. The

straight line is for the condition when the suspension transfer function is perfectly cancelled.

3.4.3 The 2f optical response

The optical response of the *2f sensor* is constructed in two steps by using the *beam detector* in Finesse which gives the beam profile of a laser beam at a given frequency. The beam detector is placed at the same location as that of the MDWS QPDs. In the first step, the actuator is given a DC rotation and as a result the beam spot at f_{MI} moves off the center of the detector which can be seen by the shifting of maxima from the center (x=0) in fig. 3.11. Second, the graph for the x position of the maxima vs angle of rotation of the actuator is plotted as shown in fig. 3.12. The slope of this curve represents the ability of an actuator to move the beam spot. Similar curves are obtained for all the actuators from which the the matrix elements for the 2f sensor as shown in fig. 3.8 is obtained.

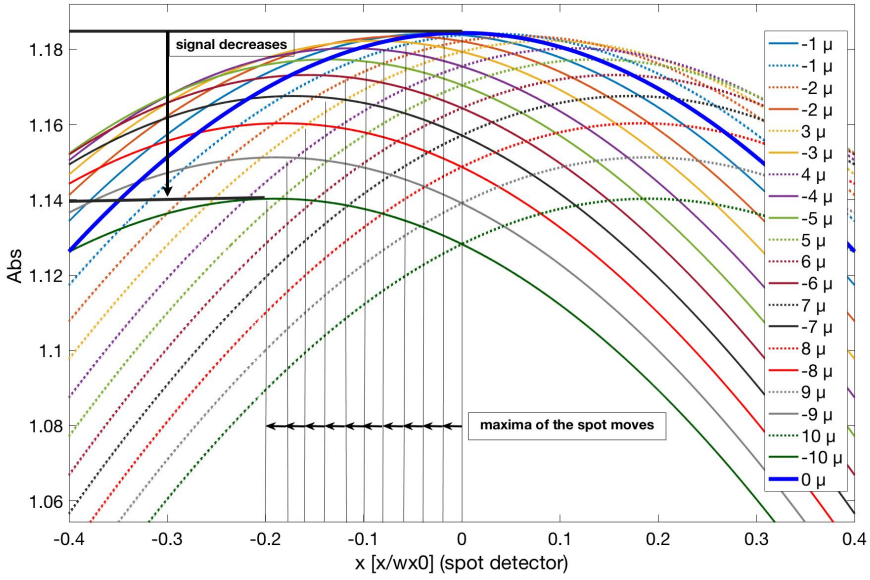

Figure 3.11: Output of the 2f beam detector vs BDO1 rotation where the legend indicates rotation in microns. The beam waist size (wx0) of 239μ is used as a scaling factor as shown on the x-axis. The overall strength of the signal decreases when the spot moves as shown by the decreasing arrow on the top left.

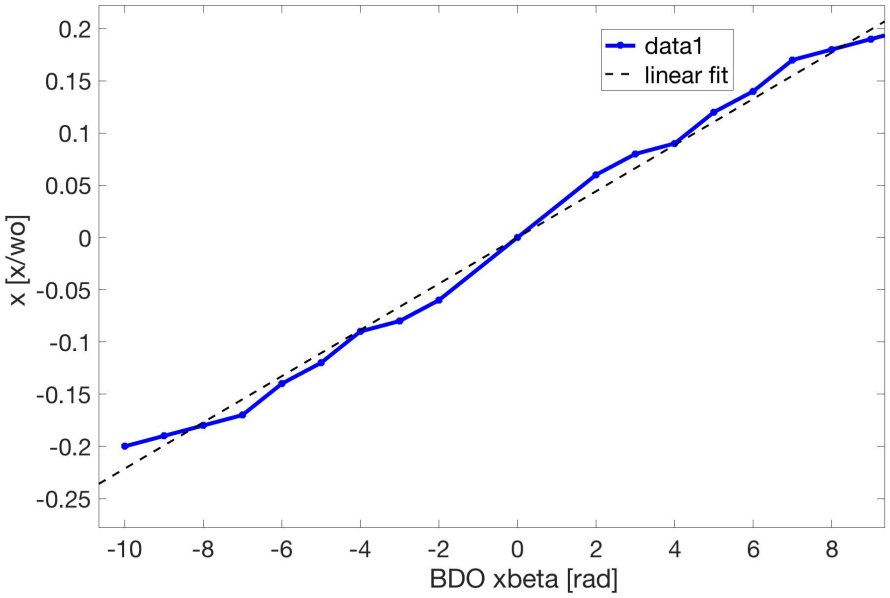

Figure 3.12: The x positions of the maxima of the beam spot at f_{MI} vs BDO rotation angle. The slope of the linear fit is the response of the 2f sensor to spot motion on the QPDs caused by BDO1.

3.4.4 Modelling the 2f servo

The spot centring loops utilise the 2f sensors and galvanometer scanners to re-center the spots on the QPDs as described in section 2.4.1. The scanners have been modelled as a second-order low pass filter (fig. 3.13) with a resonance at 400 Hz (the free rotation resonance around the scanners axis with mounted mirror is between 400 Hz and 600 Hz [73]). The 2f servo consists of:

- A low pass filter with a cut off at 500 Hz
- An integrator at DC
- Inverse of the scanner TF

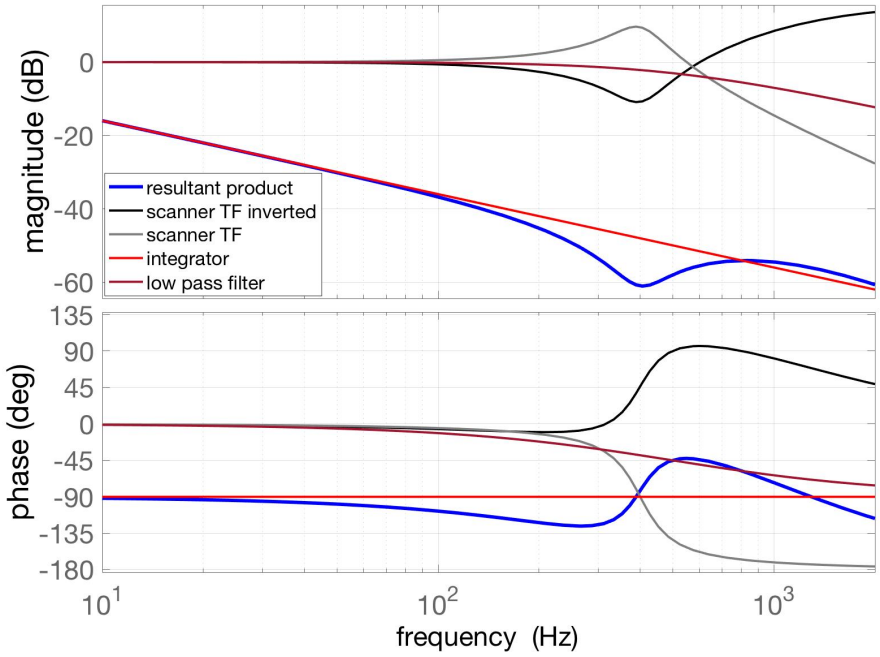

Figure 3.13: Design of the 2f servo shown by the product of the filter components in blue.

3.5 Measurement of noise

There are a few sources of noise associated with the MDWS system that were externally measured as described in this section. The measured data is prepared and imported into the model using Matlab and SimulinkNb. An example of how this is done is given in Appendix D, E.

3.5.1 Seismic noise

Seismic noise is one of the most prominent noise source that can couple in through the suspension point or through the clamped structure that holds the OSEMs as can be seen in fig. 2.19a and fig. 3.4. In both cases, the OSEM will *"see"* a displacement and create a proportional signal. If the magnet is positioned at the sweet spot, as explained in section 2.5.3, the seismic noise through the OSEM is negligible. The two pathways of seismic noise injection are shown in fig. 3.14. If there is a difference in loop gain

between the pair OSEM 1 and OSEM 2 or OSEM 3 and OSEM 4, of about 50% then the seismic noise injection through the OSEM is noticeable. The measurements of seismic noise were made at the GEO 600 site, and are given in Appendix C. The addition of seismic noise in the model is done through the SimulinkNb blocks as shown in fig. 3.4.

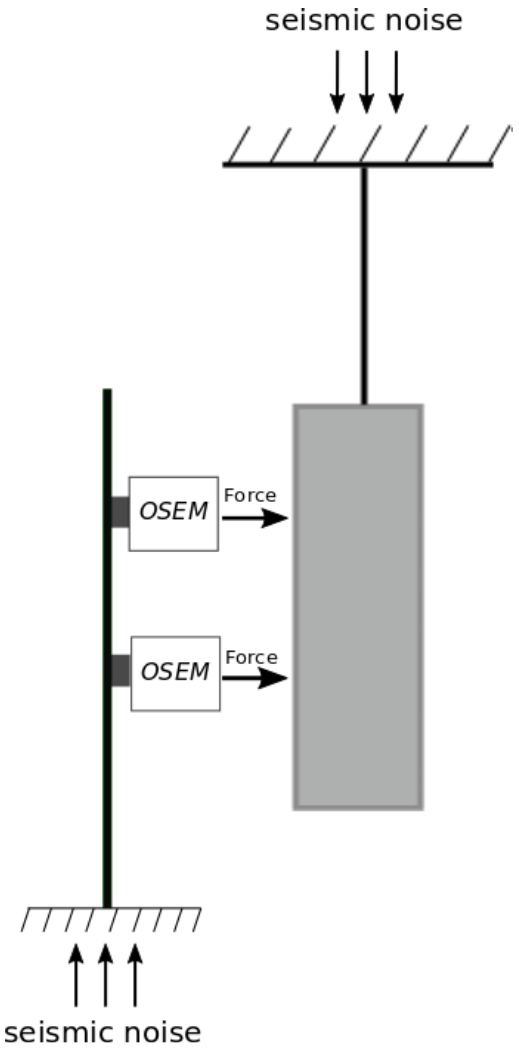

Figure 3.14: A simple representation of a single stage suspension and OSEM actuators to show the two paths of seismic injection.

3.5.2 LED Intensity noise

The intensity fluctuation of the OSEM LED was measured by replicating the transimpedance amplifier (TIA) circuit used at GEO 600 as shown in fig. 3.15a. The LED used is SFH485 that has a peak emission wavelength of 880 nm. To exclude the possibility of the current driver adding to the noise of the LED intensity fluctuation, a DC current supply was built as shown in fig. 3.15b. This noise source is added through the local control in the model as shown in fig. 3.4.

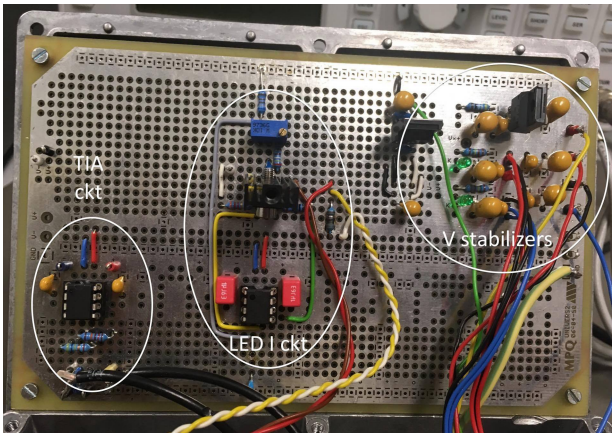

(a)

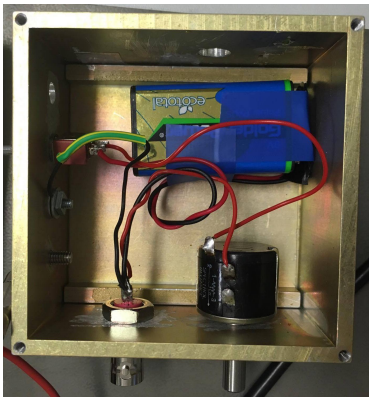

(b)

Figure 3.15: a). The transimpedance (2k Ω) circuit and the LED current driver circuit. b). The DC supply built using a battery source

The result of the measurement is shown in fig. 3.16 where the measured intensity noise is calibrated into units of displacement which is a more relevant unit for the OSEM which is a displacement sensor. For converting the output of the TIA in $\frac{V_{out}}{\sqrt{Hz}}$ to displacement units of $\frac{\mu m}{\sqrt{Hz}}$ the following relation is used:

$$\text{Displacement } (\frac{\mu m}{\sqrt{Hz}}) = \text{TIA output } (\frac{V_{out}}{\sqrt{Hz}}) * \frac{2.5\,mm}{7\,V} * 10^3 \tag{3.9}$$

where, the calibration factor of $\frac{2.5\,mm}{7\,V}$ is obtained from the OSEM sensitivity measurements from section 2.5.4.

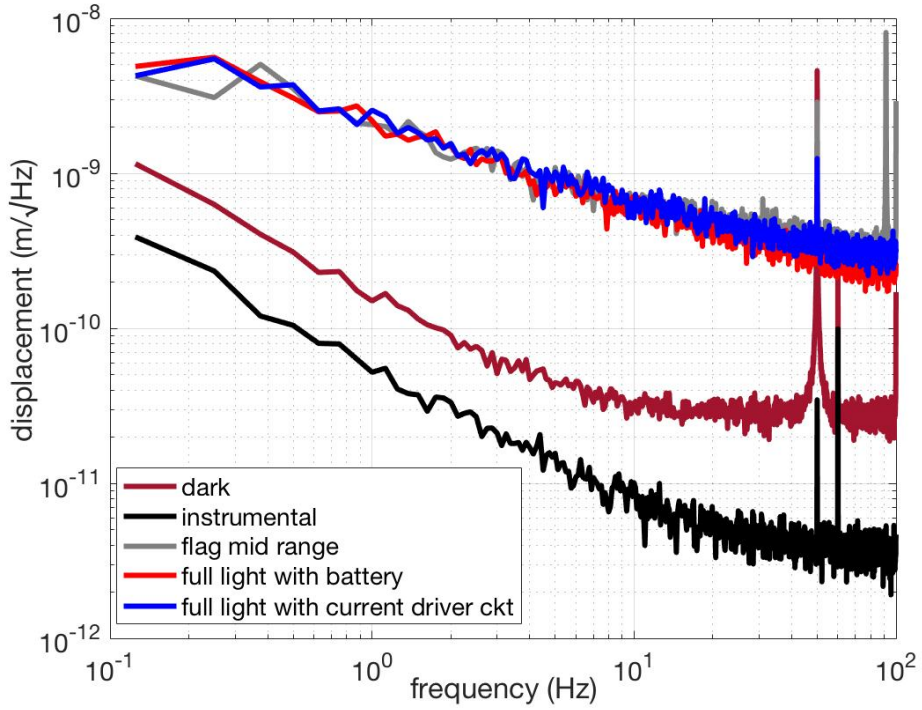

Figure 3.16: The LED displacement noise measurement.

The pink and the black traces in fig. 3.16 correspond to the measurement for the current driver circuit and the DC current supply for the LED when the flag is completely removed. As can be seen, they lie on top of each other indicating that the source of current does not add noise to the measurement. The grey curve is the measurement for the flag at mid-range. Each of the three curves is normalized with the total DC signal on the photodiode. The dark noise measurement shown in blue is about an order of magnitude lower at low frequencies and more than two orders at high frequencies than the top curves. The instrument (SR785 spectrum analyzer) noise is measured for completeness and is orders of magnitude below the displacement noise contribution of the OSEM LED.

3.5.3 OSEM coil driver noise

The circuit that provides the feedback current for the BDO OSEMs is called the coil driver. It sources current to the four OSEM coils. The measured inductance of the coil is about 72 mH at 120 Hz and a resistance of 270 Ω. The circuit design is given in Appendix F. The measurement of the current noise of the coil driver was made with an OSEM and three resistors to mimic the other three BDO OSEMs.

The measurement is given in fig. 3.17 and shows a current noise of about $4\,\mathrm{nA}/\sqrt{\mathrm{Hz}}$ at 1 Hz. The instrumental (SR785) noise is well below the current noise curve. This noise is added in the model as shown in fig. 3.4.

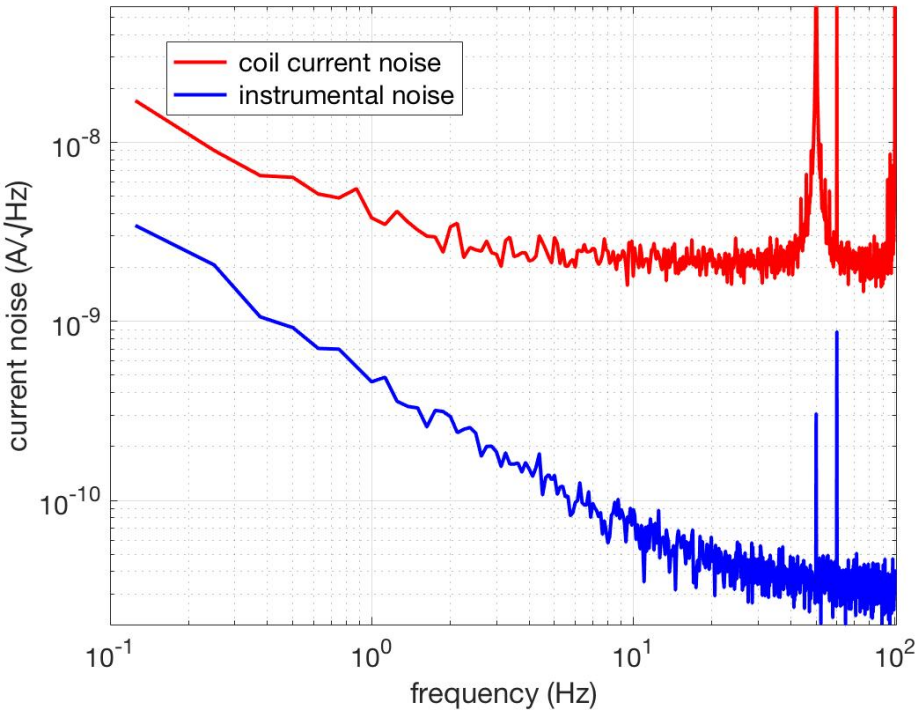

Figure 3.17: The measured current noise of the BDO coil driver.

3.6 Coupling between the 1f and 2f loops

For replicating the default operating state of the MDWS scheme, the alignment control loops (1f) and the spot centring loops (2f) were stabilised simultaneously in the model. The OLTFs of the four 1f loops is shown in fig. 3.18. It was observed that the 1f and the 2f loops interact with each other. This can be seen by the change in the shape of the OLTF of the 1f loops when the 2f loops are turned on and vice versa is true for the 2f loops also. This effect becomes more prominent if the 1f loop gains are further increased so the gains have been kept low to have a stable operating state. Also, gain hierarchy is maintained between the loops so that one loop is at a higher gain than the other for each DoF as was also done in section 2.7.3.

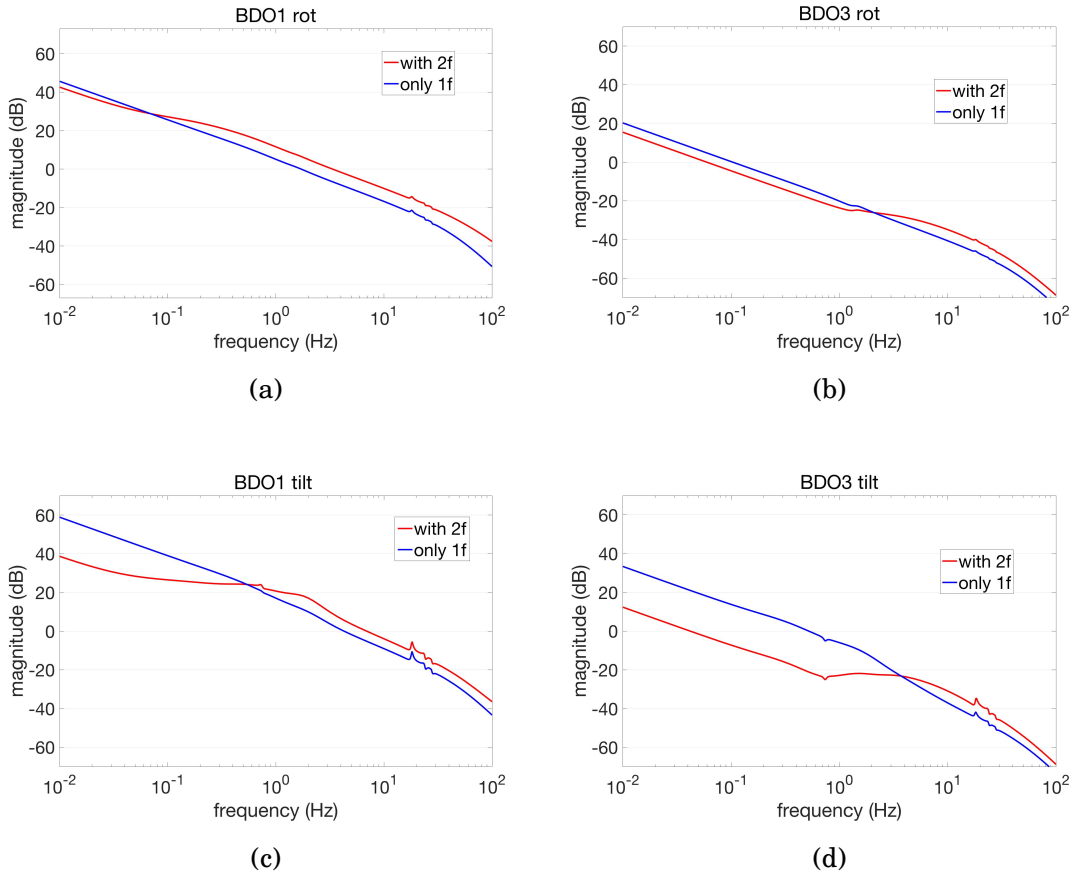

Figure 3.18: The OLTF of the MDWS 1f loops. The blue curve is only with the 1f loops working and the red curve is with the 2f loops having a UGF of 100 Hz. In both the cases the system was in a stable operating state.

3.7 Noise budget of the MDWS loops

In this section the results of the noise budget modelling is presented. The state of the system in which the following results are obtained is with the 1f and 2f loops working simultaneously as described in section 3.6.

3.7.1 The near QPD x error signal

The contribution of various noise sources in the model to the error signal can be seen in fig. 3.19. It can be seen that for frequencies lower than the BDO1 and BDO3 suspension resonance of 1.3 Hz, the dominant sources of noise are the seismic noise injection through the triple suspensions and the OSEM coil driver noise of BDO1 and BDO3. Above 1.3 Hz, the LED intensity noise of BDO1 dominates. The multiple noise peaks between 10 Hz to 20 Hz is due to the filters in the LC as can be seen in fig. 3.5. The 50 Hz peak is the line frequency and its higher harmonics.

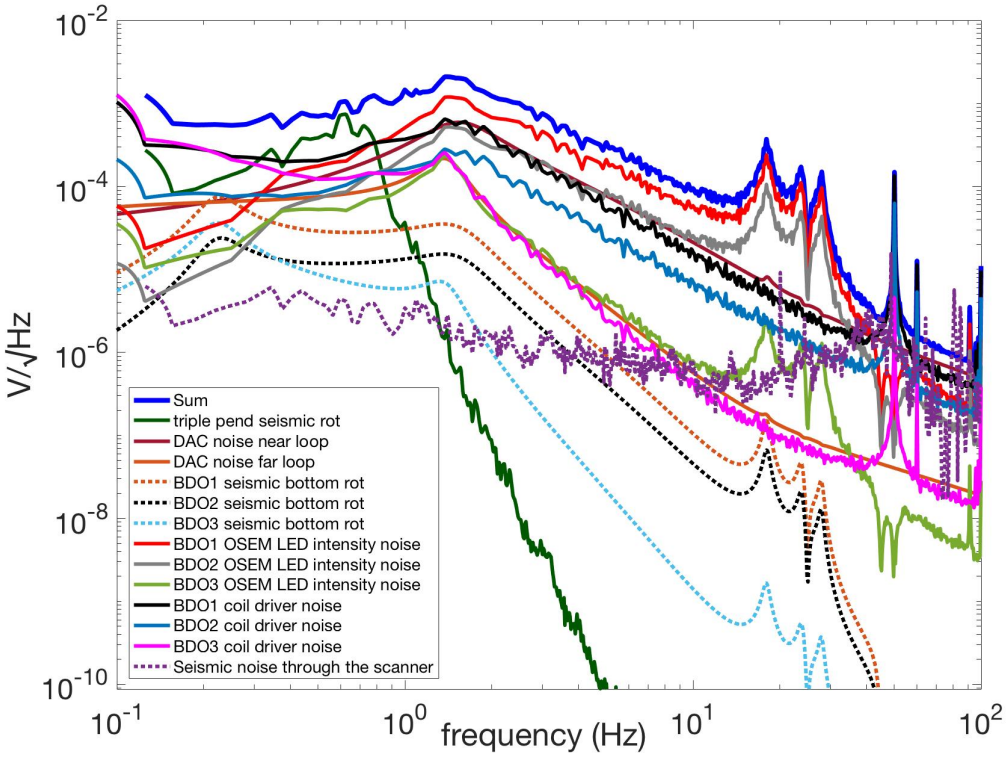

Figure 3.19: Noise budget of the error signal at the near QPD for misalignment in the x plane.

3.7.2 The far QPD x error signal

The noise budget of the far QPD x error signal as shown in fig. 3.20 has a similar noise contribution at all frequencies as that of the near x loop shown in fig. 3.19 but about a factor of five higher at the peak around 1.4 Hz. This is because of having lower UGF and hence lesser noise suppression. The dominant noise is the OSEM LED intensity noise through the BDO1 suspension.

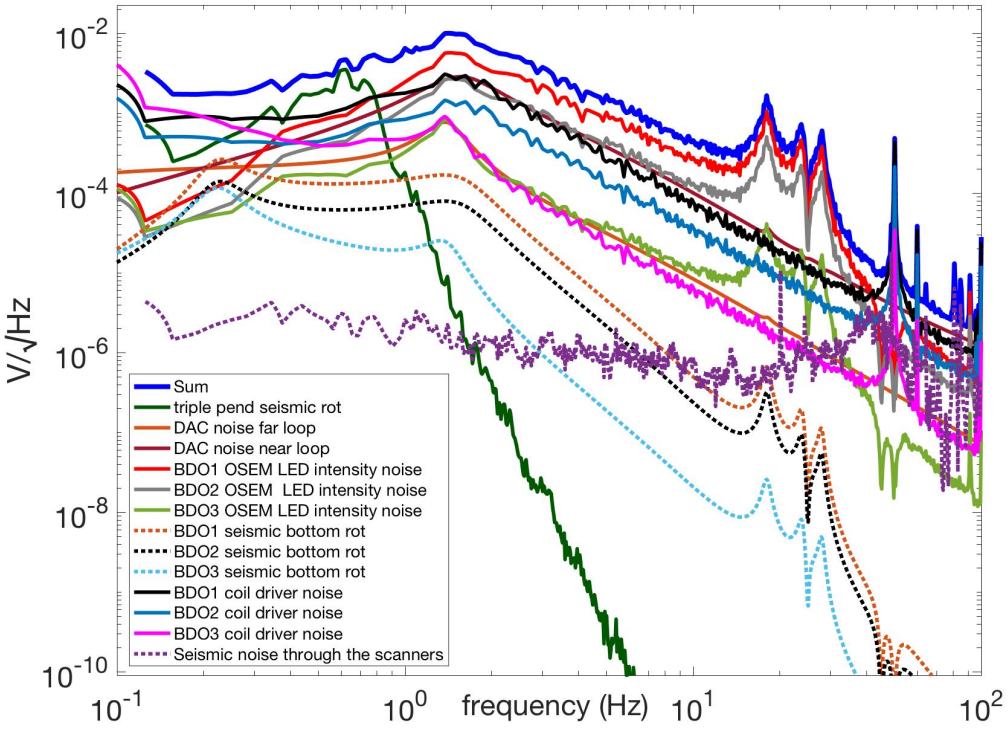

Figure 3.20: Noise budget of the error signal at the far QPD for misalignment in the x plane.

3.7.3 The near QPD y error signal

The noise budget of the near QPD y error signal is shown in fig. 3.21. The noise peak appears at about 0.75 Hz mainly due to the coupling of seismic noise through the longitudinal degree of the three BDO suspensions. As shown in fig. 3.1, the resonances of the BDO2 suspension are damped by the local control but not by the MDWS feedback loops so it contributes to more noise at 0.75 Hz than BDO1 and BDO3. Just above 1.3 Hz, the noise of the DAC dominates all other noise sources. It was found that if the suspension compensation filter is designed to be precise then the contribution of DAC noise can be reduced.

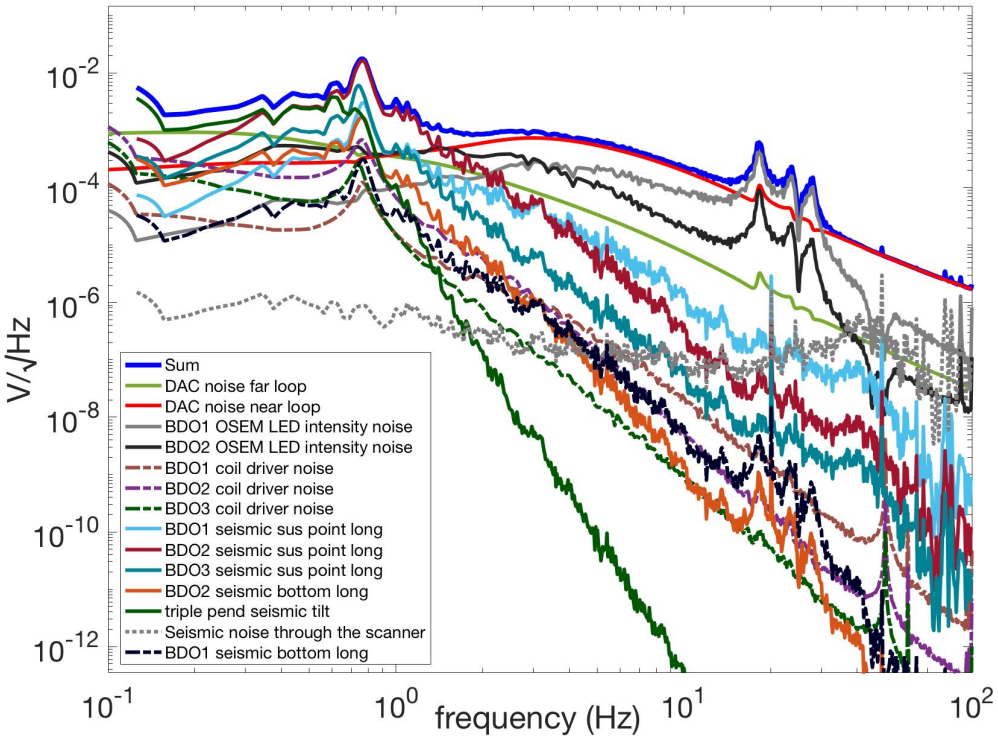

Figure 3.21: Noise budget of the error signal at the near QPD for misalignment in the y plane.

3.7.4 The far QPD y error signal

The noise budget for the far QPD y signal as shown in fig. 3.22 is quite similar to that for the near QPD error signal and is dominated by the seismic noise coupling through the longitudinal DoF of the BDO suspensions at about 0.75 Hz. On comparing the noise floor of the x and y error signals, the latter is about a factor of five higher. This is due to a strong noise coupling through the longitudinal degree which is not the case for the orthogonal x direction. Also, as shown in table 3.2, the tilt (0.6 Hz) and longitudinal (0.78Hz) resonance frequencies for BDO3 are close to each other so the coupling is further increased. Hence, the compensation filter has to be designed precisely else noise coupling through various sources increases.

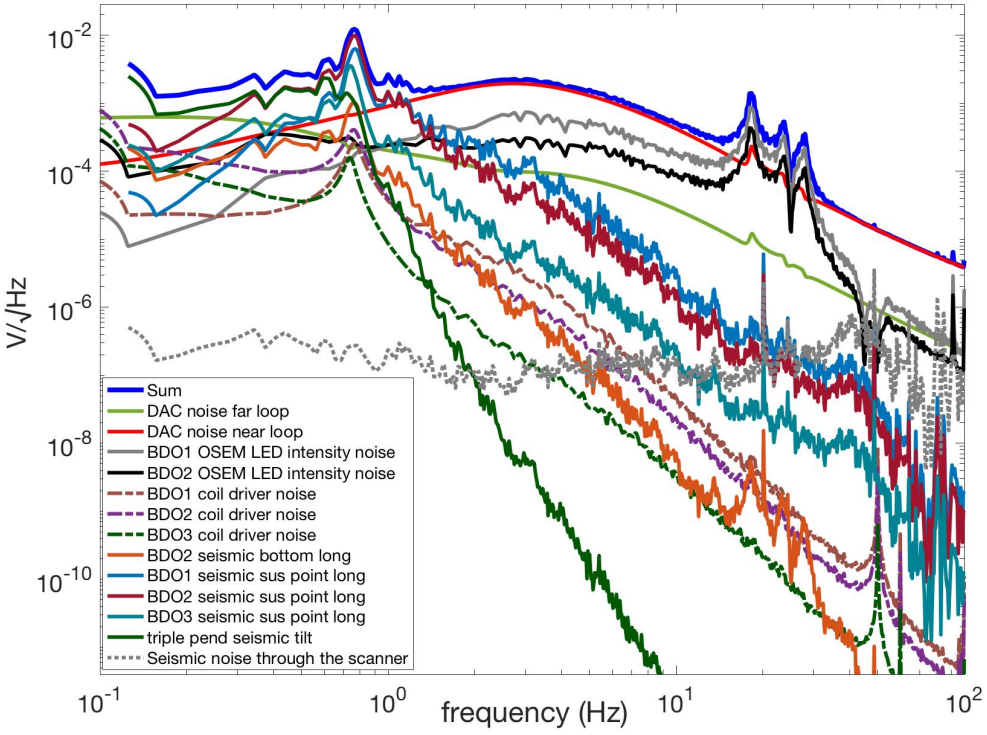

Figure 3.22: Noise budget of the error signal at the far QPD for misalignment in the y plane.

CHAPTER 4

Summary and outlook

This thesis presents the development of the MDWS AA scheme for the OMC at GEO 600. The motivation for this work is that the current AA scheme called the beacon dither can only achieve a bandwidth of about 20 mHz and is thus unable to suppress the motion of the IFO output beam that is dominated by the residual motion of the Michelson suspensions around 1 Hz. Moreover, the beacon dither scheme requires the addition of four injections done by dithering ('shaking') the BDO1 and BDO3 output optics that adds to the rms motion of the beam. This rms motion can lead to noise coupling into h and even poses an additional loss for squeezing. An improvement of these conditions is promised by the MDWS scheme that does not require additional modulations and has a higher control bandwidth of at least a few Hz.

A preliminary test of MDWS for one DoF given in section 2.7.1 was done before the work in this thesis. It was shown that with 3 Hz of bandwidth good error signal suppression can be achieved. Therefore, the goal of this work was to obtain at least 5 Hz of bandwidth for the four degrees of alignment and possibly replace the beacon dither scheme with it permanently.

Finally, as shown in section 2.7.3, stability was achieved for all four DOFs using a gain hierarchy with 2 Hz bandwidth for two degrees and lower bandwidth for the other two degrees. However, a few challenges were faced as described in section 2.8 that prevented the full time implementation of the MDWS AA scheme. To further consolidate our understanding, the system was modelled using simulation tools that gave a deeper insight into the various subparts of the real system. The experimental and modelling results obtained during this thesis will pave the way for the final goal of having a high-bandwidth AA scheme for the OMC at GEO 600.

The following is a summary of the investigation and the conclusions that can be made based on the work. Also, possible improvements are discussed:

- The 8° Gouy phase separation between BDO1 and BDO3 makes the actuators far from orthogonal. This means that the actuators have to move a lot to sufficiently span the alignment DoF space that causes excessive movement and possible coupling between them. It was seen through the modelling work that if the response of the actuators is not compensated well such that their frequency response is very different from one another then noise coupling to the control signal through various sources will be higher as shown in section 3.7.

  Also, transfer function measurements (given in section 2.20) revealed the resonance frequencies of the BDO1 and BDO3 tilt DoF are quite different. One of the possible reasons that can be explained by the model is that BDO3 is suspended 180° off in roll such that the centre of mass of the optic lies above the point of attachment of the pendulum wires (explained in section 3.2). However, this does not pose a problem in the implementation of the MDWS scheme if the compensation filters are well designed as will be needed for further work. Furthermore, if the BDO suspensions are relocated to ensure a better Gouy phase separation then coupling between the loops can be reduced a lot more. A picture of the suspensions inside the vacuum tank is shown in fig. 4.1.

- As shown in section 2.8, the MDWS error signals showed a DC drift over a day scale while operating in a low-bandwidth state. This requires more investigation as this is not clearly understood at the moment. Furthermore, a coupling between the MDWS alignment signals and the spot centring signals was found and this triggered a new design of the electronics which ensures better separation.

  Hence, new electronic modules were built to separate the paths of the two signals (shown in Appendix B). An investigation was carried out for possible ground loops in the GEO 600 cleanroom where the electronics is installed. Further improvements such as the grounding of the sending and receiving cables were made consistent. To further minimise the interaction between the loops, the 2f servo that

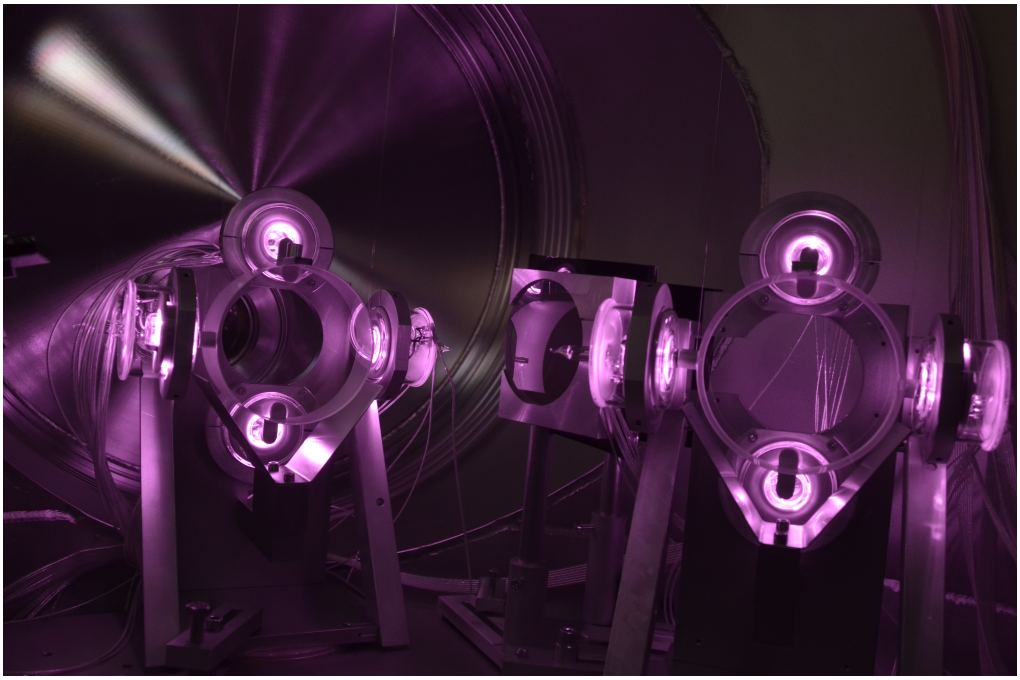

Figure 4.1: A picture of the BDO1 (right) and BDO3 (left) suspensions inside the TCOb vaccum tank taken with an IR filter, during one of the downtimes of the detector. The brightly lit OSEM LED emits light at 880 nm while the wavelength of the main laser is 1064 nm. Picture courtesy: Emil Schreiber.

currently exists as analog electronics will be migrated to CDS. The work for this has already begun. Also, in section 3.6 it was shown that there is an interaction between the 1f and 2f loops through the optical plant. This will be one of the foremost things to investigate in going ahead.

- Seismic noise is one of the biggest contributors of noise near suspension resonances. The seismic noise measurements done at the BDO vacuum tanks have been included in the model but the one from the OMC tank is not included yet as it requires further development of the model architecture. As shown in Appendix C.1.2 the OMC seismic isolation can be improved that will possibly reduce the noise coupling to the h channel and to the MDWS control signals.

Appendices

APPENDIX A

Fitting script for BDO TF measurement

The frequency dependent transfer function of a single stage pendulum can be approximated with a resonant low-pass filter having the following form,

$$H(s) = \frac{w_0^2}{s^2 + \frac{w_0}{Q}s + w_0^2} \tag{A.1}$$

where, H(s) is the complex transfer function
Q is the quality factor of the resonator
w_0 is the angular resonance frequency

Factorizing the denominator of A.1 gives,

$$H(s) = \frac{w_0^2}{[s + \frac{w_0}{2Q} + (\sqrt{\frac{1}{Q^2} - 4})\frac{w_0}{2}][s - \frac{w_0}{2Q} + (\sqrt{\frac{1}{Q^2} - 4})\frac{w_0}{2}]} \tag{A.2}$$

The poles of the system are obtained by equating the denominator of A.2 to zero, giving

$$p1 = -\frac{w_0}{2Q} + i\frac{w_0}{2}\sqrt{\frac{-1}{Q^2} + 4} \tag{A.3}$$

$$p2 = -\frac{w_0}{2Q} - i\frac{w_0}{2}\sqrt{\frac{-1}{Q^2} + 4} \tag{A.4}$$

Comparing eq A.2 and A.3 to a complex number notation, z= a+i b, gives

$$a = \frac{-w_0}{2Q} \tag{A.5}$$

$$b = \frac{w_0}{2Q}\sqrt{(2Q)^2 - 1} \tag{A.6}$$

On rearranging eq. A.5 and A.6 in terms of Q and f (f = $\frac{w_0}{2\pi}$) we get,

$$Q = \frac{1}{2}\sqrt{1+\frac{b}{a}^2} \tag{A.7}$$

$$f = \frac{-a}{2\pi}\sqrt{1+\frac{b}{a}^2} \tag{A.8}$$

The following Matlab script is a model of a resonant low pass filter, using eq. A.7 and A.8. The script also plots the data points obtained from the experiment. The best fit can be obtained by choosing the required number of zeros and poles. The result for the BDO TF measurements is shown in section 2.20.

```
% w, frequency in Hz
% mag, magnitude
% rad, phase measured in radians
deg=rad*180/pi; % deg, angle in degrees
omega=w*2*pi; % omega, angular frequency
% Model of a second order low pass filter
[b,a]=invfreqs(mag.*exp(1i*rad),omega,2,4); % 2 zeros
    and 4 poles
[zeros, poles, gain]=tf2zp(b,a);
poleQfact=(sqrt(1+(imag(poles)./real(poles)).^2))/2;
polefreq=((real(poles).*poleQfact)./pi)*(-1);
zeroQfact=(sqrt(1+(imag(zeros)./real(zeros)).^2))/2;
zerofreq = ((real(zeros).*zeroQfact)./pi)*(-1);
[h,f]=freqs(b,a,1000);
% Plot the magnitude curve
figure(1)
plot(f/2/pi,abs(h),'b',w,mag,'rx')
set(gca,'xscale','log')
set(gca,'yscale','log')
% Plot phase curve
figure(2)
plot(f/2/pi,angle(h)*180/pi,w,deg,'ro')
set(gca,'xscale','log')
```

APPENDIX B

Improved design of electronics for MDWS

The improved demodulation electronics was developed by Marc Brinkmann, Michael Weinert and the E-workshop at AEI. This was done to reduce cross talk between the 1f and 2f electronics. In this design, the signal lines from the QPD is split through an HF splitter module into the two demodulation paths as shown in fig. B.2. The connections from the different QPD quadrants is as shown in fig. B.1. In the old design, instead of the HF splitter there was a simple soldered joint to separate the two signal paths that caused coupling.

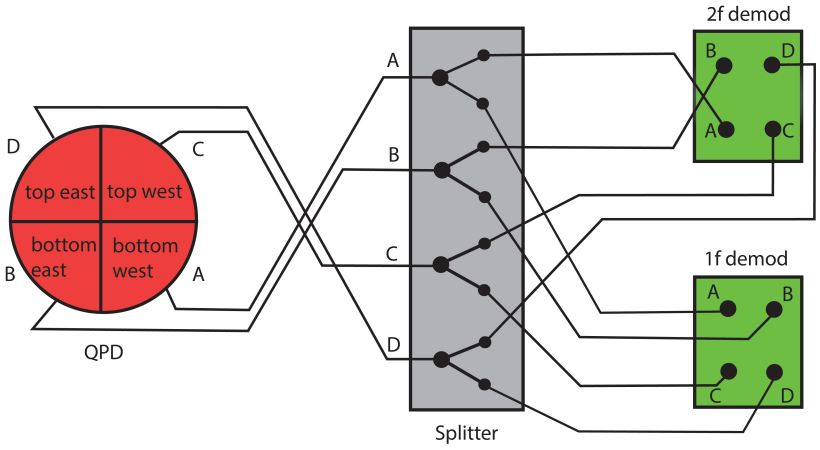

Figure B.1: QPD electrical connections

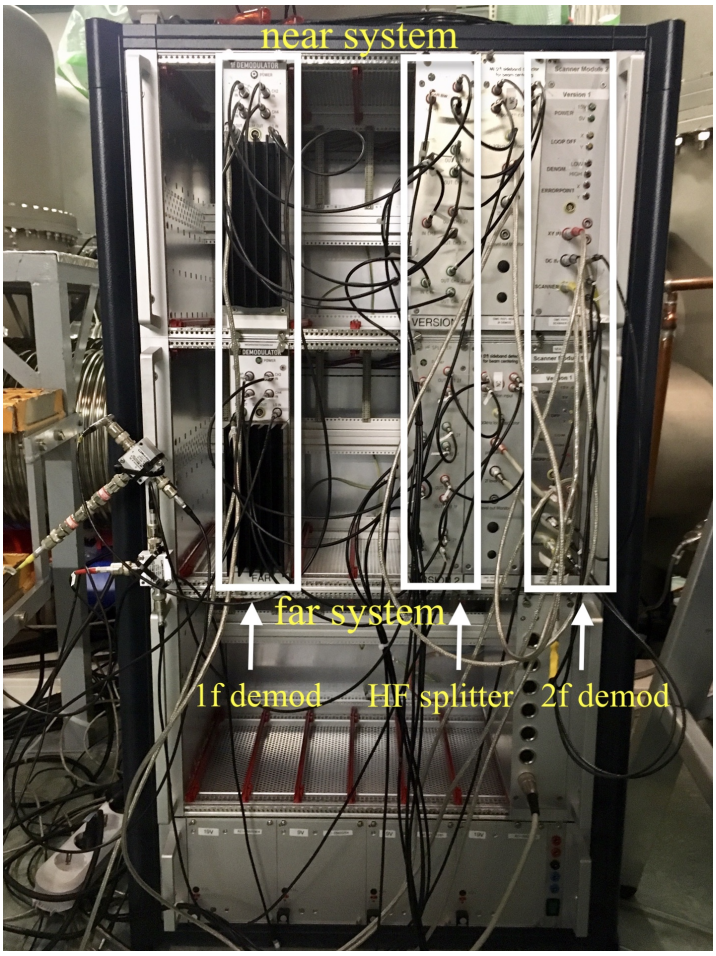

Figure B.2: The new electronic crate showing the demodulation electronics for the near (upper rack) and the far (lower rack) sensing paths.

APPENDIX C

Seismic noise measurements

The following document summarizes the seismic noise measurements made at the output of the detector as already mentioned in section 3.5. Fig. C.1 shows the output optics relevant for MDWS. The TCOa vacuum tank houses BDO2, TCOb tank houses BDO1 and BDO3 and TCOc houses the OMC. The noise measurements were done with two types of geophones - L-22 [88] and CDJ-Z2C [89]. These were calibrated against the STS2 seismometer in the 10 m prototype hall at AEI, which is a well calibrated instrument. Both the geophones have a natural resonance frequency of about 2 Hz. The L22 is used for the horizontal (X,Y) axes and the CDJ-Z2C is used for the vertical (Z) axis.

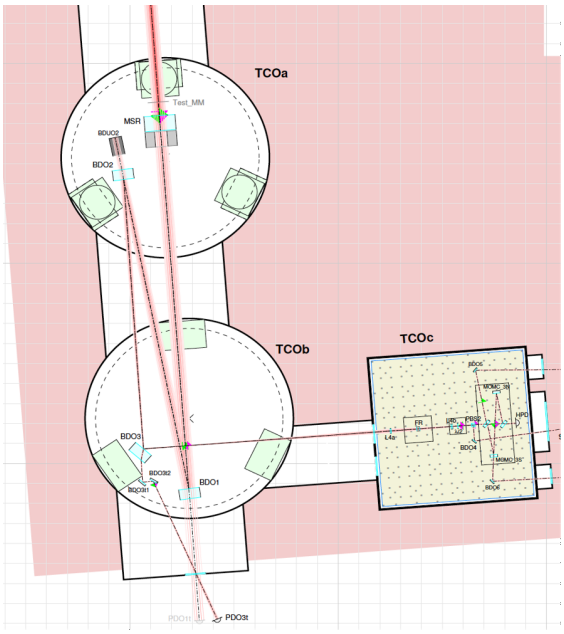

Figure C.1: Layout of the vacuum tanks at the detector output. The beam entering into the TCOa tank from top left is coming after passing through the IFO.

C.1 TCOc measurements

The TCOc tank comprises the OMC, HPD, mode matching lenses to the OMC and a Faraday assembly for squeezing injection. These components are mounted on top of an optical table that itself rests on a passive seismic isolation system consisting of three Minus-K seismic isolators. Details of the implementation of this system can found in [49].

C.1.1 The TCOc table top motion and the ground motion at GEO 600

Two measurements were made with the geophones kept on top of the optical bench and placed on the ground as shown in fig. C.2. The ground motion was measured to have a $\frac{1}{f^2}$ form above 1 Hz and unknown noise structures around 20 Hz that cause a bump. The lines around 20 Hz were also present in the BDO flag signals. The traces for the bench top measurement have a $\frac{1}{f^4}$ form above 1 Hz.

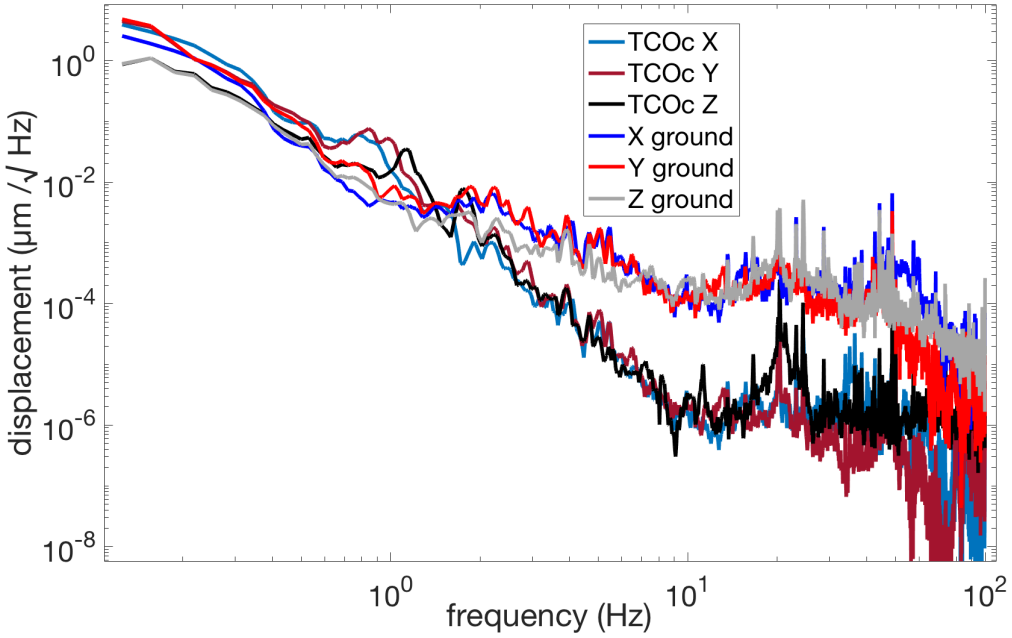

Figure C.2: Seismic noise measurements made on top of the TCOc optical bench and made on the ground.

C.1.2 The transmissibility of the seismic isolation system

The transmissibility of the Minus-K seismic vibration system is shown in fig. C.3. It is obtained by taking a transfer function between the in-vacumm and ground measurements as shown in fig. C.2. As can be seen the resonance frequency of the system lies more towards 1 Hz than 0.5 Hz as claimed by the manufacturer [90]. This means that the residual seismic motion of the OMC can be as source of noise for the MDWS alignment signals as well as for the detector's h channel.

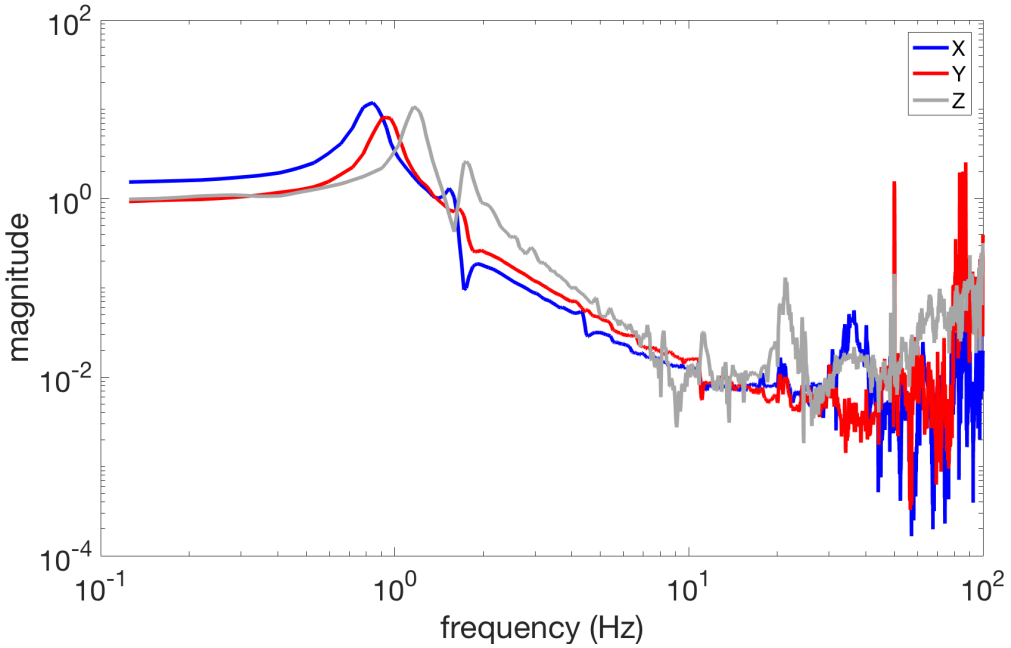

Figure C.3: The measurement of transmissibility of the minus-K isolation system showing resonance peaks for the three DOFs.

C.2 TCOa measurements

The BDO2 suspension that is located inside the TCOa tank has additional fluorubber pads beneath its baseplate. This was done as part of the upgrade of BDO suspensions for extra isolation under the GEO-HF program [49]. Therefore two seismic measurements were done in the tank one on top of the optical bench and another on top of the BDO2 baseplate.

C.2.1 Measurement on top of the optical table

The measurement for the table top motion is shown in fig. C.4 where the traces have a slope of slightly less than $\frac{1}{f^2}$ above 1 Hz. These measurements were made in air.

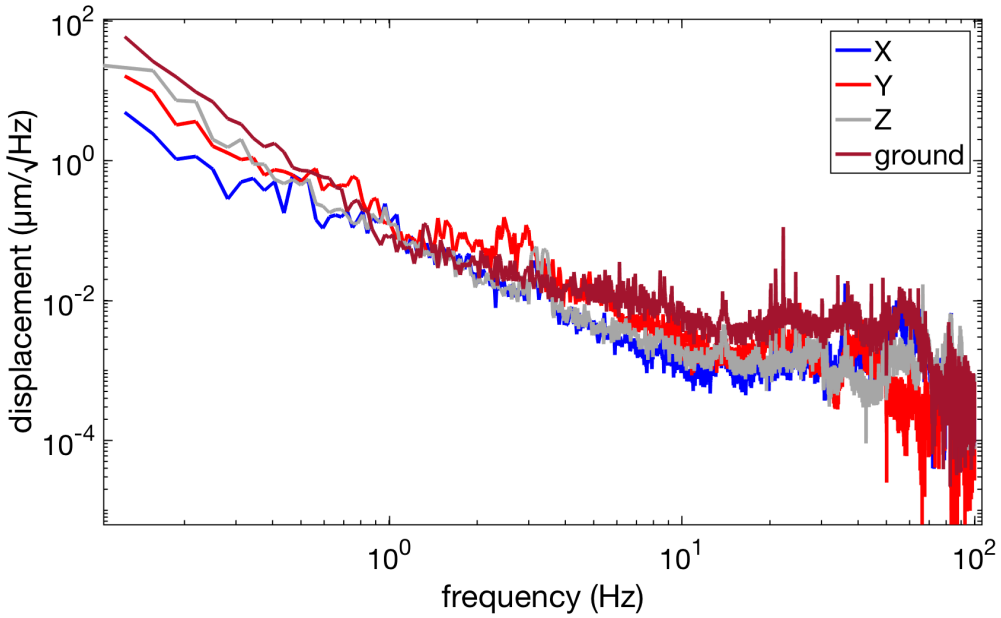

Figure C.4: Seismic measurements on top of the TCOa optical bench.

C.2.2 Measurement on top of the BDO2 baseplate

The measurement on top of the baseplate is shown in fig. C.5 where the 3.5 Hz resonance peak is probably the resonance of the baseplate. The additional seismic isolation provided by the rubber pads is not clearly visible in comparison to fig. C.4.

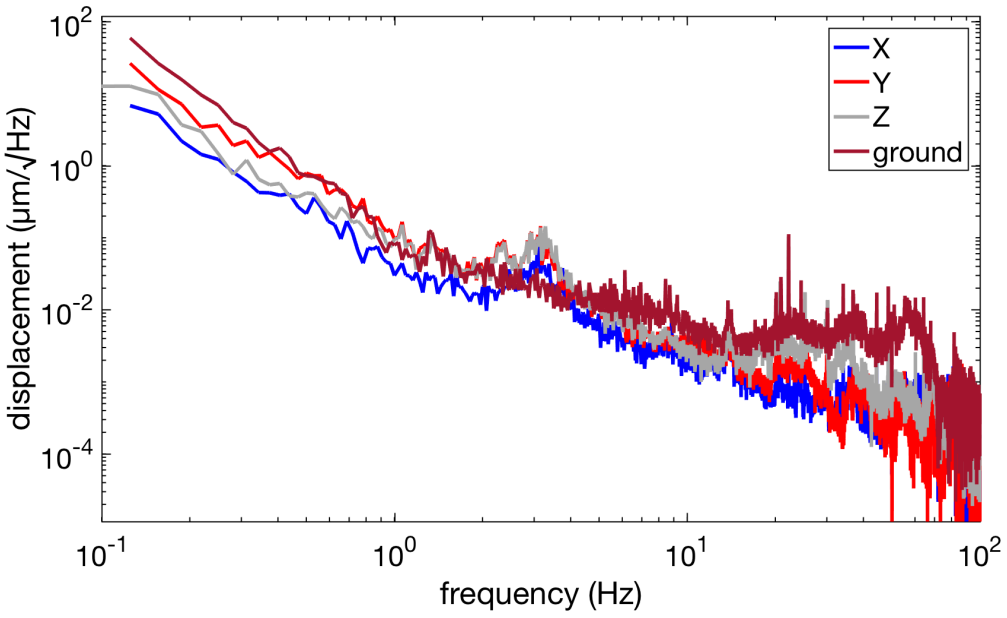

Figure C.5: Seismic noise measurement on top of the BDO2 baseplate.

C.3 TCOb measurements

The seismic noise measurement made inside the TCOb tank in-air is shown in fig. C.6. The slope of the traces can be roughly estimated to be below $\frac{1}{f^2}$ above 1 Hz.

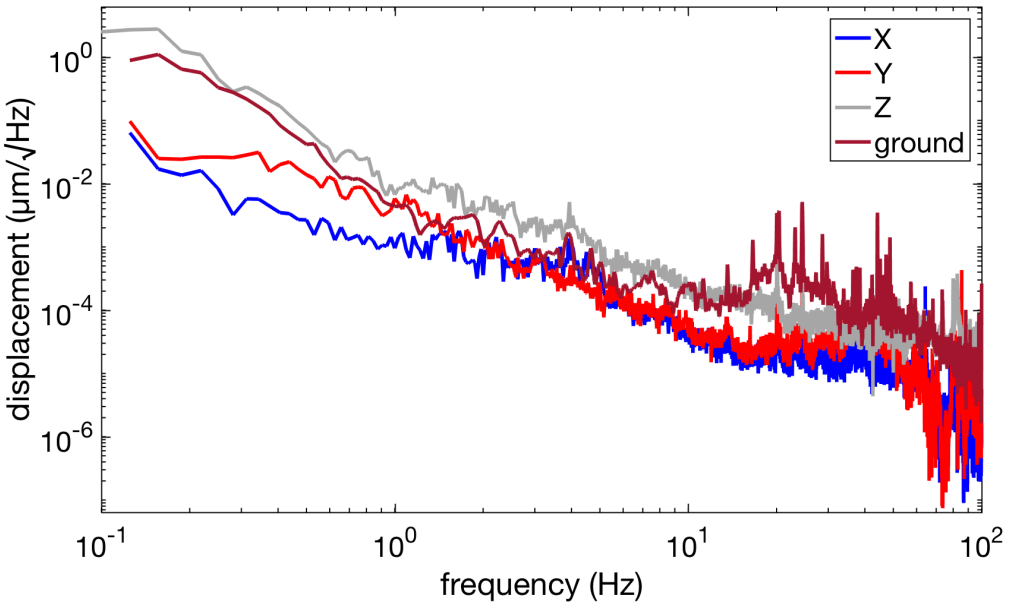

Figure C.6: Seismic measurements on top of the TCOb optical bench.

APPENDIX D

A basic introduction to the SimulinkNb tool

The following document is about the SimulinkNb tool which is a noise budget simulation tool developed by Chris Wipf [91]. It is accessible with the LIGO credentials and can be downloaded from [92]. To begin with, a stable control system has to be built where the noise inputs can then be measurements or intuitive guesses. A simple control loop is taken as an example here to explain the working of the tool.

D.1 Why is a noise budget important?

Short version: it helps us to hunt down the noise present in our system.
We can project various noise sources through the model to the quantity of interest. These noise sources maybe measured or maybe based on analytic understanding of the system. SimulinkNb is a handy tool that can be used to make noise budgets for simple and complex systems in a very easy way.

D.2 How does it work?

- The first step is to build a robust control model using Simulink. Different coloured blocks can be used for the various components such as the sensors, transducers, actuators, gain knobs etc with the correct units of the quantity it represents.

- The second step is to gather all the information about the system such as measurements of TF for example. As a quick start if measurements are not available then generic expressions can be used to construct model components. For eg., the TF of a single stage sus-

pension can be designed as a second order resonant low pass filter using a simple script in Matlab and called into the respective block in the model.

- The third step is to use SimulinkNb blocks for injecting noise. As many blocks as needed can be used along with a cal and sink block as shown in fig. D.1.

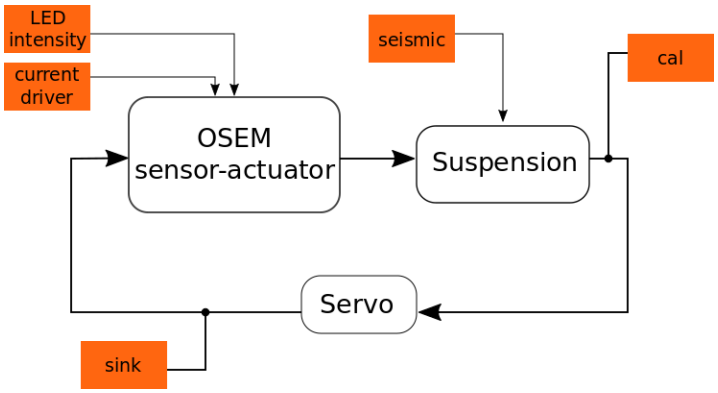

Figure D.1: Using SimulinkNb noise blocks in a control model

The following steps are being copied directly from the 'README.md'file which gets downloaded automatically with the SimulinkNb toolkit. These steps are for graphically configuring a noise budget for the Simulink model.

1. Open SimulinkNb/NbLibrary.mdl and copy in a NbNoiseSink block. Connect it in series with the signal that you actually measure (for example, digitized photodetector output). Double-click the block to give a name to the DoF you are measuring (a string).
2. Copy in a NbNoiseCal block. Sum it in to the signal that you "want" to measure and budget the noise of (for example, test mass displacement calibrated in meters). Double-click the block and set the DoF name (which must correspond with the Sink block) and the unit string (for example, 'displacement [m/rtHz] ').
3. Copy in one or more NbNoiseSource blocks. Sum them in throughout the model wherever noise couples. Double-click each block and set the ASD of the noise source (which can be a constant or a vector). If desired, set one or more group strings, to name the noise source and/or form sub-budgets.
4. Use the nbFromSimulink function to obtain the individual noise

terms and calibration TFs.
5. Use the nbGroupNoises function to organize the noise terms into a hierarchical noise budget (NoiseModel object).
6. Plot the noise budget using a function such as matlabNoisePlot or fragNoisePlot

D.3 How to build a Noise Budget

The ASD of measured data (done for LED intensity noise) can be prepared using the following code in Matlab where data is stored in an excel file. Also the script generates a noise budget plot as shown in fig. D.2.

```
load('filename.xls'); % excel data file
LEDfreq = freq; % frequency data column
LEDasd = asd; % ASD data column
ASDnoiseLED = interp1(LEDfreq,LEDasd,frequency,'
    linear','extrap'); % using interp1 to interpolate
     the measured data to the frequency band of
    interest.
LEDnoise = ASDnoiseLED; % The noise block can now be
     simply named as LEDnoise

[A,B,C,D] = linmod('model_name');  % name of the
    control model without .slx extension
lcsys = ss(A,B,C,D); % state-space of the model
mdl = 'model_name';
dof = 'DOF';
[noises, sys] = nbFromSimulink(mdl,freq,'dof', dof);
nb = nbGroupNoise(mdl,noises,sys);
matlabNoisePlot(nb);
```

The noise budget with three contributing noise sources is shown in fig. D.2 where the quantity plotted is residual optic motion as shown by the *cal block* in fig. D.1.

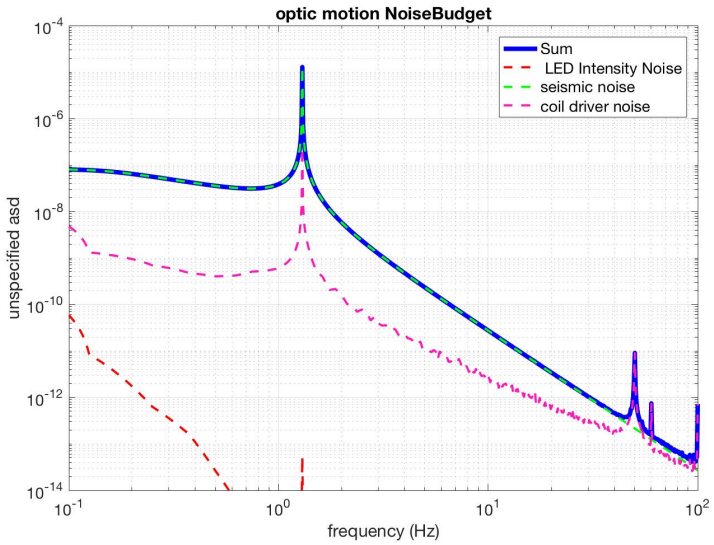

Figure D.2: Noise budget for the control model

APPENDIX E

Using SimulinkNb integrated with Finesse to generate noise budgets

The following document is about how to use Finesse (frequency domain tool) and SimulinkNb to generate noise budgets using a two mirror cavity system as an example. The basic steps are as follows:

1. Build the Finesse model and obtain the .out file.
2. Create complex TFs and a frequency response data (frd) object out of step 1 and save it in the Matlab workspace.
3. Separately create a SimulinkNb model by invoking Optickle (frequency domain tool) to auto generate a block. This can be hand edited to point to the Finesse output.
4. Call SimulinkNb to generate the noise budget.

E.1 Building a Fabry-Perot cavity model using Finesse

Fig. E.1 shows the setup of a Fabry-Perot cavity where the longitudinal control signal is obtained using the PDH technique. The Finesse model for this setup has been taken from the Finesse manual [80]. The procedure is to "shake" the mirrors m1 and m2 with a modulation and then demodulate the P_{ref} and P_{trans} detector signal at the modulation frequency. The output of the Finesse model is the magnitude and phase of the demodulated signal that can be converted into a complex form. Finally, the frd object can be created with a single line of Matlab code as shown below.

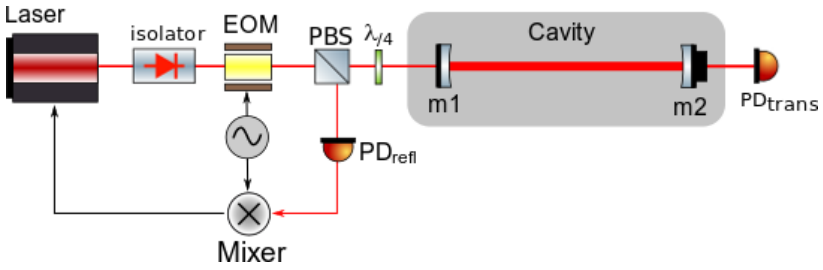

Figure E.1: Schematic of a Fabry-Perot with a PDH control scheme. The photodiode in transmission is added just for generating some extra TFs.

```
% Demodulated optical response of the ref and trans pd
    to actuation on m1
S1 = load ('PDHm1.out');
freq = S1(:,1);
m1_pdref_mag = S1(:,2);
m1_pdref_phase = S1(:,3);
m1_pdtrans_mag = S1(:,4);
m1_pdtrans_phase = S1(:,5);
% Demodulated optical response of the ref and trans pd
    to actuation on m2
S1 = load ('PDHm2.out');
freq = S2(:,1);
m2_pdfreq_mag = S2(:,2);
m2_pdref_phase = S2(:,3);
m2_pdtrans_mag = S2(:,4);
m2_pdtrans_phase = S2(:,5);
% Create complex notation
TF11 = m1_pdfreq_mag.*exp(m1_pdfreq_phase*i);
TF21 = m1_pdtrans_mag.*exp(m1_pdtrans_phase*i);
TF12 = m2_pdfreq_mag.*exp(m2_pdfreq_phase*i);
TF22 = m2_pdtrans_mag.*exp(m2_pdtrans_phase*i);
% Create FRD objects
H = zeros(2,2,length(freq));
H(1,1,:) = TF11;
H(1,2,:) = TF12;
H(2,1,:) = TF21;
H(2,2,:) = TF22;
finesseFRD = frd(H,freq,'Units','Hz');
```

E.2 Building a Simulink model

After the frd has been built it can be imported into a Simulink model that makes use of the Finesse output with the following command in Matlab:

```
driveArray = {'{m1}','{m2}'};
probeArray = {'{Pref}','{Ptrans}'};
buildOptickleSys('{CavityTest}','{freq}',driveArray,
    probeArray);
```

This generates the block as shown on the left in fig. E.2 where the block on the right is the layer beneath it. It has noise input blocks for the P_{ref} and P_{trans} signals. The label name below the block as marked by the red circle is *flexTF:optickleFrd(Cavity Test,freq)*. For getting the frd data from Finesse into this model the label name has to be replaced with *flexTF:finesseFrd*.

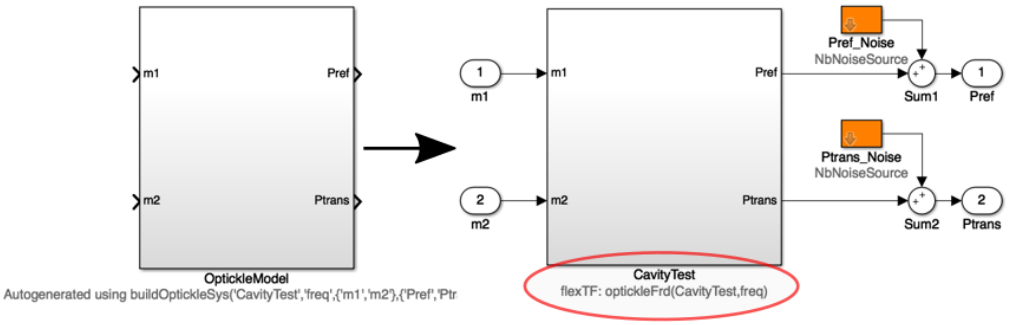

Figure E.2: Simulink model with noise inputs

It is possible to add more noise sources as one likes. For that simply copy the orange block and point to to another noise input. Additionally, a *cal* and *sink* block have to be added as given in Appendix D. The noise budget plot can be made with a similar script as in section D.3.

APPENDIX F

State-space model for the BDOs

The Mathematica modelling for the BDO suspensions is done by Dr. Mark Barton and can be cloned from here [83]. It includes the extra twist potential terms that arise due to the twisting of the cantilever blades which is an addition to a simple single stage suspension model that he worked on earlier. Once the 'FourWireTwistBlades' repository is downloaded it has the directory structure as shown by fig. F.1.

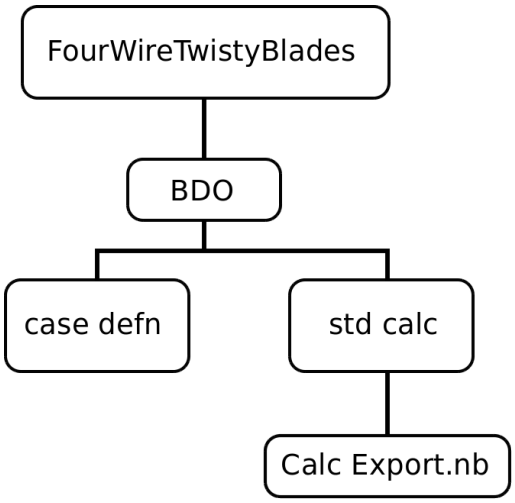

Figure F.1: Model directory structure

To define a user specific case with new input parameters make changes to the case defn (case definition) file and then save it. In the CalcExport.nb file make precomputed = false, then re evaluate it. A file with .m (Matlab extension) is generated in the same folder that has the ABCD matrices for the model.

F.1 For BDO1

$$1A = \begin{bmatrix} 0 & 0 & 0 & 0 & 0 & 0 & 1 & 0 & 0 & 0 & 0 & 0 \\ 0 & 0 & 0 & 0 & 0 & 0 & 0 & 1 & 0 & 0 & 0 & 0 \\ 0 & 0 & 0 & 0 & 0 & 0 & 0 & 0 & 1 & 0 & 0 & 0 \\ 0 & 0 & 0 & 0 & 0 & 0 & 0 & 0 & 0 & 1 & 0 & 0 \\ 0 & 0 & 0 & 0 & 0 & 0 & 0 & 0 & 0 & 0 & 1 & 0 \\ 0 & 0 & 0 & 0 & 0 & 0 & 0 & 0 & 0 & 0 & 0 & 1 \\ -22.81912 & 0 & 0 & 0 & 0.08957 & 0 & 0 & 0 & 0 & 0 & 0 & 0 \\ 0 & -21.44091 & 0 & 0 & 0 & 0.00128 & 0 & 0 & 0 & 0 & 0 & 0 \\ 0 & 0 & -578.77357 & 0 & 0 & 2.79627e-13 & 0 & 0 & 0 & 0 & 0 & 0 \\ 0 & 0 & 0 & -73.20701 & 0 & 0 & 0 & 0 & 0 & 0 & 0 & 0 \\ 111.92026 & 0 & 0 & 0 & -80.47243 & 0 & 0 & 0 & 0 & 0 & 0 & 0 \\ 0 & 1.06575 & 2.32925e-10 & 0 & 0 & -1240.42276 & 0 & 0 & 0 & 0 & 0 & 0 \end{bmatrix} \tag{F.1}$$

$$1B = \begin{bmatrix} 0 & 0 & 0 & 0 & 0 & 0 & 1 & 0 & 0 & 0 & 0 & 0 \\ 0 & 0 & 0 & 0 & 0 & 0 & 0 & 0 & 0 & 0 & 0 & 0 \\ 0 & 0 & 0 & 0 & 0 & 0 & 0 & 0 & 0 & 0 & 0 & 0 \\ 0 & 0 & 0 & 0 & 0 & 0 & 0 & 0 & 0 & 0 & 0 & 0 \\ 0 & 0 & 0 & 0 & 0 & 0 & 0 & 0 & 0 & 0 & 0 & 0 \\ 0 & 0 & 0 & 0 & 0 & 0 & 0 & 0 & 0 & 0 & 0 & 0 \\ 22.81912 & 0 & 0 & 0 & -0.84447 & 0 & 1.22981 & 0 & 0 & 0 & 0 & 0 \\ 0 & 21.44091 & 0 & 0 & 0 & 0.11553 & 0 & 1.22981 & 0 & 0 & 0 & 0 \\ 0 & 0 & 578.77357 & 0 & 0 & 0 & 0 & 0 & 1.22981 & 0 & 0 & 0 \\ 0 & 0 & 0 & 73.20701 & 0 & 0 & 0 & 0 & 0 & 1536.62644 & 0 & 0 \\ -111.92025 & 0 & 0 & 0 & 132.28977 & 0 & 0 & 0 & 0 & 0 & 1536.62643 & 0 \\ 0 & -1.06575 & -2.32925e-10 & 0 & 0 & 1239.92935 & 0 & 0 & 0 & 0 & 0 & 1024.41762 \end{bmatrix} \tag{F.2}$$

$$1C = \begin{bmatrix} 1 & 0 & 0 & 0 & 0 & 0 & 0 & 0 & 0 & 0 & 0 & 0 \\ 0 & 1 & 0 & 0 & 0 & 0 & 0 & 0 & 0 & 0 & 0 & 0 \\ 0 & 0 & 1 & 0 & 0 & 0 & 0 & 0 & 0 & 0 & 0 & 0 \\ 0 & 0 & 0 & 1 & 0 & 0 & 0 & 0 & 0 & 0 & 0 & 0 \\ 0 & 0 & 0 & 0 & 1 & 0 & 0 & 0 & 0 & 0 & 0 & 0 \\ 0 & 0 & 0 & 0 & 0 & 1 & 0 & 0 & 0 & 0 & 0 & 0 \\ 0 & 0 & 0 & 0 & 0 & 0 & 1 & 0 & 0 & 0 & 0 & 0 \\ 0 & 0 & 0 & 0 & 0 & 0 & 0 & 1 & 0 & 0 & 0 & 0 \\ 0 & 0 & 0 & 0 & 0 & 0 & 0 & 0 & 1 & 0 & 0 & 0 \\ 0 & 0 & 0 & 0 & 0 & 0 & 0 & 0 & 0 & 1 & 0 & 0 \\ 0 & 0 & 0 & 0 & 0 & 0 & 0 & 0 & 0 & 0 & 1 & 0 \\ 0 & 0 & 0 & 0 & 0 & 0 & 0 & 0 & 0 & 0 & 0 & 1 \end{bmatrix} \tag{F.3}$$

$$1D = \begin{bmatrix} 0 & 0 & 0 & 0 & 0 & 0 & 0 & 0 & 0 & 0 & 0 & 0 \\ 0 & 0 & 0 & 0 & 0 & 0 & 0 & 0 & 0 & 0 & 0 & 0 \\ 0 & 0 & 0 & 0 & 0 & 0 & 0 & 0 & 0 & 0 & 0 & 0 \\ 0 & 0 & 0 & 0 & 0 & 0 & 0 & 0 & 0 & 0 & 0 & 0 \\ 0 & 0 & 0 & 0 & 0 & 0 & 0 & 0 & 0 & 0 & 0 & 0 \\ 0 & 0 & 0 & 0 & 0 & 0 & 0 & 0 & 0 & 0 & 0 & 0 \\ 0 & 0 & 0 & 0 & 0 & 0 & 0 & 0 & 0 & 0 & 0 & 0 \\ 0 & 0 & 0 & 0 & 0 & 0 & 0 & 0 & 0 & 0 & 0 & 0 \\ 0 & 0 & 0 & 0 & 0 & 0 & 0 & 0 & 0 & 0 & 0 & 0 \\ 0 & 0 & 0 & 0 & 0 & 0 & 0 & 0 & 0 & 0 & 0 & 0 \\ 0 & 0 & 0 & 0 & 0 & 0 & 0 & 0 & 0 & 0 & 0 & 0 \\ 0 & 0 & 0 & 0 & 0 & 0 & 0 & 0 & 0 & 0 & 0 & 0 \end{bmatrix} \tag{F.4}$$

F.2 For BDO3

$$3A = \begin{bmatrix} 0 & 0 & 0 & 0 & 0 & 0 & 1 & 0 & 0 & 0 & 0 & 0 \\ 0 & 0 & 0 & 0 & 0 & 0 & 0 & 1 & 0 & 0 & 0 & 0 \\ 0 & 0 & 0 & 0 & 0 & 0 & 0 & 0 & 1 & 0 & 0 & 0 \\ 0 & 0 & 0 & 0 & 0 & 0 & 0 & 0 & 0 & 1 & 0 & 0 \\ 0 & 0 & 0 & 0 & 0 & 0 & 0 & 0 & 0 & 0 & 1 & 0 \\ 0 & 0 & 0 & 0 & 0 & 0 & 0 & 0 & 0 & 0 & 0 & 1 \\ -21.43267 & 0 & 0 & 0 & 0.10312 & 0 & 0 & 0 & 0 & 0 & 0 & 0 \\ 0 & -21.44029 & 0 & 0 & 0 & -0.19168 & 0 & 0 & 0 & 0 & 0 & 0 \\ 0 & 0 & -578.77424 & 0 & 0 & 0 & 0 & 0 & 0 & 0 & 0 & 0 \\ 0 & 0 & 0 & -68.88530 & 0 & 0 & 0 & 0 & 0 & 0 & 0 & 0 \\ 128.84928 & 0 & 0 & 0 & -20.41272 & 0 & 0 & 0 & 0 & 0 & 0 & 0 \\ 0 & -159.66869 & 0 & 0 & 0 & -1168.30762 & 0 & 0 & 0 & 0 & 0 & 0 \end{bmatrix} \tag{F.5}$$

$$3B = \begin{bmatrix} 0 & 0 & 0 & 0 & 0 & 0 & 1 & 0 & 0 & 0 & 0 & 0 \\ 0 & 0 & 0 & 0 & 0 & 0 & 0 & 0 & 0 & 0 & 0 & 0 \\ 0 & 0 & 0 & 0 & 0 & 0 & 0 & 0 & 0 & 0 & 0 & 0 \\ 0 & 0 & 0 & 0 & 0 & 0 & 0 & 0 & 0 & 0 & 0 & 0 \\ 0 & 0 & 0 & 0 & 0 & 0 & 0 & 0 & 0 & 0 & 0 & 0 \\ 0 & 0 & 0 & 0 & 0 & 0 & 0 & 0 & 0 & 0 & 0 & 0 \\ 21.43267 & 0 & 0 & 0 & -0.02351 & 0 & 1.22981 & 0 & 0 & 0 & 0 & 0 \\ 0 & 21.44029 & 0 & 0 & 0 & 0.11553 & 0 & 1.22981 & 0 & 0 & 0 & 0 \\ 0 & 0 & 578.77425 & 0 & 0 & 1.39813e-13 & 0 & 0 & 1.22981 & 0 & 0 & 0 \\ 0 & 0 & 0 & 68.88530 & 0 & 0 & 0 & 0 & 0 & 1536.62643 & 0 & 0 \\ -128.84928 & 0 & 0 & 0 & 78.91002 & 0 & 0 & 0 & 0 & 0 & 1536.62643 & 0 \\ 0 & 159.66869 & 0 & 0 & 0 & 1240.79689 & 0 & 0 & 0 & 0 & 0 & 1024.41762 \end{bmatrix} \tag{F.6}$$

$$3C = \begin{bmatrix} 1 & 0 & 0 & 0 & 0 & 0 & 0 & 0 & 0 & 0 & 0 & 0 \\ 0 & 1 & 0 & 0 & 0 & 0 & 0 & 0 & 0 & 0 & 0 & 0 \\ 0 & 0 & 1 & 0 & 0 & 0 & 0 & 0 & 0 & 0 & 0 & 0 \\ 0 & 0 & 0 & 1 & 0 & 0 & 0 & 0 & 0 & 0 & 0 & 0 \\ 0 & 0 & 0 & 0 & 1 & 0 & 0 & 0 & 0 & 0 & 0 & 0 \\ 0 & 0 & 0 & 0 & 0 & 1 & 0 & 0 & 0 & 0 & 0 & 0 \\ 0 & 0 & 0 & 0 & 0 & 0 & 1 & 0 & 0 & 0 & 0 & 0 \\ 0 & 0 & 0 & 0 & 0 & 0 & 0 & 1 & 0 & 0 & 0 & 0 \\ 0 & 0 & 0 & 0 & 0 & 0 & 0 & 0 & 1 & 0 & 0 & 0 \\ 0 & 0 & 0 & 0 & 0 & 0 & 0 & 0 & 0 & 1 & 0 & 0 \\ 0 & 0 & 0 & 0 & 0 & 0 & 0 & 0 & 0 & 0 & 1 & 0 \\ 0 & 0 & 0 & 0 & 0 & 0 & 0 & 0 & 0 & 0 & 0 & 1 \end{bmatrix} \tag{F.7}$$

$$3D = \begin{bmatrix} 0 & 0 & 0 & 0 & 0 & 0 & 0 & 0 & 0 & 0 & 0 & 0 \\ 0 & 0 & 0 & 0 & 0 & 0 & 0 & 0 & 0 & 0 & 0 & 0 \\ 0 & 0 & 0 & 0 & 0 & 0 & 0 & 0 & 0 & 0 & 0 & 0 \\ 0 & 0 & 0 & 0 & 0 & 0 & 0 & 0 & 0 & 0 & 0 & 0 \\ 0 & 0 & 0 & 0 & 0 & 0 & 0 & 0 & 0 & 0 & 0 & 0 \\ 0 & 0 & 0 & 0 & 0 & 0 & 0 & 0 & 0 & 0 & 0 & 0 \\ 0 & 0 & 0 & 0 & 0 & 0 & 0 & 0 & 0 & 0 & 0 & 0 \\ 0 & 0 & 0 & 0 & 0 & 0 & 0 & 0 & 0 & 0 & 0 & 0 \\ 0 & 0 & 0 & 0 & 0 & 0 & 0 & 0 & 0 & 0 & 0 & 0 \\ 0 & 0 & 0 & 0 & 0 & 0 & 0 & 0 & 0 & 0 & 0 & 0 \\ 0 & 0 & 0 & 0 & 0 & 0 & 0 & 0 & 0 & 0 & 0 & 0 \\ 0 & 0 & 0 & 0 & 0 & 0 & 0 & 0 & 0 & 0 & 0 & 0 \end{bmatrix} \tag{F.8}$$

The suspensions can now be defined by a single line of Matlab code:

susBDO1 = ss (1A,1B,1C,1D)
susBDO3 = ss (3A,3B,3C,3D)

APPENDIX G

Finesse script for the MDWS optical plant

```
# based on the Finesse model geoHF_official.kat

bs bs1 0.5 0.5 0 45 n11 dump n13 n14
l l1 0.02 0 0 n11 # carrier
l l2 0.004 $fMI 0 n14 # MI SB upper
s spacer 0 1 n13 n21 # 1064n space length changed to 0
bs bs2 0.5 0.5 0 45 n21 dump n23 n24
l l3 0 -$fMI 180 n24 # MI SB lower
s space2 0 1 n23 n25

bs triplepend1 1 0 0 45 n25 n26 dump dump
s space3 1 n26 n27
bs triplepend2 1 0 0 45 n27 n28 dump dump
s space4 1 n28 n29
bs triplepend3 1 0 0 45 n29 n30 dump dump
s space5 1 n30 n31
m MSR 0 1 0 n31 n32

gauss carrier l1 n11 9.9597519m -251.73734m 9.9810679m 51.73734m
gauss upperSB l2 n14  9.9597519m -251.73734m 9.9810679m 51.73734m
gauss lowerSB l3 n24 9.9597519m -251.73734m 9.9810679m 51.73734m

s sout1 1.79606 n32 nBDO1i

#### output optics telescope ####

bs BDO1 990E-3 10E-3 0 3.55 nBDO1o nBDO1i dump dump # T=1%
attr BDO1 Rc $BDO1_RofC

s sout2 1.5774 nBDO1o nBDO2i
bs BDO2 998.E-3 2.E-3 0 3.701 nBDO2i nBDO2o dump dump

s sout3 1.3501 1. nBDO2o nBDO3i
bs BDO3 998.E-3 2.E-3 0 44.896 nBDO3i nBDO3o dump dump

s rs14 1.11 1 nBDO3o nWTCOce1a # Distance BDO3 -> Window east
m sf14a 0 998.E-3 0 nWTCOce1a nWTCOce1b
s rs14e 0.005 1.45 nWTCOce1b nWTCOce1c
m sf14b 0 998.E-3 0 nWTCOce1c nWTCOce1d

# Add a lens L4a
s rs14w 0.075 1 nWTCOce1d nTCOcL1a
lens l_L4a $F_L4a_fl nTCOcL1a nTCOcL1b

s rsl4a 0.025 nTCOcL1b nTCOcPBS1a # Distance L4a -> PBS1

m sf15a 0 990.E-3 0 nTCOcPBS1a nTCOcPBS1b
```

```
s rsPB1 0.017 1.45 nTCOcPBS1b nTCOcPBS1c
m sf15b 0 995.E-3 0 nTCOcPBS1c nTCOcPBS1d

s rsPBS1e 0.063 1 nTCOcPBS1d nTCOcFRa # Distance PBS1 -> FR

m sf16a 0 998.E-3 0 nTCOcFRa nTCOcFRb
s rsFR 0.1 1.94 nTCOcFRb nTCOcFRc
m sf16b 0 998.E-3 0 nTCOcFRc nTCOcFRd

s rsFRe 0.055 1 nTCOcFRd nTCOcLama # Distance FR -> Lambda plate

m sf17a 0 998.E-3 0 nTCOcLama nTCOcLamb
s rsLam 0.002 1.45 nTCOcLamb nTCOcLamc
m sf17b 0 998.E-3 0 nTCOcLamc nTCOcLamd

# the following lens is on a remote-control moveable stage
# and can be shifted by about +-10mm keeping the sum of rsLame and rsPB2s const.
s rsLame 0.077 1 nTCOcLamd nTCOcL2a # Lambda plate -> L4b
lens l_L4b $F_L4b_fl nTCOcL2a nTCOcL2b
s rsPB2s 0.076 1 nTCOcL2b nTCOcBS2a # L4b -> PBS2

m sf18a 0 995.E-3 0 nTCOcBS2a nTCOcBS2b
s rsPB2 0.017 1.45 nTCOcBS2b nTCOcBS2c
m sf18b 0 995.E-3 0 nTCOcBS2c nTCOcBS2da

s s_sf18b_sf18c 0 nTCOcBS2da nTCOcBS2db
bs sf18c 0.E-3 995.E-3 0 45 nTCOcBS2db dump nTCOcBS2e nTCOcBS2f

# nTCOcBS2e output node for the carrier
# nTCOcBS2f output node for the sqz beam

s rs16 0.0601 1 nTCOcBS2e nOMC1_AR_w # Distance PBS2 -> OMC

#--------------------OMC-----------------------------------
# This is the newly installed (May 2013), slightly longer OMC!
# See GHF log p. 2860 + 4712
# Convention about the name of the node
# nOMC1_AR_w =  first mirror of the OMC, AR coating side, coming from the left
#
#                       /--\  OMCN
#
#
#
#
#
#                 /                   /
#       OMC1/           /    OMC2
#           /           /
#
#
#
#
#
#                 \--/  OMCS


bs OMC1_AR 1.E-3 999.E-3 0 41.652 nOMC1_AR_w dump nOMC1_AR_e dump
s rs17 0.0135 1.44963 nOMC1_AR_e nOMC1_HR_w
bs OMC1_HR 980.E-3 20.E-3 0 27.288 nOMC1_HR_w nOMC1_HR_n nOMC1_HR_e nOMC1_HR_s
s rs18 73.22E-3 1. nOMC1_HR_e  nOMC2_HR_w
bs OMC2_HR 980.E-3 20.E-3 0 41.652 nOMC2_HR_w nOMC2_HR_n nOMC2_HR_e nOMC2_HR_s
s rs19 153.81E-3 1. nOMC2_HR_n nOMCN_HR_w
bs OMCN_HR 999.9E-3 100.E-6 0 6.702 nOMCN_HR_w nOMCN_HR_n nOMCN_HR_e dump
attr OMCN_HR Rc 2.35
s rs20 307.62E-3 nOMCN_HR_n nOMCS_HR_n
bs OMCS_HR 1 0 0 6.711949 nOMCS_HR_w nOMCS_HR_n dump dump
attr OMCS_HR Rc 2.35

```

```
# Last path to close the OMC
s rs21 153.81E-3 1. nOMCS_HR_w nOMC1_HR_s

#####################################################

# Transmitted beam through the east mirror
s rs22 13.490E-3 1.44963 nOMC2_HR_e nOMC2_AR_w
bs OMC2_AR 1.E-3 999.E-3 0 27.185 nOMC2_AR_w dump nOMC2_AR_e dump
s rs23 1 nOMC2_AR_e n_dump_east
m sf-5 0 0 0 n_dump_east dump
# OMC cavity
cav OMC OMC1_HR nOMC1_HR_e OMC1_HR nOMC1_HR_s

# Transmitted beam through the north mirror
s rs24 12.0419E-3 1.44963 nOMCN_HR_e nOMCN_AR_w
bs OMCN_AR 1.E-3 999.E-3 0 4.779 nOMCN_AR_w dump nOMCN_AR_e dump
s rs25 1 nOMCN_AR_e  n_dump_north
m sf-6 0 0 0 n_dump_north dump

# Reflected beam from the west mirror
s rs26 13.490E-3 1.44963 nOMC1_HR_n nOMC1_AR2_w
bs OMC1_AR2 1.E-3 999.E-3 0 27.185 nOMC1_AR2_w dump nOMC1_AR2_e dump
# Reflected beam going toward BDO5
s rs27 290.284E-3 1. nOMC1_AR2_e nBDO5_w
bs BDO5_HR 5E-1 0 0 38.226 nBDO5_w nBDO5_n dump dump  # lossy!
#s mp1 0.775 1. nBDO5_n nLSB3a

#pd DC_carrier nBDO5_n #turn SBs off
#pd DC_SB nBDO5_w* # turn laser off
#noplot DC_SB

#pd DCcarrier nOMC1_AR2_e

s mp1 0.5 1. nBDO5_n nLSB3a

#ad Carrier 0 0 0 nBDO5_w*
#yaxis abs:deg

lens lsb3 0.5 nLSB3a nLSB3b
s mp2 0.758 nLSB3b nBDSB9w # Splitting for the two paths
bs DBSB9 0.5 0.5 0 45 nBDSB9w nBDSB9n nBDSB9e nBDSB9s

##-----------------------------------------------------------
# Near telescope

s mp3 0.057 nBDSB9n nScanner11
bs nScanner1 1 0 0 45 nScanner11 nScanner12 dump dump
s mp4 0.025 nScanner12 nScanner21 # 25mm vertical offset added for scanner mirrors
bs nScanner2 1 0 0 45 nScanner21 nScanner22 dump dump
s space 0.365 nScanner22 nLens1
lens LNear 0.3 nLens1 nLens2
s mp5 0.155 nLens2 QPDn

# QPD-near
pdtype QPDnearx1f x-split
pdtype QPDnearx2f x-split
pdtype QPDneary1f y-split
pdtype QPDneary2f y-split

# detectors
pd1 QPDnearxDC 0 QPDn
pd2 QPDnearx1f $fMI 150 6000 0 QPDn
pd1 QPDnearx2f 29.809864M 10 QPDn # 2f detector

pd QPDnearyDC QPDn
pd2 QPDneary1f $fMI 150 6000 0 QPDn
pd1 QPDneary2f 29.809864M 0 QPDn # check if demod phase is optimal
#pd1 DC2f 29.809864M QPDn
```

```
#pd1 DC1f $fMI QPDn

##-------------------------------------------------------------
# Far telescope

s mp6 0.352 nBDSB9e nLensf1
lens LFar 0.3 nLensf1 nLensf2
s mp7 0.2875 nLensf2 fScanner11
bs fScanner1 1 0 0 45 fScanner11 fScanner12 dump dump
s mp8 0.025 fScanner12 fScanner21 # 25mm vertical offset added for scanner mirrors
bs fScanner2 1 0 0 45 fScanner21 fScanner22 dump dump
s mp9 0.605 fScanner22 QPDf

# QPD-far

pd QPDfarxDC QPDf # DC signal of the split PD
pd2 QPDfarx1f $fMI 150 6000 0 QPDf
pd1 QPDfarx2f 29.809864M 0 QPDf # 2f detector
pd QPDfaryDC QPDf
pd2 QPDfary1f $fMI 150 6000 0 QPDf
pd1 QPDfary2f 29.809864M 0 QPDf

qshot shotnear 2 $fMI 150 6000 0 QPDn
qshot shotfar 2 $fMI 150 6000 0 QPDf

pdtype QPDfarx1f x-split
pdtype QPDfarx2f x-split
pdtype QPDfary1f y-split
pdtype QPDfary2f y-split
noplot QPDnearyDC
noplot QPDnearxDC
noplot QPDfarxDC
noplot QPDfaryDC
#noplot QPDnearx1f
noplot QPDnearx2f
noplot QPDfarx1f
noplot QPDfarx2f
noplot QPDneary1f
noplot QPDneary2f
noplot QPDfary2f
noplot QPDfary1f

# A little summary of the useful nodes:
#Input beam:                    nOMC1_AR_w
#Transmitted beam for HPD:      nOMC2_AR_e
#Transmitted beam for CCD:      nOMCN_AR_e
#Reflected beam:                nOMC1_AR2_e

##-------------------------------------------------------------
## further settings and commands

# Mode matching for OMC
const BDO1_RofC 6.27
const F_L4a_fl 0.25
const F_L4b_fl -0.0523 # this lens is on a moveable stage

# Modulation frequencies
const fMI 14.904932M ## (2/2014 H. Grote), crystal osc.

## -------------------------------------------------------------

# power detectors
pd1 Ptrans 0 nOMC2_AR_e # Transmitted beam (for the carrier from the ifo)

fsig OMCdither OMCN_HR phase 6000 0 # OMC length dither

#xaxis OMCN_HR phi lin 5 -5 1000 # Scan the OMC length
#yaxis lin abs:deg
```

```
noplot Ptrans
#pd DCn QPDn
#pd DCF QPDf

#pd1 DCn 0 QPDn
xaxis BDO1 xbeta lin -2e-6 2e-6 1000
#xaxis triplepend3 ybeta lin -2E-6 2E-6 1000
#xaxis MSR ybeta lin -5E-6 5E-6 1000
#xaxis nScanner1 xbeta lin -2e-6 2e-6 1000 # in radians
#scale ampere

# Plot Gouy phases
#gouy QPDGouyN x mp3 mp4 space mp5
#gouy QPDGouyF x mp6 mp7 mp8 mp9
#gouy BDOGouy x sout1 sout3
#gouy offsetBDO1 x sout1 mspace
#gouy BDO2OMC x rs14 rs14e rs14w rsl4a rsPB1 rsPBS1e rsFR rsFRe rsLam rsLame rsPB2s
    rsPB2

#attr BDO1 xbeta 10e-6
#beam spotdetector $fMI QPDn
#xaxis spotdetector x lin -1 1 2000

maxtem 2
gnuterm no
scale ampere
```

APPENDIX H

Circuit schematics

H.1 BDO coil driver circuit

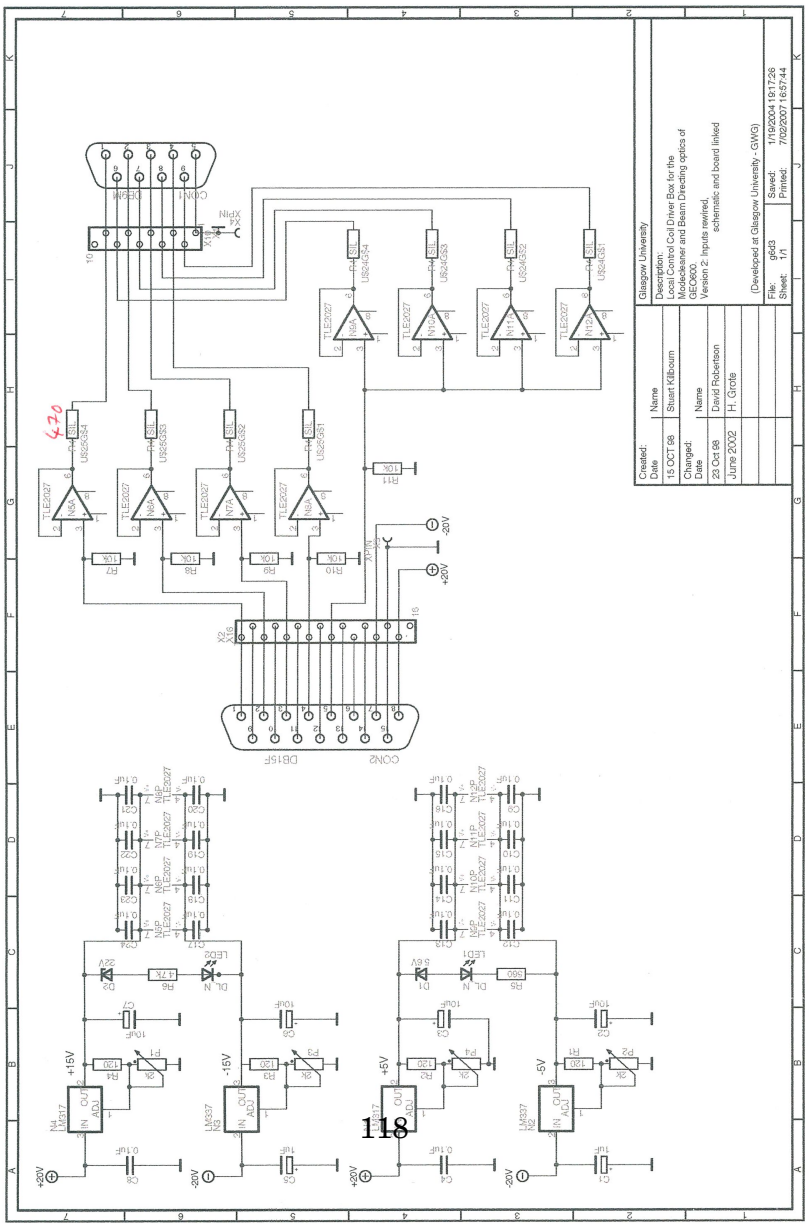

7/02/2007 16:57:44 f=0.90 /home/hrg/eagle/geo/localc/g6d3.sch (Sheet: 1/1)

H.2 BDO Local Control circuit

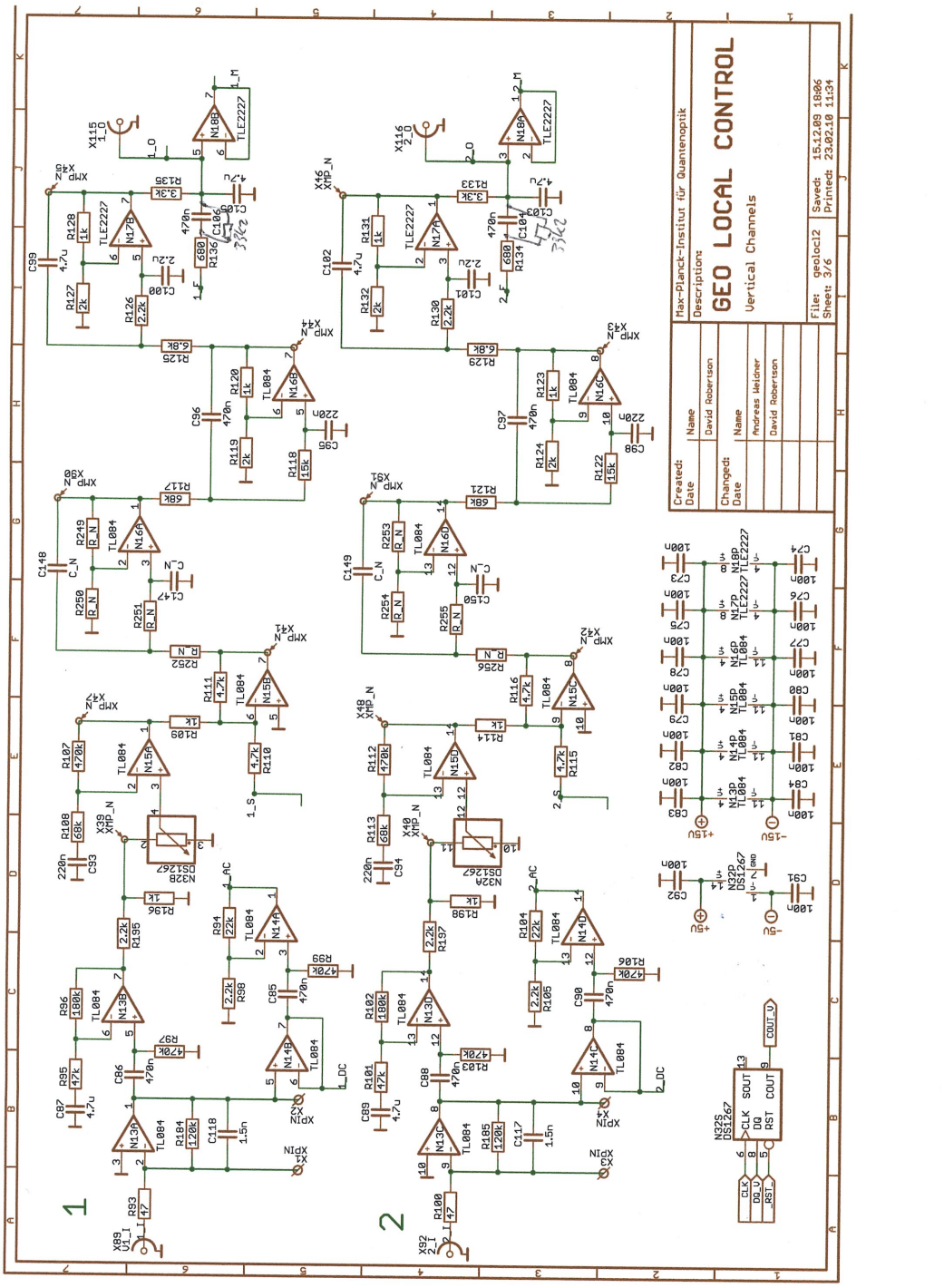

23.02.10 11:34 f=0.90 /home/hrg/eagle/projects/geo/localc/geolocl2.sch (Sheet: 3/6)

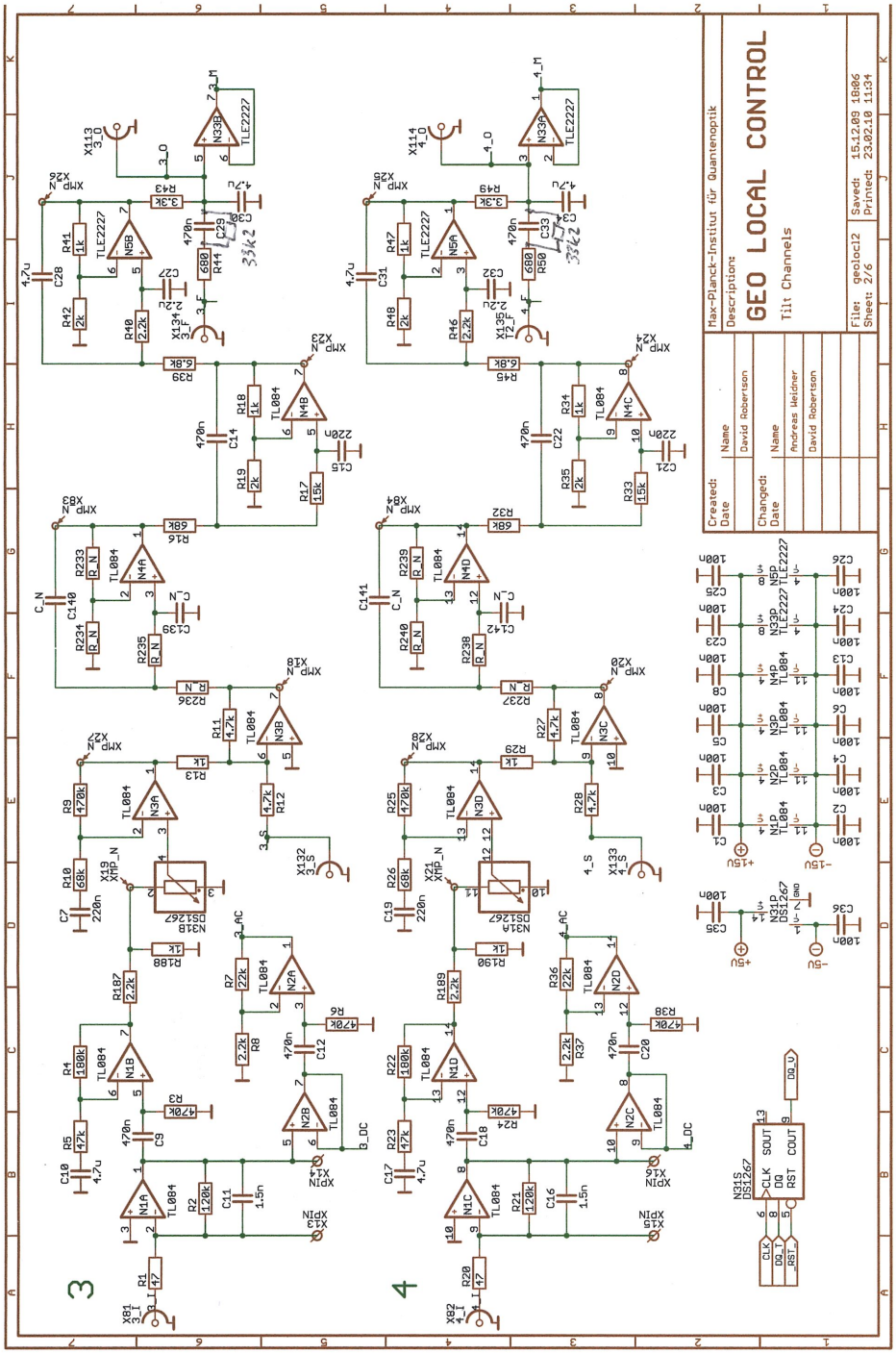
GEO LOCAL CONTROL
Tilt Channels
Max-Planck-Institut für Quantenoptik
Description:
Created: Name David Robertson
Changed: Name Andreas Weidner
David Robertson
Filet: geolocl2
Sheet: 2/6
Saved: 15.12.09 18:06
Printed: 23.02.10 11:34
3
4

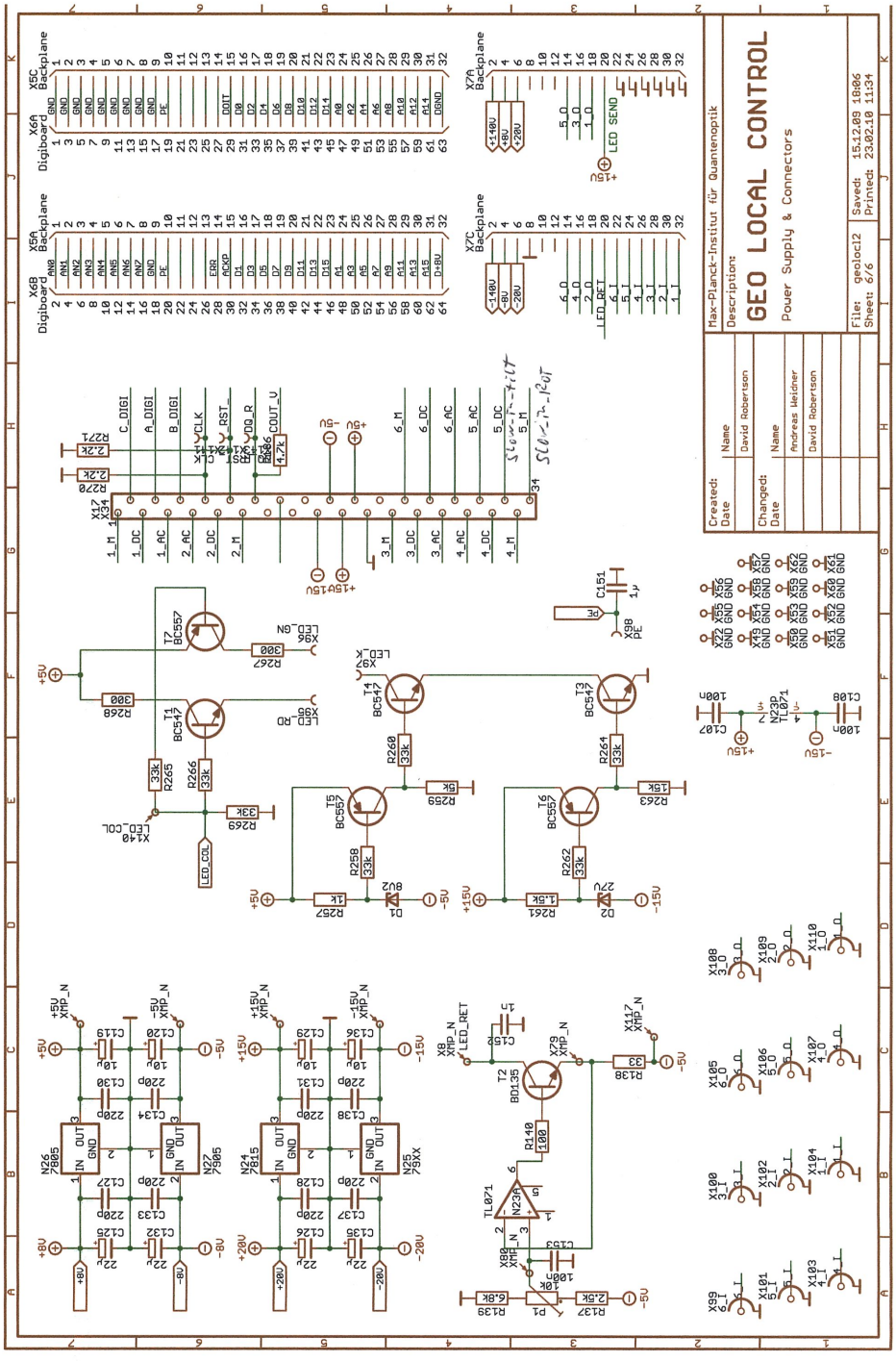
GEO LOCAL CONTROL
Power Supply & Connectors
Max-Planck-Institut für Quantenoptik
Description:
Created: Date
Name
David Robertson
Changed: Date
Name
Andreas Heidner
David Robertson
File: geolocl2
Sheet: 6/6
Saved: 15.12.09 18:06
Printed: 23.02.10 11:34
X5A Backplane
X5B Backplane
X5C Backplane
X6A Digiboard
X6B Digiboard
X7A Backplane
X7B Backplane
X7C Backplane
LED SEND
LED_RET
C_DIGI
A_DIGI
B_DIGI
SCLK
SDA
RST_
DOUT_R
COUT_U
1_M
1_DC
1_AC
2_AC
2_DC
2_M
3_M
3_DC
3_AC
4_AC
4_DC
4_M
5_M
5_DC
5_AC
6_AC
6_DC
6_M
LED_ON
LED_RD
LED_GN
LED_COL
T1 BC547
T2 BD135
T3 BC547
T4 BC547
T5 BC557
T6 BC557
T7 BC557
D1 8V2
D2 27V
TL071
N23P
N24 7815
N25 79XX
N26 7805
N27 7905
+5V
-5V
+8V
-8V
+15V
-15V
+20V
-20V
+5V_N
-5V_N
+15V_N
-15V_N
LED_K
LED_A
PE

Bibliography

[1] B.P. Abbott et al. (LIGO Scientific Collaboration and Virgo Collaboration): 'Observation of gravitational waves from a binary black hole merger'. Physical Review Letters 116, 2016.

[2] B.P. Abbott et al. (LIGO Scientific Collaboration and Virgo Collaboration): 'Observation of gravitational waves from a binary neutron star inspiral'. Physical Review Letters 119, 2017.

[3] LIGO website. (https://www.ligo.caltech.edu/).

[4] Virgo website. (http://www.virgo-gw.eu/).

[5] NASA GBM website. (https://fermi.gsfc.nasa.gov/science/instruments/gbm.html).

[6] Multiple collaborations, 'Low-latency Gravitational-wave Alerts for Multimessenger Astronomy during the Second Advanced LIGO and Virgo Observing Run'. The Astrophysical Journal, 875(2):161, Apr 2019.

[7] R. Abbott et al. GW190814: Gravitational waves from the coalescence of a 23 solar mass black hole with a 2.6 solar mass compact object. The Astrophysical Journal, 896(2):L44, Jun 2020.

[8] How gravitational waves could solve some of the Universe's deepest mysteries. Nature. June,2018.
(https://www.nature.com/articles/d41586-018-04157-6).

[9] Space-time. Wikipedia. https://simple.wikipedia.org/wiki/Space-time.

[10] scitechdaily.com. (https://scitechdaily.com/ligo-and-virgo-reveal-four-new-sources-of-gravitational-waves/).

[11] P.R. Saulson: 'Fundamentals of Interferometric Gravitational Wave Detectors'. World Scientific, 1994.

[12] A. A. Michelson, E. W. Morley: 'On the relative motion of the Earth and the luminiferous ether'. American Journal of Science s3-34.203, 1887.

[13] Odylio D. Aguiar, https://arxiv.org/pdf/1009.1138.pdf.

[14] Kagra website. (https://gwcenter.icrr.u-tokyo.ac.jp/en/).

[15] GEO 600 website. (https://www.geo600.org/).

[16] LIGO-India website. (https://www.ligo-india.in/).

[17] LSC website. (www.ligo.org).

[18] Gravitational Waves In The European Strategy For Particle Physics, ET Steering Committee, 2018.

[19] 3G R&D, R&D for the next generation of ground-based gravitational-wave detectors, GWIC, GWIC-3G, GWIC-3G-R&D-Consortium, 2019.

[20] M. Barsuglia talk: Future generation earth-based interferometric gravitational-wave detectors, Laboratoire Astroparticule Cosmologie - CNRS, 2015.

[21] S. Hild talk: Concepts for Third Generation Gravitational Wave Observatories. LISA Symposium, 2010. LIGO-G1000659-v1.

[22] J. Harms talk: Third Generation, Ground-Based, Gravitational-Wave Detectors. Universita degli studi Urbino.

[23] GWIC website. (https://gwic.ligo.org/3Gsubcomm/documents.shtml).

[24] LISA website. (https://www.lisa.nasa.gov/).

[25] GEO 600 research. (https://www.geo600.org/1265061/Research).

[26] LIGO document. (https://www.ligo.caltech.edu/system/media_files/binaries/313/original/LIGOHistory.pdf).

[27] B.P. Abbott et al. (LIGO Scientific Collaboration and Virgo Collaboration): 'GW190425: Observation of a Compact Binary Coalescence with Total Mass $\approx 3.4\ M_\odot$ '.

[28] B. J. Meers. 'Recycling in laser-interferometric gravitational-wave detectors'. Physical Review D. Third Series. Vol. 38, No. 8, 1988.

[29] H. Grote et al.: 'Dual Recycling for GEO 600'. Class and Quantum Gravity, Vol. 21, No. 5, 2004.

[30] B. Willke et al.: 'The GEO 600 gravitational wave detector'. Class and Quantum Gravity, Vol. 19, No. 7, 2002.

[31] H. Grote et al.: 'The GEO 600 status'. Class and Quantum Gravity, Vol. 27, No. 8, 2010.

[32] LSC publication: 'A gravitational wave observatory operating beyond the quantum shot-noise limit'. Nature Physics. Vol. 7, 2011.

[33] K. L. Dooley, J.R. Leong, T. Adams et al.: 'GEO 600 and the GEO-HF upgrade program: successes and challenges'. Class and Quantum Gravity, Vol. 33, No. 7, 2016.

[34] K. A. Strain and B J Meers. 'Experimental Demonstration of Dual Recycling for Interferometric Gravitational-Wave Detectors'. Physical Review Letters, Vol. 66, No. 11, 1991.

[35] G. Heinzel, K. A. Strain, J. Mizuno, et al. 'Experimental Demonstration of a Suspended Dual Recycling Interferometer for Gravitational Wave Detection'. Physical Review Letters, Vol. 81, No. 25, 1998.

[36] C. Affeldt, K. Danzmann, K. L . Dooley et al.: 'Advanced Techniques in GEO 600'. Classical and Quantum Gravity, Vol. 31, No. 22, 2014.

[37] L. Barsotti, M. Evans, P. Fritschel. 'Alignment sensing and control in advanced LIGO'. Classical and Quantum Gravity, Vol. 27, 2010.

[38] K. L. Dooley et al.: 'Phase control of squeezed vacuum states of light in gravitational wave detectors'. Optics Express, Vol. 23, No. 7, 2015.

[39] A. Abramovici and J. Chapsky: 'Feedback control systems A fast-track guide for scientists and engineers'. Springer Science+Business Media, LLC, 2000.

[40] J. H. Moore, C. C. Davis, M. A. Coplan: 'Building Scientific Apparatus'. Cambridge University Press, 2009.

[41] A. E. Siegman: 'Lasers'. University Science Books, 1986.

[42] H. Kogelnik, T. Li: 'Laser beams and resonators'. Applied Optics, Vol. 5, No. 10, 1966.

[43] E. Schreiber, K. L. Dooley, H. Vahlbruch et al.: 'Alignment sensing and control for squeezed vacuum states of light'. Optics Express, Vol. 24, Issue 1, 2016.

[44] E. Schreiber: 'Gravitational-wave detection beyond the quantum shot-noise limit : The integration of squeezed light in GEO 600'. PhD thesis, Gottfried Wilhelm Leibniz Universität, Hannover, 2018.

[45] J. Lough, E. Schreiber, F. Bergamin, et. al. 'First demonstration of 6 dB quantum noise reduction in a kilometer scale gravitational wave observatory'. **In publication**.

[46] C. Affeldt: 'Laser power increase for GEO600: Commissioning aspects towards an operation of GEO600 at high laser power'. PhD thesis, Gottfried Wilhelm Leibniz Universität Hannover, 2014.

[47] M. Prijatelj at al.: 'The output mode cleaner of GEO 600'. Classical and Quantum Gravity, Vol. 29, No. 5, 2012.

[48] M. Prijatelj et al.: 'Control and automatic alignment of the output mode cleaner of GEO 600'. J. Phys.: Conf. Ser., 228:012014, 2010.

[49] M. Prijatelj: 'Gravitational wave detection with pristine light: The implementation of an output mode cleaner at GEO 600'. PhD thesis, Gottfried Wilhelm Leibniz Universität Hannover, 2012.

[50] D.Z. Anderson 'Alignment of resonant optical cavities'. Applied Optics, Vol. 23, No. 17, 1984.

[51] E. Morrison, B. J. Meers, D. I. Robertson, and H. Ward. 'Automatic alignment of optical interferometers'. Applied Optics, 33 (22), 1994.

[52] E. Morrison, B. J. Meers, D. I. Robertson, and H. Ward. 'Experimental demonstration of an automatic alignment system for optical interferometers'. Applied Optics, 33 (22), 1994.

[53] R.W.P Drever et al.: 'Laser phase and frequency stabilization using an optical resonator'. Applied Physics, B 31, 97-105, 1983.

[54] E. Black: Notes on the Pound-Drever-Hall technique, LIGO Technical Note, LIGO-T980045.

[55] N. Mavalvala: 'Alignment Issues In Laser Interferometric Gravitational-Wave Detectors'. PhD thesis, Massachusetts Institute of Technology, 1997.

[56] G. Heinzel: 'Advanced optical techniques for laser-interferometric gravitational wave detectors'. PhD thesis, Universität Hannover, 1999.

[57] A. Freise: 'The Next Generation of Interferometry: Multi-Frequency Optical Modelling, Control Concepts and Implementation'. PhD thesis, Gottfried Wilhelm Leibniz Universität Hannover, 2003.

[58] S. Hild: 'Beyond the first Generation: Extending the Science Range of the Gravitational Wave Detector GEO 600 '. PhD thesis, Gottfried Wilhelm Leibniz Universität Hannover, 2007.

[59] S. Goßler: 'The suspension systems of the interferometric gravitational-wave detector GEO 600'. PhD thesis, Gottfried Wilhelm Leibniz Universität Hannover, 2007.

[60] Matlab website address: https://de.mathworks.com/products/simulink.html.

[61] Mathematica website address: https://www.wolfram.com/mathematica/

[62] D. Shoemaker et al.: 'Noise behaviour of the Garching 30-meter prototype gravitational-wave detector'. Physical Review D, Particles and Fields, Third SEries, Vol. 38, No. 2, 1988.

[63] L. Carbone, S. M. Aston, R. M. Cutler et al.: 'Sensors and actuators for the advanced LIGO mirror suspensions'. Classical and Quantum Gravity, Vol. 29, No. 11, 2012.

[64] M. Barton: 'Calculation and measurement of the OSEM actuator sweet spot position', LIGO-T1000164-v3.

[65] K. A. Strain and B. N. Shapiro: 'Damping and local control of mirror suspensions for laser interferometric gravitational wave detectors'. Rev. Sci. Instrum. 83, 044501, 2012.

[66] H. Wittel: 'Active and passive reduction of higher order modes in the gravitational wave detector GEO 600'. PhD thesis, Gottfried Wilhelm Leibniz Universität Hannover, 2015.

[67] S. Hild, H. Grote, J. Degallaix et al.: 'DC-readout of a signal-recycled gravitational wave detector'. Classical and Quantum Gravity, Vol. 26, No. 5, 2008.

[68] T. Fricke et al.: 'DC readout experiment in Enhanced LIGO'. Classical and Quantum Gravity, Vol. 29, No. 6, 2008.

[69] D. Martynov: 'Lock Acquisition and Sensitivity Analysis of Advanced LIGO Interferometers'. PhD thesis, California Institute of technology, Pasadena, California, 2015.

[70] P. F. Gascoyne and H N Rutt 1983 J. Phys. E: Sci. Instrum. 16 31.

[71] K. Kawabe, N. Mio, K. Tsubono: 'Automatic alignment-control system for a suspended Fabry-perot cavity'. Applied Optics, Vol. 33, No. 24, 1994.

[72] N. Smith-Lefebvre, S. Ballmer, M. Evans et al.: 'Optimal Alignment Sensing of a Readout Mode Cleaner Cavity'. Optics Letters, 36:4365–4367, 2011.

[73] H. Grote: 'Making it work : Second generation interferometry in GEO 600'. PhD thesis, Gottfried Wilhelm Leibniz Universität, Hannover, 2003.

[74] N. Smith: a la mode: Mode matching and beam propagation solutions for Matlab, 2016.

[75] K. Dooley talk: Design principles for an alignment system, GEO ISC Meeting, 2012.

[76] K. Dooley: 'Design and performance of high laser power interferometers for gravitational -wave detection'. PhD thesis, University of Florida, 2011.

[77] J.R. Smith: 'Formulation of Instrument Noise Analysis Techniques and Their Use in the Commissioning of the Gravitational Wave Observatory, GEO 600'. PhD thesis, Gottfried Wilhelm Leibniz Universität, Hannover, 2006.

[78] N. Smith: 'Techniques for Improving the readout Sensitivity of Gravitational Wave Antennae'. PhD thesis, Massachusetts Institute of Technology, 2012.

[79] R. Bork, M. Aronsson, A. Ivanov: aLIGO CDS Real-time Code Generator (RCG V2.8), Application Developer's Guide. LIGO-T080135-v9.

[80] FINESSE website address: www.gwoptics/finesse

[81] Paul Fulda talk: FINESSE: What is it, what does it do, and why am I learning it ? (http://www.phys.ufl.edu/p̃fulda/FinesseTutorial_1.pdf).

[82] Mathematica. version 11.0.1.0. Champaign, IL: Wolfram Research, Inc., 2016.

[83] M. Barton: 'Models of the Advanced LIGO Suspensions in Mathematica. Tech. rep. T020205-v2. LIGO Laboratory / LIGO Scientific Collaboration', 2014.

[84] BDO suspension model with twisty cantilever blades: https://redoubt.ligo-wa.caltech.edu/svn/sus/trunk/Common /MathematicaModels/FourWireSimpleTwoTwistyBlades.

[85] C. I. E. Torrie: 'Development of suspensions for the GEO 600 gravitational wave detector', PhD thesis, University of Glasgow, 2000.

[86] J. S. Hennig: 'Mirror suspensions for the Glasgow Sagnac speed meter', PhD thesis, University of Glsgow, 2018.

[87] Datasheet of the QPDs used at GEO 600: https://www.datasheets360.com/pdf/4394236095907334703.

[88] R. Kirchoff, C. M. Mow-Lowry, V. B. Adya et al: 'Huddle test measurement of a near Johnson noise limited geophone'. Review of Scientific Instruments, Vol. 88, 2017.

[89] Entry in the GEO-HF logbook, page 7783.

[90] Entry in the GEO-HF logbook, page 8367 and page 7968.

[91] C. Wipf talk: Noise budgeting for advanced detectors. GWADW 2014, LIGO-G1400587.

[92] SimulinkNb: https://github.com/cwipf/SimulinkNb.

Curriculum Vitae

Personal data

Name : Aparna Bisht
Nationality : Indian
Date of birth : 28.02.1991
Place of birth : Nainital, India

Education

2011	Bachelor of Science in Physics (Hons.), Hans Raj College, University of Delhi, India
2014	Master of Science in Physics, National Institute of Technology, Surathkal, India
2020	Doctor of Philosophy, Max Planck Institute for Gravitational Physics, Hannover, Germany

Fellowship and awards

2010	Summer Research Fellowship awarded by the Indian Academy of Sciences.
2016	Special Breakthrough Prize in Fundamental Physics as a member of the LIGO Scientific Collaboration.
2016	The Gruber Cosmology Prize as a member of the LIGO Discovery Team.
2017	Princess of Asturias Award for Technical and Scientific Research as a member of the LSC.

Publications

1 Publications as member of the GEO 600 group

- E. Schreiber, K. L. Dooley, H. Vahlbruch, C. Affeldt, A. Bisht, J. R. Leong, J. Lough, M. Prijatelj, J. Slutsky, M. Was, H. Wittel, K. Danzmann, and H. Grote. 'Alignment sensing and control for squeezed vacuum states of light '. *Opt. Express*, 24(1):146–152, Jan 2016

- K L Dooley, J R Leong, T Adams, C Affeldt, A Bisht, C Bogan, J Degallaix, C Grf, S Hild, J Hough, and et al. 'GEO 600 and the GEO-HF upgrade program: successes and challenges '. *Classical and Quantum Gravity*, 33(7):075009, Mar 2016

- H. Wittel, C. Affeldt, A. Bisht, S. Doravari, H. Grote, J. Lough, H. Lück, E. Schreiber, K. A. Strain, and K. Danzmann. 'Matrix heater in the gravitational wave observatory GEO 600 '. *Opt. Express*, 26(18):22687–22697, Sep 2018

- N. Mukund, J. Lough, C. Affeldt, F. Bergamin, A. Bisht, M. Brinkmann, V. Kringel, H. Lück, S. Nadji, M. Weinert, and et al. 'Bilinear noise subtraction at the GEO 600 observatory '. *Physical Review D*, 101(10), May 2020

- J. Lough, E. Schreiber, F. Bergamin, H. Grote, M. Mehmet, H. Vahlbruch, C. Affeldt, M. Brinkmann, A. Bisht, V. Kringel, H. Lück, N. Mukund, S. Nadji, B. Sorazu, K. Strain, M. Weinert, K. Danzmann.'First demonstration of 6 dB quantum noise reduction in a kilometer scale gravitational wave observatory'. *Physical Review Letters 126, 041102 (2021)*

- A. Bisht, M. Prijatelj, J. Leong, E. Schreiber, C. Affeldt, M. Brinkmann, K. Danzmann, S. Doravari, H. Grote, V. Kringel, J. Lough, H. Lück, K. Strain, M. Weinert, K. Danzmann. 'Modulated Differential Wavefront Sensing : alignment scheme for beams with large higher order mode content'. *Galaxies* 2020,8,81.

2 Publications as member of the LSC

- B. P. Abbott...., A. Bisht...., and J. Zweizig. 'All-sky search for long-duration gravitational wave transients with initial LIGO '. *Phys. Rev. D*, 93:042005, Feb 2016
- B. P. Abbott...., A. Bisht...., and J. Zweizig. 'GW150914: Implications for the Stochastic Gravitational-Wave Background from Binary Black Holes'. *Phys. Rev. Lett.*, 116:131102, Mar 2016
- B. P. Abbott...., A. Bisht...., and J. Zweizig. 'Astrophysical implications of the binary black hole merger GW150914 '. *The Astrophysical Journal*, 818(2):L22, Feb 2016
- B. P. Abbott...., A. Bisht...., and J. Zweizig. 'Calibration of the Advanced LIGO detectors for the discovery of the binary black-hole merger GW150914 '. *Phys. Rev. D*, 95:062003, Mar 2017
- B. P. Abbott...., A. Bisht...., and J. Zweizig. 'Characterization of transient noise in Advanced LIGO relevant to gravitational wave signal GW150914'. *Classical and Quantum Gravity*, 33(13):134001, Jun 2016
- B. P. Abbott...., A. Bisht...., and J. Zweizig. 'Observing gravitational-wave transient GW150914 with minimal assumptions '. *Phys. Rev. D*, 93:122004, Jun 2016
- B. P. Abbott...., A. Bisht...., and J. Zweizig. 'The rate of binary black hole mergers inferred from advanced LIGO observations surrounding GW150914 '. *The Astrophysical Journal*, 833(1):L1, Nov 2016
- B. P. Abbott...., A. Bisht...., and Y. Zlochower. 'Tests of General Relativity with GW150914 '. *Phys. Rev. Lett.*, 116:221101, May 2016
- B. P. Abbott...., A. Bisht...., and Y. Zlochower. 'Properties of the Binary Black Hole Merger GW150914 '. *Phys. Rev. Lett.*, 116:241102, Jun 2016
- B. P. Abbott...., A. Bisht...., and J. Zweizig. 'GW150914: First results from the search for binary black hole coalescence with Advanced LIGO '. *Phys. Rev. D*, 93:122003, Jun 2016
- B. P. Abbott...., A. Bisht...., and J. Zweizig. 'GW150914: The Advanced LIGO Detectors in the Era of First Discoveries '. *Phys. Rev. Lett.*, 116:131103, Mar 2016
- B. P. Abbott...., A. Bisht...., and J. Zweizig. 'Observation of Gravitational Waves from a Binary Black Hole Merger '. *Phys. Rev. Lett.*, 116:061102, Feb 2016

- B. P. Abbott...., A. Bisht...., and S. Rosswog. 'Localization and broadband follow-up of the gravitational -wave transient GW150914 '. *The Astrophysical Journal*, 826(1):L13, Jul 2016

- B. P. Abbott...., A. Bisht...., and J. Zweizig. 'First targeted search for gravitational-wave bursts from core-collapse supernovae in data of first-generation laser interferometer detectors '. *Phys. Rev. D*, 94:102001, Nov 2016

- B. P. Abbott...., A. Bisht...., and B. L. Wells. 'Search for transient gravitational waves in coincidence with short-duration radio transients during 2007–2013 '. *Phys. Rev. D*, 93:122008, Jun 2016

- B. P. Abbott...., A. Bisht...., and J. Zweizig. 'Comprehensive all-sky search for periodic gravitational waves in the sixth science run LIGO data '. *Phys. Rev. D*, 94:042002, Aug 2016

- B. P. Abbott...., A. Bisht...., and Y. Zlochower. 'Directly comparing GW150914 with numerical solutions of Einstein's equations for binary black hole coalescence '. *Phys. Rev. D*, 94:064035, Sep 2016

- B. P. Abbott...., A. Bisht...., and Y. Zlochower. 'Improved Analysis of GW150914 Using a Fully Spin-Precessing Waveform Model '. *Phys. Rev. X*, 6:041014, Oct 2016

- B. P. Abbott...., A. Bisht...., and J. Zweizig. 'Binary Black Hole Mergers in the First Advanced LIGO Observing Run '. *Phys. Rev. X*, 6:041015, Oct 2016

- B. P. Abbott...., A. Bisht...., and S. Teukolsky. 'GW151226: Observation of Gravitational Waves from a 22-Solar-Mass Binary Black Hole Coalescence '. *Phys. Rev. Lett.*, 116:241103, Jun 2016

- B. P. Abbott...., A. Bisht...., and J. Zweizig. 'Results of the deepest all-sky survey for continuous gravitational waves on LIGO S6 data running on the Einstein@Home volunteer distributed computing project '. *Phys. Rev. D*, 94:102002, Nov 2016

- B. P. Abbott...., A. Bisht...., and S. Sigurdsson. 'Search for continuous gravitational waves from neutron stars in globular cluster NGC 6544 '. *Phys. Rev. D*, 95:082005, Apr 2017

- B. P. Abbott...., A. Bisht...., and J. Zweizig. 'Upper limits on the rates of binary neutron star and neutron star -black hole mergers from advanced LIGO's first observation run '. *The Astrophysical Journal*, 832(2):L21, Nov 2016

- B. P. Abbott...., A. Bisht...., and J. Harms. 'Exploring the sensitivity of next generation gravitational wave detectors '. *Classical and Quantum Gravity*, 34(4):044001, Jan 2017

- B. P. Abbott...., A. Bisht...., and J. Zweizig. 'All-sky search for short gravitational-wave bursts in the first Advanced LIGO run '. *Phys. Rev. D*, 95:042003, Feb 2017

- B. P. Abbott...., A. Bisht...., and A. Vano Vinuales. 'Effects of waveform model systematics on the interpretation of GW150914 '. *Classical and Quantum Gravity*, 34(10):104002, Apr 2017

- B. P. Abbott...., A. Bisht...., and X. Zhang. 'Search for Gravitational Waves Associated with Gamma-Ray Bursts during the First Advanced LIGO Observing Run and Implications for the Origin of GRB 150906B '. *The Astrophysical Journal*, 841(2):89, May 2017

- B. P. Abbott...., A. Bisht...., and J. Zweizig. 'Directional Limits on Persistent Gravitational Waves from Advanced LIGO's First Observing Run '. *Phys. Rev. Lett.*, 118:121102, Mar 2017

- B. P. Abbott...., A. Bisht...., and J. Zweizig. 'Upper Limits on the Stochastic Gravitational-Wave Background from Advanced LIGO's First Observing Run '. *Phys. Rev. Lett.*, 118:121101, Mar 2017

- B. P. Abbott...., A. Bisht...., and P. Weltevrede. 'First Search for Gravitational Waves from Known Pulsars with Advanced LIGO '. *The Astrophysical Journal*, 839(1):12, Apr 2017

- A. Albert...., A. Bisht...., and J. Zweizig. 'Search for high-energy neutrinos from gravitational wave event GW151226 and candidate LVT151012 with ANTARES and IceCube '. *Phys. Rev. D*, 96:022005, Jul 2017

- B. P. Abbott...., A. Bisht...., and R. J. Evans. Search for gravitational waves from scorpius x-1 in the first advanced ligo observing run with a hidden markov model. *Phys. Rev. D*, 95:122003, Jun 2017

- B. P. Abbott...., A. Bisht...., and J. Zweizig. 'Search for intermediate mass black hole binaries in the first observing run of Advanced LIGO '. *Phys. Rev. D*, 96:022001, Jul 2017

- B. P. Abbott...., A. Bisht...., and J. Zweizig. 'GW170104: Observation of a 50-Solar-Mass Binary Black Hole Coalescence at Redshift 0.2 '. *Phys. Rev. Lett.*, 118:221101, Jun 2017

- B. P. Abbott...., A. Bisht...., and L. Wang. 'Upper Limits on Gravitational Waves from Scorpius X-1 from a Model-based Cross-correlation Search in Advanced LIGO Data '. *The Astrophysical Journal*, 847(1):47, Sep 2017

- B. P. Abbott...., A. Bisht...., and D. P. Anderson. 'First low-frequency Einstein@Home all-sky search for continuous gravitational waves in Advanced LIGO data '. *Phys. Rev. D*, 96:122004, Dec 2017

- B. P. Abbott...., A. Bisht...., and J. Zweizig. 'GW170814: A Three-Detector Observation of Gravitational Waves from a Binary Black Hole Coalescence '. *Phys. Rev. Lett.*, 119:141101, Oct 2017

- B. P. Abbott...., A. Bisht...., and J. Zweizig. 'All-sky search for periodic gravitational waves in the O1 LIGO data '. *Phys. Rev. D*, 96:062002, Sep 2017

- B. P. Abbott...., A. Bisht...., and P. Weltevrede. 'First Search for Nontensorial Gravitational Waves from Known Pulsars '. *Phys. Rev. Lett.*, 120:031104, Jan 2018

- B. P. Abbott...., A. Bisht...., and J. Zweizig. 'Effects of data quality vetoes on a search for compact binary coalescences in Advanced LIGO's first observing run '. *Classical and Quantum Gravity*, 35(6):065010, Feb 2018

- B. P. Abbott...., A. Bisht...., and J. Zweizig. 'First narrow-band search for continuous gravitational waves from known pulsars in advanced detector data '. *Phys. Rev. D*, 96:122006, Dec 2017

- A. Albert...., A. Bisht...., and J. Zweizig. Search for high-energy neutrinos from binary neutron star merger GW170817 with ANTARES, IceCube, and the pierre auger observatory. *The Astrophysical Journal*, 850(2):L35, Nov 2017

- A. Albert...., A. Bisht...., and J. Zweizig. 'On the Progenitor of Binary Neutron Star Merger GW170817 '. *The Astrophysical Journal*, 850(2):L40, dec 2017

- B. P. Abbott...., A. Bisht...., and J. Zweizig. 'GW170817: Implications for the Stochastic Gravitational-Wave Background from Compact Binary Coalescences '. *Phys. Rev. Lett.*, 120:091101, Feb 2018

- B. P. Abbott...., A. Bisht...., and J. Zweizig. 'Estimating the Contribution of Dynamical Ejecta in the Kilonova Associated with GW170817 '. *The Astrophysical Journal*, 850(2):L39, Dec 2017

- B. P. Abbott...., A. Bisht...., and P. Ubertini. 'Gravitational Waves and Gamma-Rays from a Binary Neutron Star Merger: GW170817 and GRB 170817A '. *The Astrophysical Journal*, 848(2):L13, Oct 2017

- B. P. Abbott...., A. Bisht...., and A. Woudt. 'Multi-messenger Observations of a Binary Neutron Star Merger '. *The Astrophysical Journal*, 848(2):L12, Oct 2017

- B. P. Abbott...., A. Bisht...., and J. Zweizig. 'GW170817: Observation of Gravitational Waves from a Binary Neutron Star Inspiral '. *Phys. Rev. Lett.*, 119:161101, Oct 2017

- B. P. Abbott...., A. Bisht...., and J. Zweizig. 'Search for Post-merger Gravitational Waves from the Remnant of the Binary Neutron Star Merger GW170817 '. *The Astrophysical Journal*, 851(1):L16, Dec 2017

- B. P. Abbott...., A. Bisht...., and J. Zweizig. GW170608: Observation of a 19 solar-mass binary black hole coalescence. *The Astrophysical Journal*, 851(2):L35, Dec 2017

- B. P. Abbott...., A. Bisht...., and J. Zweizig. 'All-sky search for long-duration gravitational wave transients in the first Advanced LIGO observing run '. *Classical and Quantum Gravity*, 35(6):065009, Feb 2018

- B. P. Abbott...., A. Bisht...., and J. Zweizig. 'Constraints on cosmic strings using data from the first Advanced LIGO observing run '. *Phys. Rev. D*, 97:102002, May 2018

- B. P. Abbott...., A. Bisht...., and J. Zweizig. 'Full band all-sky search for periodic gravitational waves in the O1 LIGO data '. *Phys. Rev. D*, 97:102003, May 2018

- B. P. Abbott...., A. Bisht...., and J. Zweizig. 'Search for Tensor, Vector, and Scalar Polarizations in the Stochastic Gravitational-Wave Background '. *Phys. Rev. Lett.*, 120:201102, May 2018

- B. P. Abbott...., A. Bisht...., and J. Zweizig. 'GW170817: Measurements of Neutron Star Radii and Equation of State '. *Phys. Rev. Lett.*, 121:161101, Oct 2018

- B. P. Abbott...., A. Bisht...., and J. Zweizig. 'Properties of the Binary Neutron Star Merger GW170817 '. *Phys. Rev. X*, 9:011001, Jan 2019

- B. P. Abbott...., A. Bisht...., and S. Shandera. 'Search for Subsolar-Mass Ultracompact Binaries in Advanced LIGO's First Observing Run '. *Phys. Rev. Lett.*, 121:231103, Dec 2018

- B. P. Abbott...., A. Bisht...., and N. N. Weinberg. 'Constraining the p-Mode–g-Mode Tidal Instability with GW170817 '. *Phys. Rev. Lett.*, 122:061104, Feb 2019

- E. Burns...., A. Bisht...., and J. Zweizig. 'A Fermi Gamma-Ray Burst Monitor Search for Electromagnetic Signals Coincident with Gravitational-wave Candidates in Advanced LIGO's First Observing Run '. *The Astrophysical Journal*, 871(1):90, Jan 2019

- B. P. Abbott...., A. Bisht...., and J. Zweizig. 'Search for Gravitational Waves from a Long-lived Remnant of the Binary Neutron Star Merger GW170817 '. *The Astrophysical Journal*, 875(2):160, Apr 2019

- A. Albert...., A. Bisht...., and J. Zweizig. 'Search for Multimessenger Sources of Gravitational Waves and High-energy Neutrinos with Advanced LIGO during Its First Observing Run, ANTARES, and IceCube '. *The Astrophysical Journal*, 870(2):134, Jan 2019

- B. P. Abbott...., A. Bisht...., and J. Zweizig. 'Tests of General Relativity with GW170817 '. *Phys. Rev. Lett.*, 123:011102, Jul 2019

- B. P. Abbott...., A. Bisht...., and J. Zweizig. 'Binary Black Hole Population Properties Inferred from the First and Second Observing Runs of Advanced LIGO and Advanced Virgo '. *The Astrophysical Journal*, 882(2):L24, Sep 2019

- B. P. Abbott...., A. Bisht...., and J. Zweizig. 'GWTC-1: A Gravitational-Wave Transient Catalog of Compact Binary Mergers Observed by LIGO and Virgo during the First and Second Observing Runs '. *Phys. Rev. X*, 9:031040, Sep 2019

- B. P. Abbott...., A. Bisht...., and J. Zweizig. 'Searches for Continuous Gravitational Waves from 15 Supernova Remnants and Fomalhaut b with Advanced LIGO ', journal = The Astrophysical Journal,. 875(2):122, Apr 2019

- M. Soares-Santos...., A. Bisht...., and J. Zweizig. 'First Measurement of the Hubble Constant from a Dark Standard Siren using the Dark Energy Survey Galaxies and

the LIGO/Virgo Binary-Black-hole Merger GW170814 '. *The Astrophysical Journal*, 876(1):L7, Apr 2019

- B. P. Abbott...., A. Bisht...., and J. Zweizig. 'Low-latency Gravitational-wave Alerts for Multimessenger Astronomy during the Second Advanced LIGO and Virgo Observing Run '. *The Astrophysical Journal*, 875(2):161, Apr 2019

- B. P. Abbott...., A. Bisht...., and J. Zweizig. 'Search for Transient Gravitational-wave Signals Associated with Magnetar Bursts during Advanced LIGO's Second Observing Run '. *The Astrophysical Journal*, 874(2):163, Apr 2019

- B. P. Abbott...., A. Bisht...., and P. Weltervrede. 'Searches for Gravitational Waves from Known Pulsars at Two Harmonics in 2015-2017 LIGO Data '. *The Astrophysical Journal*, 879(1):10, Jun 2019

- B. P. Abbott...., A. Bisht...., and P. Weltervrede. 'Narrow-band search for gravitational waves from known pulsars using the second LIGO observing run '. *Phys. Rev. D*, 99:122002, Jun 2019

- B. P. Abbott...., A. Bisht...., and A. Pisarski. 'All-sky search for continuous gravitational waves from isolated neutron stars using Advanced LIGO O2 data '. *Phys. Rev. D*, 100:024004, Jul 2019

- B. P. Abbott...., A. Bisht...., and J. Zweizig. 'Search for the isotropic stochastic background using data from Advanced LIGO's second observing run '. *Phys. Rev. D*, 100:061101, Sep 2019

- B. P. Abbott...., A. Bisht...., and J. Zweizig. 'Tests of general relativity with the binary black hole signals from the LIGO-Virgo catalog GWTC-1 '. *Phys. Rev. D*, 100:104036, Nov 2019

- B. P. Abbott...., A. Bisht...., and J. Zweizig. 'Directional limits on persistent gravitational waves using data from Advanced LIGO's first two observing runs '. *Phys. Rev. D*, 100:062001, Sep 2019

- B. P. Abbott...., A. Bisht...., and J. Zweizig. 'All-sky search for long-duration gravitational-wave transients in the second Advanced LIGO observing run '. *Phys. Rev. D*, 99:104033, May 2019

- B. P. Abbott...., A. Bisht...., and S. Shandera. 'Search for Subsolar Mass Ultracompact Binaries in Advanced LIGO's Second Observing Run '. *Phys. Rev. Lett.*, 123:161102, Oct 2019

- B. P. Abbott...., A. Bisht...., and F. Salemi. 'All-sky search for short gravitational-wave bursts in the second Advanced LIGO and Advanced Virgo run '. *Phys. Rev. D*, 100:024017, Jul 2019

- B. P. Abbott...., A. Bisht...., and M. A. Papa. 'Search for intermediate mass black hole binaries in the first and second observing runs of the Advanced LIGO and Virgo network '. *Phys. Rev. D*, 100:064064, Sep 2019

- B. P. Abbott...., A. Bisht...., and W. Moran. 'Search for gravitational waves from Scorpius X-1 in the second Advanced LIGO observing run with an improved hidden Markov model '. *Phys. Rev. D*, 100:122002, Dec 2019

- B. P. Abbott...., A. Bisht...., and Badri Krishnan. 'Search for Gravitational-wave Signals Associated with Gamma-Ray Bursts during the Second Observing Run of Advanced LIGO and Advanced Virgo '. *The Astrophysical Journal*, 886(1):75, Nov 2019

- B. P. Abbott...., A. Bisht...., and F. Salemi. 'Search for Eccentric Binary Black Hole Mergers with Advanced LIGO and Advanced Virgo during Their First and Second Observing Runs '. *The Astrophysical Journal*, 883(2):149, Sep 2019

- B. P. Abbott...., A. Bisht...., and J. Zweizig. 'Model comparison from LIGO-Virgo data on GW170817's binary components and consequences for the merger remnant '. *Classical and Quantum Gravity*, 37(4):045006, Jan 2020

- B. P. Abbott...., A. Bisht...., and F. Salemi. 'Optically targeted search for gravitational waves emitted by core-collapse supernovae during the first and second observing runs of advanced LIGO and advanced Virgo '. *Phys. Rev. D*, 101:084002, Apr 2020

- B. P. Abbott...., A. Bisht...., and J. Zweizig. 'A guide to LIGO-Virgo detector noise and extraction of transient gravitational-wave signals '. *Classical and Quantum Gravity*, 37(5):055002, Feb 2020

- R. Hamburg...., A. Bisht...., and J. Zweizig. 'A Joint Fermi-GBM and LIGO/Virgo Analysis of Compact Binary Mergers from the First and Second Gravitational-wave Observing Runs '. *The Astrophysical Journal*, 893(2):100, Apr 2020

- B. P. Abbott...., A. Bisht...., and J. Zweizig. 'GW190425: Observation of a Compact Binary Coalescence with Total Mass $\sim$ 3.4 M $\odot$ '. *The Astrophysical Journal*, 892(1):L3, Mar 2020

- The LIGO Scientific Collaboration and the Virgo Collaboration. 'GW190412: Observation of a binary-black-hole coalescence with asymmetric masses', 2020
- R. Abbott, ...Bisht A., and Zweizig J. 'GW190814: Gravitational waves from the coalescence of a 23 solar mass black hole with a 2.6 solar mass compact object'. *The Astrophysical Journal*, 896(2):L44, Jun 2020

Acknowledgements

"Nothing in life is to feared. It is only to be understood. Now is the time to understand more, so that we may fear less."

Looking at my journey as a PhD student, this one quote by Marie Curie sums up most of my fears, success and motivation of moving ahead and any of this would not have been possible without all the wonderful people who helped me in my pursuit!

I am truly thankful to Prof. Karsten Danzmann for giving me the opportunity to begin my research career at such a great institute and for being a powerhouse of positivity and enthusiasm. I would like to thank Hartmut Grote and Jonathan Leong for helping me with the first steps of getting to know GEO 600 and for being so approachable and warm all through these years. To Mirko - thank you for your patience in filling up the gaps in my knowledge and for helping me overcome my fears of being a total stranger to this incredible field of research. Dear Emil and Holger, thank you for being friends first and colleagues later. I deeply admire how versatile you both are and for being the 'they-WILL-know' people that I have looked up to.

I would like to thank Harald and Ken for being the out-of-loop sensors of progress. Your instinct and eagerness to learn something new is unparalleled! I am deeply indebted to Benno for the most valuable supervision and guidance throughout my PhD time. I am very thankful to Mark Barton for his help in suspension modelling as well as to Jan-Simon Hennig for getting me started with the modelling work. I am grateful to you Jim, for encouraging me to think like a real scientist and for being an unofficial mentor. To the GEO on-site team - Christoph, Jim, Fabio, Marc, Michael, Nikhil, Severin, Volker, Walter, thank you all for the great environment and for being a TEAM! The sunny barbeque days at GEO and strictly after work drinking are some of my fondest memories of being on site. OUR beautiful site!

This thesis would not have possible at all without the two of you - Christoph and Suresh. This journey has been yours as much as it has been mine. Christoph, thank you for going that extra mile for my well being of all sorts. Be it reports, posters, talks, approvals and this thesis, you have really made all of it happen. Suresh, you've taught me that research is a way of living and being curious is

a full time job! Thank you for making my visits to IUCAA truly enriching.

My Hannover-time was blessed in the company of these amazing fellow women - Marina, Neda, Sonja and Sweta - thank you for all the pep talks and for making me a better version of me, really! Thank you Vaishali, Janis and Juliane for being my refuge and for reviving me from the everyday-panic-hour! A very special note of thanks to Sandra, Kirsten, Gina, Oksana, Luisa, colleagues at the IT, E-Workshop and the Mech-Workshop - thank you for making all these years very very smooth!

My deepest thanks are due to all these beautiful humans who have co-travelled with me through teenage to the kind of grown up years - Nivedita, Preeti, Nupur, Anubha, Priti, Sanchita, Suman, Harshita, JP, Indu, Smita, Greeshma and Shweta. It is through you all that I see life and myself. And will continue doing so. Thank you Bhumi, Steffi and Ayan for being my family in Hannover and for bringing so much joy in these years!

I am indebted to my brother, Harsh and to my aunt, Bhawana for standing right behind me in every damn situation and for dancing with me till the silver lining appeared through dark clouds. Piyush, I could not have asked for a better partner! Thanks for being my better half and for that daily push towards my goals. I owe this thesis the most to the hard work and encouragement of my grandparents, mother and father who continue to inspire me with their simplicity and kindness. Also a big shout out to the rest of my family members for nurturing me and taking pride in my work!

Last but not the least, for proofreading small and big parts of this thesis I would like to thank Christoph, Jim, Harald, Suresh, Fabio, Severin and Nikhil. All the remaining errors are due to my fault. There are likely more people whom I have not managed to acknowledge here, thanks for your part in my journey!